

**Inverse Shape Design of Compressor and Turbine Stages Using a
Commercial CFD Program**

Araz Arbabi

A Thesis

In the Department

of

Mechanical, Industrial and Aerospace Engineering

Presented in Partial Fulfillment of the Requirements

For the Degree of

Doctor of Philosophy (Mechanical Engineering) at

Concordia University

Montreal, Quebec, Canada

June 2018

© Araz Arbabi, 2018

CONCORDIA UNIVERSITY
SCHOOL OF GRADUATE STUDIES

This is to certify that the thesis prepared

By: Araz Arbabi
Entitled: Inverse Shape Design of Compressor and Turbine Stages Using a Commercial
CFD Program

and submitted in partial fulfillment of the requirements for the degree of

Doctor Of Philosophy (Mechanical Engineering)

complies with the regulations of the University and meets the accepted standards with respect to originality and quality.

Signed by the final examining committee:

<u>Dr. Abdel Sebak</u>	Chair
<u>Dr. Huu-Duc Vo</u>	External Examiner
<u>Dr. Samuel Li</u>	External to Program
<u>Dr. Ali Dolatabdi</u>	Examiner
<u>Dr. Marius Paraschivoiu</u>	Examiner
<u>Dr. Wahid Ghaly</u>	Thesis Supervisor (s)
<u></u>	

Approved by

Dr. Ali Dolatabadi Chair of Department or Graduate Program Director

August 9, 2018

Date of Defence

Dr. Amir Asif Dean, Faculty of Engineering and Computer Science

Abstract

Inverse Shape Design of Compressor and Turbine Stages Using a Commercial CFD Program

Araz Arbabi, Ph.D.
Concordia University, 2018

An aerodynamic inverse shape design of turbomachinery blading in three-dimensional viscous flow is developed and implemented into a commercial CFD program, namely ANSYS-CFX.

The design method is based on specifying one blade parameter, the stacking condition that is a line from hub to tip, and two other flow parameters these can be a- a target pressure distribution over the blade suction surface (or a target pressure loading) and a blade thickness distribution, b- or target pressure distributions on pressure and suction surfaces. This inverse design approach is fully consistent with the viscous flow assumption and is independent of the CFD approach taken.

The blade walls are assumed to be moving with a virtual velocity that would asymptotically drive the blade to the shape that would correspond to the specified target pressure distribution. This virtual velocity distribution is computed from the difference between the computed and the target pressure distributions. The wall displacement is computed in a Junction Box Routine and communicated to ANSYS-CFX using CFX Expression Language and User Defined Functions at each design step.

In ANSYS-CFX, an element based finite volume formulation is used for space discretization. The Arbitrary Lagrangian-Eulerian formulation of the unsteady Reynolds-Averaged Navier Stokes (URANS) equations is solved in a time accurate fashion with the blade motion being the source of

unsteadiness. At each time step, the blade shape is modified and dynamic meshing is used to remesh the fluid flow domain.

The implementation is first validated on a transonic rotor blade; the capability, robustness and accuracy of the method in satisfying the design target are then assessed on a single subsonic stator blade row, the rotor blade of an axial compressor stage and, the rotor and stator blades of an axial turbine stage where different choices of the design variables are used. The method is finally implemented to the redesign of a transonic compressor stage, a subsonic axial compressor stage and a turbine stage so as to improve their aerodynamic performance.

Acknowledgement

Thanks are due to all the people who helped me so much throughout this research work. To mention a few, I express my deepest appreciation to my supervisor Dr. Wahid Ghaly who trusted me and offered me this great opportunity, motivated me and provided me with his exceptional guidance during the course of this work.

Special thanks go to Dr. Adam J. Medd of Honeywell Aerospace for his continuous technical support during this work and to Dr. Mahmoud Mansour for his general support. The continuous financial support of Honeywell International from initiation to completion is greatly acknowledged.

Finally, I sincerely thank my wonderful parents, without whom it was impossible for me to complete this journey, for their emotional and integral support, sympathy and care.

Contents

List of Figures	x
List of Tables	xiv
Nomenclature	xv
Chapter 1.....	1
Introduction.....	1
1.1. Previous investigations	3
1.2. Present Investigation	9
1.3. Objectives of the present work	10
1.4. Thesis outline	11
Chapter 2.....	12
Flow governing equations	12
Figure 2.1. A typical two-dimensional control volume in ANSYS-CFX.....	12
2.1. Mesh deformation	15
2.1.1 Regions of motion specified.....	16
2.1.1.1. Mesh motion options	16
2.1.1.2. Mesh stiffness.....	18
Chapter 3.....	20

Inverse Design Methodology and algorithm.....	20
3.1. Inverse design formulation	21
3.2. Inverse design variables.....	25
3.2.1. Target pressure loading and blade thickness distribution.....	25
3.2.2. Target suction surface pressure and thickness distribution	26
3.2.3. Target pressure distribution on the blade pressure and suction surfaces	27
3.3. Inverse design implementation	27
3.4. Reconstruction of the 3D designed blade	31
3.5. Design constraints.....	35
3.6. Inverse design algorithm.....	35
3.7. Challenges associated with 3D inverse design versus 2D inverse design	38
Chapter 4.....	39
Validation of the Methodology & Design Convergence	39
4.1. Validation of the inverse design implementation in ANSYS-CFX.....	40
4.2. Redesign of the stator 67 as a single blade row	46
4.3. Redesign of the E/CO-3 compressor rotor.....	50
4.4. E/TU-3 turbine rotor redesign	53
4.5. E/TU-3 turbine stator redesign	53
4.6. Concluding remarks	54

Chapter 5.....	60
CFD analysis and inverse design of axial compressor and turbine stages	60
5.1. Analysis of the E/CO-3 Compressor Stage	60
5.2. Redesign of the E/CO-3 compressor stage at Maximum Flow	65
5.3. Redesign of the E/CO-3 compressor stage at Design Point.....	68
5.4. Analysis of the transonic compressor stage 67	81
5.5. Redesign of the transonic axial flow compressor	84
5.6. Analysis of the E/TU-3 Turbine Stage	91
5.7. Redesign of the E/TU-3 turbine stage at Design Point	92
Chapter 6.....	99
Conclusion	99
6.1. Summary	99
6.2. Future work.....	101
References	103
Appendix A.....	109
Validation of the inverse design implementation in ANSYS-CFX (Fitting Approach).....	109
Appendix B	112
Computational domain	112
B.1. NASA Rotor 37.....	112

B.2.	E/CO-3 Compressor Stage.....	114
B.3.	Transonic Compressor 67	116
B.4.	E/TU-3 Turbine Stage	118

List of Figures

Figure 1.1. Convergence history [23].....	5
Figure 1.2. Flow diagram of inverse design integrated into a CFD solver [30].....	7
Figure 2.1. A typical two-dimensional control volume in ANSYS-CFX [34].....	12
Figure 3.1. Normal to the blade surface at discrete points	22
Figure 3.2. Schematic representation of wall movement	23
Figure 3.3. Blade-to-blade plane in a cascade	26
Figure 3.4. Normal camber & thickness: Solid line (Designed part of the blade) and dashed line (TE).....	29
Figure 3.5. Camberline smoothing (High frequency removal)	30
Figure 3.6. Airfoil reconstruction after adding normal thickness to the camberline	31
Figure 3.7. Design (red) and intermediate (black) gridlines for Rotor 67.....	33
Figure 3.8. Streamwise (black) and spanwise (blue) control points for NASA Rotor 37	34
Figure 3.9. Computational algorithm for 3D inverse design.....	37
Figure 4.1. Rotor 37: Mesh close-up near the LE of the hub.....	42
Figure 4.2. Rotor 37: Mesh close-up near the TE of the tip	42
Figure 4.3. Rotor 37: L2 norm of Displacement.....	43
Figure 4.4. Rotor 37: L2 norm of DP	43
Figure 4.5. Rotor 37 validation:Original and design pressure loading	44
Figure 4.6. Rotor 37 validation: Original and design airfoil geometry	45
Figure 4.7. Stator 67: Original and design spanwise airfoils.....	46
Figure 4.8. Stator 67: Original, target and design loading distribution	47

Figure 4.9. Stator 67: Original, target and design pressure loading	49
Figure 4.10. Stator 67: Original and design airfoil geometry	50
Figure 4.11. E/CO-3 Compressor Rotor: Original and design static pressure.....	51
Figure 4.12. E/CO-3 Compressor Rotor: Original and design airfoil geometry	52
Figure 4.13. E/TU-3 Trubine Rotor: Original and design airfoil geometry.....	56
Figure 4.14. E/TU-3 Turbine Rotor: Original, target and design static pressure	57
Figure 4.15. E/TU-3 Turbine Stator: Original and design airfoil geometry.....	58
Figure 4.16. E/TU-3 Turbine Stator: Original, target and design pressure loading	59
Figure 5.1. Velocity profile inside the boundary layer of the fine mesh	61
Figure 5.2. Velocity profile inside the boundary layer of the coarse mesh.....	62
Figure 5.3. E/CO-3 Rotor redesign at maximum flow conditions: pressure loading	66
Figure 5.4. E/CO-3 Rotor redesign at maximum flow conditions: geometry	67
Figure 5.5. E/CO-3 Rotor redesign at Design Point: pressure loading at 15% and 60% span	69
Figure 5.6. E/CO-3 Rotor redesign at Design Point: geometry at 15% and 60% span.....	70
Figure 5.7. E/CO-3 Rotor redesign at Design Point: 1 st and test designed pressure distributions	72
Figure 5.8. E/CO-3 Rotor redesign at Design Point: Original and designed loading distribution.	74
Figure 5.9. E/CO-3 Rotor redesign at Design Point: Original and designed airfoils.....	75
Figure 5.10. E/CO-3 Rotor redesign at Design Point: Original and designed static pressure.....	76
Figure 5.11. E/CO-3 Rotor redesign at Maximum Flow: Original and designed loading distribution	78
Figure 5.12. E/CO-3 Rotor redesign at Maximum Flow: Original and designed static pressure ..	79
Figure 5.13. Original and designed efficiency in spanwise direction (mid-chord)	80

Figure 5.14. Original and designed pressure gradient in spanwise direction (mid-chord)	80
Figure 5.15. Original and designed pressure gradient in streamwise direction (mid-span)	81
Figure 5.16. E/CO-3 Rotor: Design and intermediate airfoils before and after the design	82
Figure 5.17. stage 67 meshed by TurboGrid.....	83
Figure 5.18. Velocity vectors near the tip section of original Stator 67	85
Figure 5.19. Velocity vectors near the tip section of designed Stator 67.....	86
Figure 5.20. Stage 67 stator design: Target and design pressure loading.....	88
Figure 5.21. Stage 67 stator design: Original and design blade shape.....	89
Figure 5.22. Stage 67 stator design: Original and design spanwise total pressure	89
Figure 5.23. Stage 67 stator design: Original and design spanwise efficiency	90
Figure 5.24. Stage 67 stator geometry: Original vs. Designed.....	90
Figure 5.25. 3D view of E/TU-3 Turbine Stage.....	91
Figure 5.26. E/TU-3 Rotor redesign: Original, target and design loading at 55% and 80% span .	94
Figure 5.27. E/TU-3 Rotor redesign: Original and design geometry at 55% and 80% span	95
Figure 5.28. E/TU-3 Rotor redesign: Original and design static pressure at 55% and 80% span .	96
Figure 5.29. E/TU-3 Rotor: Original and designed efficiency in streamwise direction	97
Figure 5.30. E/TU-3 Rotor: Original and designed pressure gradient in streamwise direction ...	98
Figure A.1. Rotor 37 validation (Fitting approach):Original and design pressure loading	110
Figure A.2. Rotor 37 validation (Fitting approach):Original and design geometry	111
Figure B.1. NASA Rotor 37 – Computational domain	112
Figure B.2. NASA Rotor 37 – Meridional view	113
Figure B.3. NASA Rotor 37 – Blade-to-blade view at mid-span.....	113

Figure B.4. NASA Rotor 37 – Blade tip and tip clearance	114
Figure B.5. E/CO-3 Compressor Stage – Computational domain: Rotor (left) & Stator (right) ..	114
Figure B.6. E/CO-3 Compressor Stage – Meridional view	115
Figure B.7. E/CO-3 Compressor Stage – Blade-to-blade view at mid-span	115
Figure B.8. E/CO-3 Compressor Rotor – Blade tip & tip clearance.....	116
Figure B.9. Stage 67 – Computational domain: rotor (left) & stator (right).....	116
Figure B.10. Stage 67 – Meridional view	117
Figure B.11. Stage 67 – Blade-to-blade view at mid-span	117
Figure B.12. Rotor 67 – Blade tip & tip clearance.....	118
Figure B.13. E/TU-3 Turbine Stage – Computational domain: stator (left) & rotor (right)	118
Figure B.14. E/TU-3 Turbine Stage – Meridional view.....	119
Figure B.15. E/TU/3 Turbine Stage – Blade-to-blade view at mid-span.....	119

List of Tables

Table 5.1. E/CO-3 Stage geometric characteristics.....	61
Table 5.2. E/CO-3 compressor stage analysis results at Maximum Flow	63
Table 5.3. E/CO-3 compressor stage analysis results at Design Point.....	64
Table 5.4. Original and design flow parameters at maximum flow conditions.....	68
Table 5.5. Original and design flow parameters at Design Point	73
Table 5.6. Original and design flow parameters at Maximum Flow.....	77
Table 5.7. Stage 67 geometric parameters.....	83
Table 5.8. Stage 67 analysis results at design point	84
Table 5.9. Stator 67 DP Design parameters.....	87
Table 5.10. E/TU-3 stage geometric characteristics	92
Table 5.11. E/TU-3 turbine stage analysis results at Design Point	92
Table 5.12. E/TU-3 turbine stage: Original and design flow parameters	97

Nomenclature

c	Speed of sound
C	Stiffness model exponent
d	Distance
f	Blade camber line
F	Conservative flux vector, virtual momentum flux
G	Conservative flux vector, virtual momentum flux
H	Conservative flux vector, virtual momentum flux
G	Viscous flux vector
M	Mach number
n	Normal vector
p	Pressure
s	Wall displacement
S	Control surface, Source term
t	Fictitious or physical time
T	Thickness, Temperature
u	Velocity component in x- direction
U	Primitive variable vector
v	Velocity component in y- direction
V	Control volume

w	Velocity component in z- direction
x	x- coordinate
y	y- coordinate

Greek Symbols

α	Angle of segment connecting PS to SS at each axial location
β	Relative flow angle
ε	Under – relaxation factor for wall movement
Γ	Diffusivity, Mesh stiffness
$\Delta(\cdot)$	= $(\cdot)_{tgt} - (\cdot)$ along the blade surface
ρ	Density
μ	Dynamic Viscosity
δ	Node displacement
\emptyset	Total energy per unit of mass
ω	Relaxation factor

Subscripts

0	Total (or stagnation)
$1,2$	Rotor inlet, outlet
eff	effective
g	Moving grid
i,j	counter

<i>new</i>	Current time step
<i>old</i>	Previous time step
<i>stiff</i>	stiffness
<i>tgt</i>	Target
<i>v</i>	Viscous, Virtual velocity
<i>x</i>	x- coordinate (spanwise direction) of the blade
<i>y</i>	y- coordinate (blade-to-blade direction) of the blade
<i>z</i>	z- coordinate (axial direction) of the blade
<i>x'</i>	x-coordinate of the camberline
<i>y'</i>	y-coordinate of the camberline
<i>z'</i>	z-coordinate of the camberline

Superscripts

–	Suction side
+	Pressure side

Acronyms

<i>ALE</i>	Arbitrary Lagrangian–Eulerian
<i>CEL</i>	CFX Expression Language
<i>CFD</i>	Computational Fluid Dynamics
<i>DP</i>	Blade Pressure Loading
<i>HFR</i>	High Frequency Removal
<i>JB</i>	Junction Box

<i>LE</i>	Leading edge
<i>PR</i>	Stage pressure ratio
<i>PS,SS</i>	Blade pressure side, suction side
<i>RANS</i>	Reynolds-averaged Navier Stokes
<i>TE</i>	Trailing edge
<i>TRR</i>	Temperature rise ratio
<i>UDF</i>	User defined function

Chapter 1

Introduction

Computer programs have been used for decades to analyze the flow field around gas turbine engine components including compressor and turbine blades by solving the Reynolds-averaged Navier Stokes (RANS) equations. The evolution of numerical analysis techniques has reached to the point where many industries, including the gas turbine industry, have employed commercial CFD (Computational Fluid Dynamics) packages to determine the flow properties and obtain the performance of their potential products. On the other hand, numerous design methods have been developed to improve the aerodynamic performance of compressors or turbines.

The earliest design methods were simply based on trial and error where the designer first designs a blade shape and then assesses its performance by analyzing the flow field around the blade which is obviously time consuming and inefficient.

The maturity of CFD techniques over time resulted in the development of faster and more efficient design tools. Automatic Numerical Optimization [1-4] is one of these approaches where the blade geometry is modified to satisfy a certain design objective(s) subject to some constraints. The designer specifies the design objective such as turbine efficiency and constraints (e.g. geometric features) and models the structure of the problem, then optimization algorithm scans the design space automatically and provides a solution that satisfies the objective(s) subject to the set constraints [5]. However, it is computationally expensive as it usually requires a large number of flow simulations to compute the optimization objectives and constraints.

In order to reduce the computational cost associated with classic optimization methods, adjoint methods based on control theory [6] were then developed where the blade profile is considered as the control variable and the goal is to minimize a cost function which is a measure of deviation from the desired function e.g., pressure distribution. Another advantage of this method is that even if the desired function is not explicitly attainable, it is still possible to find a minimum for the cost function i.e., minimize the deviation from target [6]. However, if the cost function contains multiple minima, the adjoint method risks of converging to the nearest local. The complexity associated with the derivation of the adjoint equations and the computational cost are still a motivation to improve these methods [7].

Another design approach that is much less time-consuming is the aerodynamic Inverse Shape Design. The computational time of this method is comparable with that of the analysis methods. In that approach, the blade profile that satisfies a detailed flow performance is targeted, e.g. the static pressure distribution over the blade surfaces or the blade pressure loading and thickness distribution.

However, a successful redesign depends on the proper selection of the target function e.g., pressure distribution which requires an experienced designer to choose the realistic and appropriate target function for the design process.

In this work, an existing method for the inverse design in two-dimensional flow, has been extended to the redesign of airfoils in three-dimensional flow and implemented via the commercial software ANSYS-CFX.

1.1. Previous investigations

Inverse design methods date back several decades and were first implemented on an airfoil in two-dimensional potential flow, then for inviscid flow and finally viscous flow. Some of these methods were based on a target pressure distribution on the airfoil surfaces [8-12], or Mach number [13], or velocity [14] or the pressure loading and blade thickness distributions [15-18]. The design process started from an existing blade geometry, then using the difference between the design and target functions, the blade shape deformed repeatedly so as to finally deliver the prescribed target functions. Although it has been shown in different works that the inverse design is efficient for internal flows [10-12], [16], [18], most of them still have some traces of the inviscid flow that might affect the scheme stability, robustness or consistency.

Giles and Drela [10] make use of viscous-inviscid interaction, Damle *et al.* [16] use the tangency condition to compute the designed blade camberline by imposing thickness and loading distribution as target quantities. In other methods such as Demeulenaere *et al.* [11], the transpiration condition has been used where the tangential and normal components of the velocity over the blade surfaces are computed in order to find the new blade profile. Another approach, de Vito *et al.* [12], uses both Navier Stokes and Euler solvers for the flow analysis and inverse design, respectively; or the work done by Mendes *et al.* [19] who used artificial viscosity to enhance the Euler system of equations and take the viscous effects into account. In all of these methods it has been assumed that the flow is attached to the airfoil/blade and the boundary layer is well behaved. In other words, in cases where flow separation occurs, these methods are questionable and the results thus obtained are questionable.

In most inverse methods neither the mesh movement is accounted for in the computations nor the transient term is considered in the CFD formulation so that the solution is transposed from one

mesh to the next and the problem is solved as quasi-steady (time marching) problem; such as the methods surveyed and classified by Dulikravich [20]. The error resulting from quasi-steady solutions obtained on transposed meshes is propagated into the designed blade shape and therefore causes inaccurate pressure distribution in the next iteration. The error is accumulated during the design process and may lead to divergence of the iterative process. An example of this situation is the work of Yang and Ntone [21] who extended the work of Thompkins and Tong [8], [22] to viscous flow and obtained a rather wavy blade profile. Daneshkhah and Ghaly [23] showed that the above mentioned error is due to the quasi-steady assumption and can be removed by using a time accurate formulation and modifying the governing equations to account for the mesh movement. Using a time accurate formulation improved the convergence even in difficult cases such as transonic design cases. The convergence improvement was partly demonstrated by Demeulenaere *et al.* [11] where they accounted for the mesh movement in the governing equations, while still using time marching scheme; or by Qiu *et al.* [24] who used the quasi-steady form of 3D Navier-Stokes equations for inverse design implementation; both were based on the transpiration model. Daneshkhah and Ghaly [23] showed that by using a time accurate formulation, the problem converges in transonic cases while the quasi-steady approach fails to converge in these cases. The convergence history of a quasi-steady and time accurate solution is compared in Figure 1.1. The inverse method developed by Daneshkhah and Ghaly [23], [25] is fully consistent with viscous flow. It was first used to redesign a two-dimensional transonic turbine vane. Later on, Roidl *et al.* [26] extended the method to the redesign of one or more stages.

In this method, the blade surface moves with a fictitious velocity so as to satisfy the prescribed target pressure distribution. The virtual velocity of the blade surface is computed from a balance

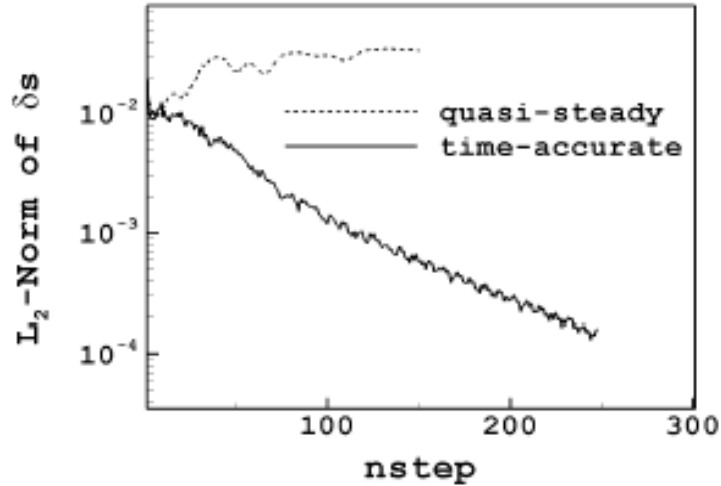


Figure 1.1. Convergence history [23]

of the current and target momentum fluxes which means that as the current pressure along the airfoil surfaces gets closer to the target, the virtual velocity gets closer to zero as well. This virtual velocity moves the nodes to their new position so that a new airfoil shape is designed which satisfies the target pressure.

The Reynolds-averaged Navier Stokes (RANS) equations are used to compute the flow field in analysis mode while the unsteady Reynolds-Averaged Navier Stokes (URANS) equations, which are written for the moving and deforming mesh using an Arbitrary Lagrangian–Eulerian (ALE) formulation, are used in design (unsteady) mode.

The method, which is developed as an in-house CFD code, was validated first. It was then successfully applied to the redesign of the rotor and stator airfoil of the low speed single stage E/TU-3 turbine in 2D flow. A similar method was developed by Mileschin *et al.* [27] into an in-house code where a target pressure is prescribed over the suction surface of the blade and uses the time accurate formulations to design a full 3D transonic fan rotor.

The method developed by Danshkhah and Ghaly [23] was later on implemented by Arbabi and Ghaly [28] into a commercial CFD program where for the first time the same CFD code was used for both analyzing as well as designing the blade profile which satisfies a given design target e.g. the loading or static pressure distribution.

Another example is the more recent work of Poursadegh *et al.* [29] who developed a quasi-3D inverse method to redesign centrifugal compressor impeller by solving the Euler equations on the blade-to-blade planes. The blade-to-blade profile of the impeller is modified based on the difference between current and target pressure distributions and finally a profile that satisfies the target pressure is obtained. Although the flow field over the designed blade is later analyzed using a fully-3D viscous code, the quasi-3D analysis code which was used in the design phase does not inherently account for viscous effects, flow separation and full 3D flow effects e.g., separation may occur for extreme cases.

Another recently developed inverse method is a dual speed inverse design code developed by Hield *et al.* [30] for the design of multistage transonic fans. This work is based on the method of Hield [31] where the time marching form of the RANS equations in 3D flow is used to inverse design multistage axial compressors.

The intent of the method is to reach the desired stage radial pressure ratio and stator exit flow angle by satisfying the target tangential angular momentum (for the rotor) and target exit blade angle (for the stator) and also to set the design mass flow rate by a choked nozzle. In their work different target functions are applied to two different rotor speeds simultaneously. For high (100%) speed the stage radial pressure ratio and stator exit metal angle and mass flow rate are set as target in order to obtain the desired take-off performance while pressure loading (lift) distribution is set as the target at part (90%) speed to achieve maximum efficiency at cruise conditions. The thickness

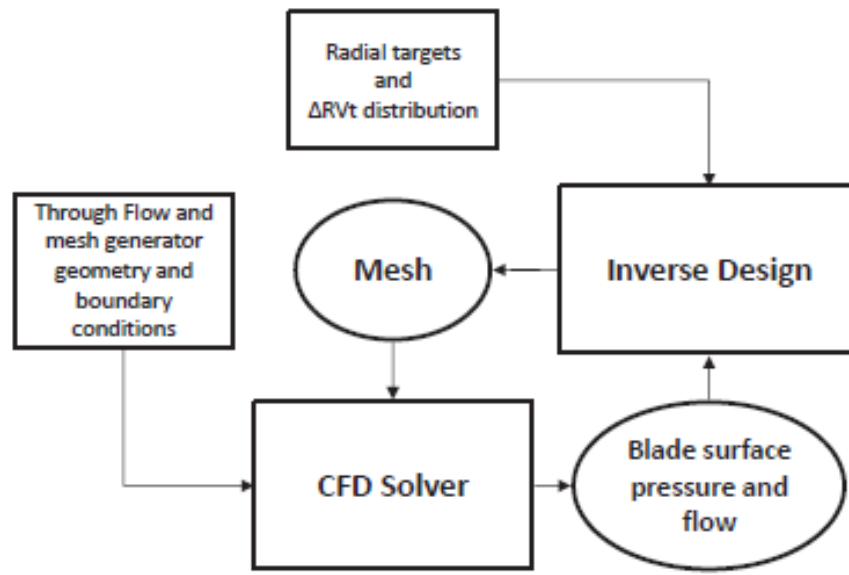


Figure 1.2. Flow diagram of inverse design integrated into a CFD solver [30]

of the blade is also maintained hence the method is referred to as semi-inverse design by the author [30]. The algorithm is developed as a stand-alone code but is claimed, by the authors, to be easily wrapped around any CFD solver.

Figure 1.2 shows the overall inverse design flow chart when coupled with a CFD solver. The original blade geometry, mesh and boundary conditions are set into the solver environment, the flow field is computed and then passed to inverse module to modify the geometry. The new blade is then fed back to the solver, the mesh is adjusted to new blade and the whole process is repeated until the target is reached. As it can be seen, the designer does not need to worry much about the mesh adjustment, governing equations, viscous effects etc. Also, linking the design module to an established CFD solver will help improving the accuracy of the solution.

The prescribed surface curvature distribution blade design (CIRCLE) Korakianitis *et al.* [32] is another design method that is used to design and redesign both 2D and 3D turbine and compressor blades as well as isolated airfoils. The blade surface curvature distribution is first prescribed based

on which the blade geometry is obtained. It allows any manufacturable shapes for leading and trailing edges and ensures the smoothness of the blade surface at the joint point and curvature and slope of curvature continuity on the entire airfoil which consequently leads to a smooth surface pressure or Mach number distribution over the blade surface.

In this method, the selected 2D sections of the blade are first designed and it can be extended to 3D blade design by smoothly modifying the blade design parameters such as inlet/outlet angles, stagger angle etc. in span-wise direction all the way from hub to tip [32].

It is an iterative process that can be used to design the blade based on the given throughflow parameters to finally obtain the desired performance or it may be used to provide the inverse or optimization design methods with the original blade geometry. Similar to inverse design methods, it may also be used to redesign the blade by manipulating the blade surface curvature distribution and subsequently moving the maximum loading or Mach number along the blade surface towards the target to improve the performance.

The RANS computations of the CIRCLE method presented above is solved by FLUENT which is an advantage in the sense that it can profit from all the features built into this software to obtain a converged solution and each run for a 2D blade takes about 2-4 hours [32]. However, the disadvantage of the method is that the redesign phase of the method is governed by Euler equations hence doesn't account for viscous effects and reduces the solution accuracy.

Moreover, compared to inverse design, it is a time consuming method as the designer needs to experimentally manipulate the curvature distribution and change the loading or Mach distribution over the blade to finally improve the performance. However, as mentioned earlier, it can be a very useful tool to provide the inverse design with a decent geometry as the initial input.

1.2. Present Investigation

The current research builds on the work of Arbabi and Ghaly [28] who implemented into ANSYS-CFX the inverse design method originally developed by Daneshkhah and Ghaly [23], [25] and used it for the redesign of compressor and turbine airfoils in two-dimensional flow.

The design method is theoretically developed for the inverse design of blades in three-dimensional flow and is then implemented into ANSYS-CFX using Junction Box Routines and User CEL Functions provided by ANSYS to interact with the CFD program. The design variables used in the present work are either the static pressure distribution on the blade pressure and suction surfaces or the pressure loading and the blade thickness. A third design variable is also introduced for the design in 3D flow: a stacking line that describes how the airfoils are stacked in the spanwise direction. The airfoils tangential thickness and camberline which were used in 2D inverse design are replaced with normal camber and thickness distributions.

In analysis mode, the Reynolds-averaged Navier Stokes (RANS) equations are used to calculate the flow field and parameters while, in design mode, the unsteady Reynolds-Averaged Navier Stokes (URANS) equations (the unsteadiness being generated by the moving and deforming blades) written for a moving and deforming mesh using an Arbitrary Lagrangian–Eulerian (ALE) formulation are used.

The methodology is validated first for a transonic compressor rotor; it is then implemented on compressor and turbine blades to assess the design convergence and to measure how accurately the prescribed target is satisfied. The method is finally applied to the redesign of a transonic compressor stage [33], a subsonic compressor and a turbine stage.

In this work, emphasis is put on the robustness, flexibility and generality of the method in handling different flow configurations and different flow regimes within the framework of a commercial

CFD program. This study demonstrates that the present inverse method can be coupled to a commercial CFD program, while being independent of the CFD program [33].

1.3. Objectives of the present work

It is clear from previous investigations particularly in three-dimensional inverse design methods, that the methods are restricted to private CFD codes, the details of the development are not mentioned such as the design space and the analysis space and how to pass from one to the other, the stacking condition which is an inherent design variable in 3D inverse design, the choice of design variables and many other design issues that engineers have to address in the course of the design process.

The main objectives of this work can be described as follows:

- Develop an aerodynamic inverse design approach that is fully consistent with viscous flow and can be applied in three-dimensional flow.
- Provide a clear description of the analysis space and design space and variables and how to pass from one space to the other. The possible choices of design variables is worth a discussion to shed some light of the design process.
- Implement the 3D inverse design methodology into a commercial code so that the same CFD code be used for both analysis and design process.
- Develop/Program the tools that are needed for a robust convergence of the design process
- Assess the methodology in the redesign and performance improvement of axial compressor and turbine stages. The design can be applied onto a single blade row, one or multiple stages based on the design input.

1.4. Thesis outline

This thesis consists of five chapters including the introduction. Chapter 2 presents the space discretization and time integration of the flow governing equations for stationary and deforming control volumes (moving mesh) in time followed by the details of different mesh motion options available in the CFD program. Inverse design methodology and formulation in 3D flow, as well as different choices of the design variables and design constraints are discussed in detail in Chapter 3. The inverse design algorithm, aspects of back and forth communication between the CFD program and the user routines throughout the design process, and the contribution of the Junction Box Routine and User CEL functions in the design implementation are given first in Chapter 4. The validation of the methodology, performed on transonic Rotor 37, is presented later on in this chapter followed by the assessment of the design convergence on a single subsonic stator blade row, the rotor blade of E/CO-3 compressor and rotor and stator blades of E/TU-3 turbine stage. The computational domain of Stage 67, E/CO-3 compressor (at two different operating conditions) and E/TU-3 turbine stages are then analyzed and the results thus obtained are validated against the available experimental data. Those stages, after being validated numerically, are inversely redesigned in order to improve their aerodynamic performance. The last chapter contains the concluding remarks where the achievements of the current work are summarized and recommendations for future work, to even further enhance the methodology and make it more practical in industrial applications, are provided.

Chapter 2

Flow governing equations

ANSYS-CFX is a general-purpose CFD program; the space is discretized using a finite-element-based finite volume method using e.g., a triangular mesh in two-dimensional flow, as illustrated in Figure 2.1. The conservation equations for mass, momentum, energy and species are discretized in space on the shown mesh, they are then integrated in time to account for the flow unsteadiness [34].

For simplicity, Figure 2.1 shows a two-dimensional mesh in ANSYS-CFX. All variables in ANSYS-CFX are stored at the nodes that are surrounded by control volumes. Control volumes are constructed by connecting the edge and element centers around every single node [34].

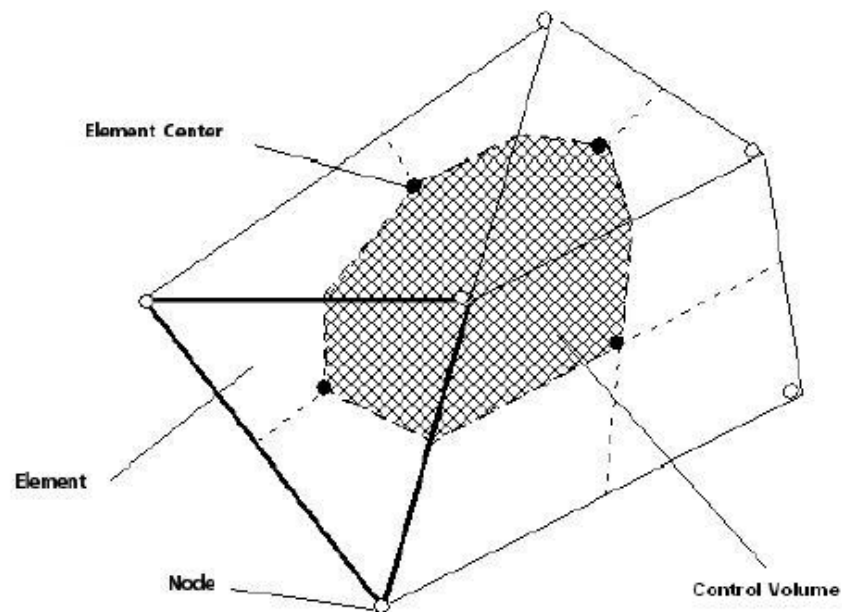


Figure 2.1. A typical two-dimensional control volume in ANSYS-CFX [34]

The conservation form of the three-dimensional URANS equations accounting for mesh movement which is written in an Arbitrary Lagrangian–Eulerian (ALE) formulation is as follows:

$$\frac{\partial U}{\partial t} = \frac{\partial(F-F_g-F_v)}{\partial x} + \frac{\partial(G-G_g-G_v)}{\partial y} + \frac{\partial(H-H_g-H_v)}{\partial z} \quad (2-1)$$

Where ‘ U ’ is the solution vector that contains the dependent flow variables, ‘ $F-F_g$ ’, ‘ $G-G_g$ ’ and ‘ $H-H_g$ ’ are the convective flux vectors relative to the moving grids while F_v , G_v and H_v stand for the viscous flux terms [33]. In cases where there is no mesh movement, the terms F_g , G_g and H_g are zero.

The integral conservation form of Eq. 2-1 for non-deforming control volumes (i.e., F_g and G_g are zero), in three-dimensional flow are [34]:

$$\frac{d}{dt} \int_V \rho dv + \int_S \rho U_j dn_j = 0 \quad (2-2)$$

$$\frac{d}{dt} \int_V \rho U_i dv + \int_S \rho U_j U_i dn_j = - \int_S P dn_j + \int_S \mu_{eff} \left(\frac{\partial U_i}{\partial x_j} + \frac{\partial U_j}{\partial x_i} \right) dn_j + \int_V S_{U_i} dv \quad (2-3)$$

$$\frac{d}{dt} \int_V \rho \phi dv + \int_S \rho U_j \phi dn_j = \int_S \Gamma_{eff} \left(\frac{\partial \phi}{\partial x_j} \right) dn_j + \int_V S_\phi dv \quad (2-4)$$

Equations 2-2, 2-3 and 2-4 represent the conservation of mass, momentum and energy, respectively. ‘ V ’ and ‘ S ’ indicate the volume and surface integration regions and ‘ dn_j ’ is the differential component of the vector normal to the control surface. ‘ S_{U_i} ’ and ‘ S_ϕ ’ are momentum and energy source terms, which are zero in the scope of this work since there is no body forces nor

heat generation in the computational domain. ‘ μ_{eff} ’ is the effective or total viscosity, which is the sum of molecular and turbulent eddy viscosity. ‘ Γ_{eff} ’ is the effective thermal diffusivity that is the sum of molecular and turbulent diffusivity and ϕ is total energy per unit of mass [34], [35].

Equations 2-2 to 2-4 must be modified when the control volumes, hence domain mesh, deform in time. In ANSYS-CFX this modification is performed by applying the Leibnitz Rule [34]:

$$\frac{d}{dt} \int_{V(t)} \phi dv = \int_V \frac{\partial \phi}{\partial t} dv + \int_S \phi W_j dn_j \quad (2-5)$$

Where W_j represents the velocity of the control surface. By applying the Leibnitz Rule to the equations 2-2 to 2-4, the integral conservation equations for the deforming mesh are obtained [34]:

$$\frac{d}{dt} \int_{V(t)} \rho dv + \int_S \rho (U_j - W_j) dn_j = 0 \quad (2-6)$$

$$\frac{d}{dt} \int_{V(t)} \rho U_i dv + \int_S \rho (U_j - W_j) U_i dn_j = - \int_S P dn_j + \int_S \mu_{eff} \left(\frac{\partial U_i}{\partial x_j} + \frac{\partial U_j}{\partial x_i} \right) dn_j + \int_V S_{U_i} dv \quad (2-7)$$

$$\frac{d}{dt} \int_{V(t)} \rho \phi dv + \int_S \rho (U_j - W_j) \phi dn_j = \int_S \Gamma_{eff} \left(\frac{\partial \phi}{\partial x_j} \right) dn_j + \int_V S_\phi dv \quad (2-8)$$

In analysis mode where the domain mesh is stationary the Reynolds-averaged Navier Stokes (RANS) equations are used to simulate the flow field while the unsteady Reynolds-averaged Navier Stokes (URANS) equations, which are written for the moving and deforming mesh using the Arbitrary Lagrangian–Eulerian (ALE) formulation, are used in simulating the flow around a yet unknown blade profile that would produce a given e.g., pressure distribution along that blade

in design mode where the flow is assumed unsteady [35].

In time-accurate simulation, a high-resolution scheme, recommended by ANSYS-CFX for compressor and turbine simulations, is used for the advection terms and a first order scheme is used for the turbulence model for both steady and transient computations. A second order accurate backward Euler scheme, which is an implicit scheme used with constant or varying time step size, is used for time integration. Also for the different cases presented in this work the two-equation k-omega or Menter Baseline (BSL) k-omega or SST Turbulence models are used because of their accurate prediction of flow separation in areas with adverse pressure gradient (the models are integrated to the wall).

2.1. Mesh deformation

During the design process the blade profile deforms at each time step, hence the mesh movement has to be accounted for in formulating and solving the flow governing equations. In ANSYS-CFX [34], there are different options available for mesh deformation cases:

- Junction Box Routine: is used when the coordinates of all nodes in the domain are predefined and read in CFX from a file.
- Regions of Motion Specified: is used when the motion of a boundary or a sub-domain is specified [34].

In this work “Regions of Motion Specified” is selected since the displacement only along the blade boundary is calculated at each design step. The displacement is returned to CFX as Cartesian coordinates, it is then applied to the mesh. The mesh motion of the rest of the domain is computed by CFX to match the new blade profile while the mesh quality is maintained.

2.1.1 Regions of motion specified

The amount of nodes displacement (for the blade profile) is calculated from the inverse design functions which are formulated in a Junction Box Routine and linked to CFX (Refer to chapters 3 and 4 for details) while, for the remaining nodes of the domain, the mesh displacement is controlled by a mesh deformation model available in ANSYS-CFX the “Mesh Displacement Diffusion” [34]. The displacement applied to the blade boundary, is diffused to the rest of the boundaries or subdomains with this model and through solving the following equation:

$$\nabla \cdot (\Gamma_{disp} \cdot \nabla \delta) = 0 \quad (2-9)$$

Where δ is the node displacement relative to the node location before displacement and Γ_{disp} is the “mesh stiffness” which determines how closely the mesh regions displace together. In transient runs, this equation is solved at the start of each time step. The merit of using this model is to retain the original relative mesh distribution through the entire domain. For example, if an area of the domain has a fine mesh, such as the boundary layer around the blade wall, there will be still a fine mesh in those areas after the displacement [34], [35].

2.1.1.1. Mesh motion options

When the mesh deformation option is set to “Regions of motion specified”, different mesh motion options become available for the boundaries or subdomains. Care must be taken to select the appropriate option for each boundary. The available options in ANSYS-CFX which are used in this work are:

- Unspecified: as it appears from its name, in this option there is no restriction for the mesh deformation and nodes movement is determined by the motion of the other regions. Tip leakage region is an example of this option where the mesh displacement is dictated by the blade and shroud boundaries.
- Conservative interface flux: similar to the first option in the sense that there is no constraint for this option as well however the motion of the nodes in adjacent domains affect, and are affected by, the motion of the nodes on the interface. An example of this option is the periodic boundaries where there is a bilateral effect between the movement of the nodes located on these boundaries and nodes in the adjacent blade passages. This option is set for both periodic boundaries because they have identical properties.
- Stationary: there is no mesh movement and the boundary is stationary. Inlet and outlet boundaries are the examples of this option so as to maintain the exact same area throughout the design process.
- Specified displacement: nodes are moved according to the displacement given by CEL. This option is used for the blade boundary where the movement of the nodes are computed by the inverse design functions and returned to CFX to apply the displacement to the geometry. In fact the displacement of the nodes in all other regions and boundaries are determined by the displacement of the nodes located on the blade wall.
- Surface of revolution: nodes slide on the same boundary definition in order to avoid exiting the initial radial position. Hub and shroud boundaries are examples of this mesh motion option.

2.1.1.2. Mesh stiffness

The mesh stiffness value could vary or could be a constant value. By using a constant value, the mesh displacement computed for the specified regions, in this work the blade wall, will diffuse uniformly throughout the domain while a varying value will make the mesh regions have a smaller relative displacement in the regions having higher stiffness and vice versa. Varying mesh stiffness is useful in the fine mesh regions where preserving the structure of mesh distribution and also the mesh quality is of high importance e.g., the boundary layer around a blade and sharp corners [34], [35].

There are two options for the varying mesh stiffness in ANSYS-CFX:

- Increase near small volumes: where the mesh stiffness will increase in the regions having smaller control volumes. In this option the mesh stiffness is computed by following equation [34]:

$$\Gamma_{disp} = \left(\frac{\forall_{ref}}{\forall} \right)^{C_{stiff}} \quad (2-10)$$

Where \forall is the size of the control volume, \forall_{ref} is reference control volume with the default value set to 1 [m^3] and C_{stiff} is the “stiffness model exponent” which is the user input. In Eq. 2-10 as the size of the control volume decreases, the mesh stiffness increases exponentially and the value of C_{stiff} indicates the degree to which the stiffness increases [34].

- Increase near boundaries: where the mesh stiffness will increase in the regions near the boundaries such as inlet, outlet, wall, etc. and is computed by the following equation [34]:

$$\Gamma_{disp} = \left(\frac{L_{ref}}{d} \right)^{C_{stiff}} \quad (2-11)$$

Where d is the distance from the nearest boundary and L_{ref} is the reference length with the default value set to 1 [m]. In this model, the mesh stiffness will increase exponentially as the distance d decreases. Again C_{stiff} indicates how fast the mesh stiffness increases and is the user input [34]. In this work, the first option i.e., “increase near small volumes” is used in order to preserve the mesh quality and distribution near the blade wall and other regions with a fine mesh.

Chapter 3

Inverse Design Methodology and algorithm

In this chapter the three dimensional inverse design methodology, which was originally developed by Daneshkhah and Ghaly [23], [25] for two dimensional flow, and the available choices of the design variables are introduced. The principle of the method is the blade deformation resulted from a virtual velocity. The blade deforms repeatedly in order to satisfy the prescribed target function. The virtual velocity of the blade surface is computed based on the difference between current (or instantaneous) and design (or fixed) pressure distributions. As the instantaneous pressure on the blade surface gets closer to the target, the virtual velocity diminishes accordingly and reaches zero upon satisfaction of the target pressure. The nodes located on the blade surface move, based on the virtual velocity, to a new position to shape a new blade profile which produces the prescribed target.

The methodology is implemented in transient (unsteady) mode using time-accurate formulation of the RANS equations written in the Arbitrary Lagrangian–Eulerian (ALE) form to account for the mesh movement. The target pressure distribution depends on the choice of the design variables and could be either the static pressure distributions on the blade pressure and suction surfaces or the pressure loading and the blade thickness distribution. These choices will be discussed in detail in this chapter.

3.1. Inverse design formulation

The airfoil walls (2D spanwise gridlines) are assumed to be moving with a virtual velocity that would asymptotically drive the airfoil to the shape that would correspond to the specified target pressure distribution. This virtual velocity distribution is computed from the difference between the current ‘ F ’ and the fixed momentum fluxes of the designed blade ‘ F_{des} ’ to be obtained.

The momentum flux of 3D moving and deforming airfoil is written as:

$$F = \begin{bmatrix} (\rho u_v u_v + P)n_x + (\rho u_v v_v)n_y + (\rho u_v w_v)n_z \\ (\rho u_v v_v)n_x + (\rho v_v v_v + P)n_y + (\rho v_v w_v)n_z \\ (\rho u_v w_v)n_x + (\rho v_v w_v)n_y + (\rho w_v w_v + P)n_z \end{bmatrix} \quad (3-1)$$

Where $n = (n_x, n_y, n_z)$ is the outward vector normal to the blade surfaces. The virtual velocity of the nodes located on the blade wall is computed by equating the momentum flux of the moving wall (3-1) with the momentum flux that is assumed to exist on the target blade shape. As the blade reaches the shape that would satisfy the target pressure profile, the virtual velocities will vanish and the design momentum flux reads:

$$F_{des} = \begin{bmatrix} (P_{tgt}n_x) \\ (P_{tgt}n_y) \\ (P_{tgt}n_z) \end{bmatrix} \quad (3-2)$$

Hence, by equating the equations (3-1) and (3-2) the resulting virtual velocity components in the direction normal to the blade surface are obtained:

$$v_v = \pm \left(\frac{n_y^2}{n_x^2 + n_y^2 + n_z^2} \frac{|P_{des} - P|}{\rho} \right)^{\frac{1}{2}}$$

$$u_v = v_v \frac{n_x}{n_y} = w_v \frac{n_x}{n_z} \quad (3-3)$$

$$w_v = v_v \frac{n_z}{n_y} = u_v \frac{n_z}{n_x}$$

where (u_v, v_v, w_v) are the components of the virtual velocity normal to the blade wall. The normal to the blade surface at the discrete points on some airfoils are shown in Figure 3.1. A heavy relaxation factor is required for the computed virtual velocity in order to ensure the stability of the unsteady simulation [8]. The relaxation factor has the following form:

$$\omega = \varepsilon \cdot (1/a) \sqrt{|\Delta P|/\rho} \quad (3-4)$$

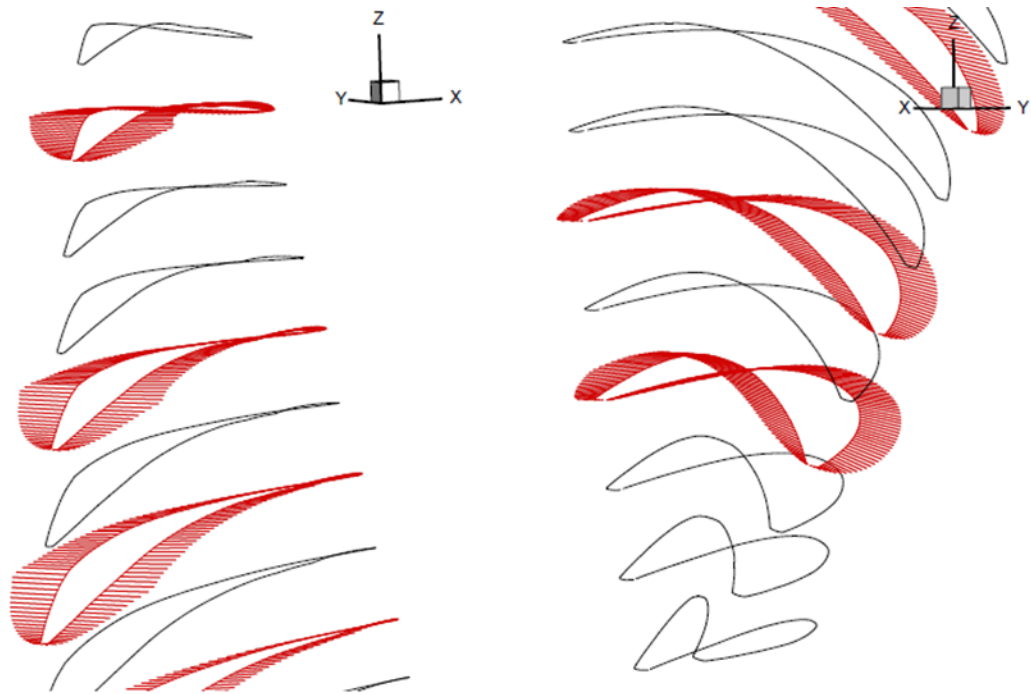


Figure 3.1. Normal to the blade surface at discrete points

Where ' ω ' is the relaxation factor, ' a ' is the speed of sound, ' ΔP ' is the difference between the current and target pressure distribution and ' ε ' is a constant that varies between 0.1 and 0.2 for subsonic flow and 0.05 and 0.1 for transonic flow cases.

The wall displacement, $\delta s = (\delta x, \delta y, \delta z)$, is directly computed from and proportional to equations (3-3) but in opposite direction as to counter the velocity and eventually drive it to zero and satisfy the impermeability condition of the blade surface:

$$\delta s = -\omega v_{v,n} \delta t \tag{3-5}$$

Where ' δt ' is the user introduced transient time step size. The negative sign, as explained earlier, implies the opposite direction for the blade displacement. Figure 3.2 represents the blade movement schematically.

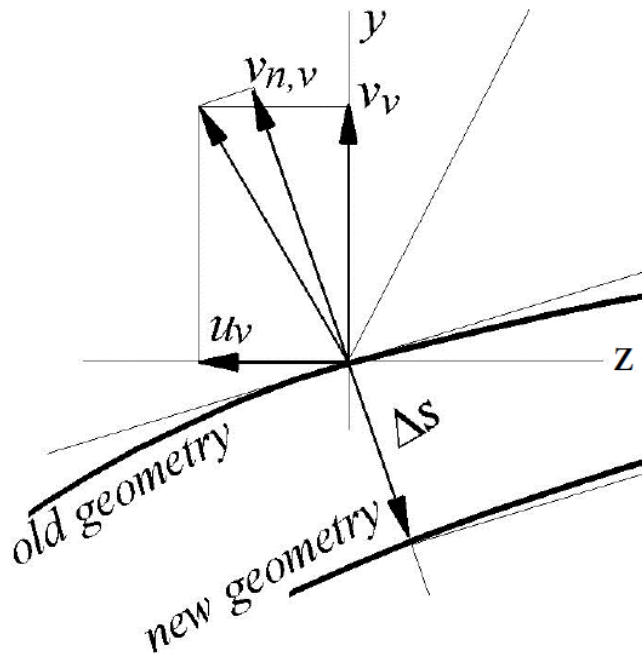


Figure 3.2. Schematic representation of wall movement

It is important to ensure that the 2D airfoils stay on their original spanwise plane so as to avoid crossing through each other and cause subsequent mesh issues especially near the end walls where the airfoils are congregated. This is done by maintaining the original radial position of the points which first requires the conversion from Cartesian to cylindrical coordinates. After having the virtual velocities converted to cylindrical coordinates, the modified blade geometry is constructed by applying the wall displacements at the discrete blade points:

$$r_{new} = r_{old} + v_r \delta t$$

$$\theta_{new} = \theta_{old} + v_\theta (1/r) \delta t \tag{3-6}$$

$$z_{new} = z_{old} + v_z \delta t$$

Where (r, θ, z) give the location of the discrete points in cylindrical coordinates. It is interesting to note that the present inverse formulation works well for inviscid as well as viscous flows, although the viscous flux terms were neglected in Eq. (3-1), and the balance of convective flux terms only was used to move the walls towards a shape that would satisfy the target pressure distribution [36]. It is believed that this is due to the fact that all the studied cases correspond to high Reynolds number flows where the viscous fluxes are negligible compared with the convective fluxes.

The next step depends on the choice of the design variable. Hence, the available choices of the design variables are presented first followed by the inverse design implementation.

3.2. Inverse design variables

In the current implementation, there are three choices of the design variables.

3.2.1. Target pressure loading and blade thickness distribution

This choice (referred to as DP design) consists of prescribing the blade pressure loading, DP, the blade thickness distribution and a stacking line which is a spanwise line through the camberlines of 2D sections at a specified fraction of chord. . Here the virtual velocity may not be computed directly from the difference between the current and target pressure loadings since the term ΔP in equations (3-3) and (3-4) refers to the difference between target and current static pressure of the suction or pressure surfaces of the blade. Hence, it is first required to derive the target static pressure from the target loading. After each design step, the target pressure distributions P^+ and P^- are updated using this target loading. Translation of the target loading to the static pressure of the suction and pressure surface is as follows:

$$P_{des}^{\pm} = \frac{1}{2}[(P^+ + P^-) \pm \Delta P] \quad (3-7)$$

Where \pm refers to the + (pressure) and – (suction) surfaces of the blade, as shown in Figure 3.3. In some cases the above equation may give a non-physical value for P_{des}^+ (for example in the presence of shocks, equation 3-7 will result in a pressure jump on the pressure surface) during the design process. In such occasions, the equation (3-7) could be written as:

$$\begin{aligned} P_{des}^+ &= P^+ \\ P_{des}^- &= P^+ - \Delta P \end{aligned} \quad (3-8)$$

Where the target pressure distribution for the pressure surface is directly taken from the time accurate solution of the simulation and the target loading distribution is used to obtain the target pressure on the suction surface of the blade.

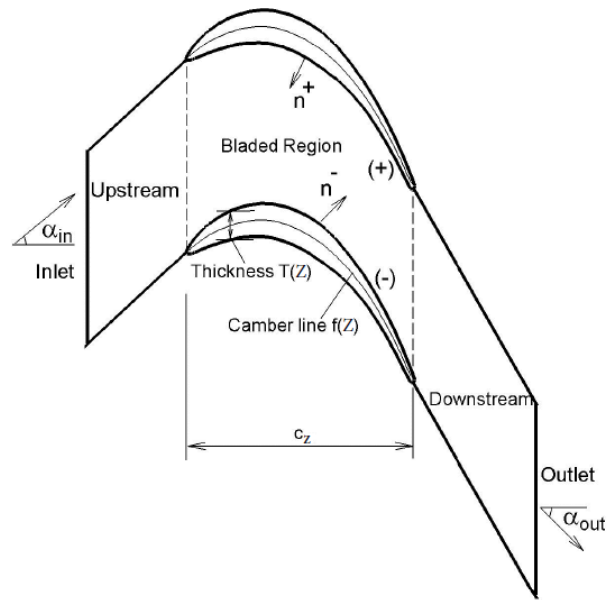


Figure 3.3. Blade-to-blade plane in a cascade

3.2.2. Target suction surface pressure and thickness distribution

The second choice of the design variables is prescribing a target pressure distribution on the blade suction surface, the thickness distribution and a stacking line (referred to as P- design).

This option is practical for blade design since the suction side pressure distribution predominantly dictates the blade performance; it gives more control on the flow over the blade and hence on the performance so that weakening of a shock or reducing a flow separation region can be achieved through the choice of P^- . On the other hand, as the pressure distribution on the blade pressure surface does not have a strong impact on the blade performance, the pressure obtained from the

URANS solution is imposed as target for the pressure surface at every time step which means no virtual velocity is computed, however this surface will still deform to satisfy the thickness constraint. The thickness distribution ensures that the blade is closed and allows for satisfying manufacturing and structural constraints.

3.2.3. Target pressure distribution on the blade pressure and suction surfaces

This choice consists of prescribing the target pressure distribution for both suction and pressure surfaces of the blade and a stacking line. Then the virtual velocity is directly computed from Eqs. (3-3). From the aerodynamic point of view, this choice of design variable works very well; however, since the target blade thickness distribution is not prescribed and it is left to be a part of the design solution, structural problems may rise. This is remedied by having the blade LE and TE shapes be specified by excluding the first and last 2% from inverse computations which is addressed in section 3.5.

3.3. Inverse design implementation

The blade movement is represented schematically in Figure 3.2. The resulting blade is scaled back to the original chord length. The discrete points are interpolated back to their original axial location (z-location), thereby the spanwise blade sections are essentially moving only in the tangential direction normal to the blade shape. For the first two choices of the design variables, the new normal camberline is then computed from the modified geometry.

After scaling the geometry back to the original axial chord length, the new tangential camber line is derived out of the new geometry which is used as the initial guess for normal camber

computation. The new normal camberline is now computed from the modified geometry and in two steps, one for the inversely designed part of the blade and one for the analyzed part of the blade where the blade shape is prescribed (see section 3.5), namely the LE/TE regions:

- *Designed part*: starting from tangential camber, at each camber point, the normal to the camber line and its intersection with the +/- surfaces are found using the aforementioned interpolation method. The normal distance from +/- surfaces is then evaluated, if the difference is within the prescribed tolerance, it means the point is located on the normal camber. If not, the point is adjusted in the tangential direction such that the difference is reduced. The whole procedure is repeated until the normal camber (and subsequently normal thickness) is obtained [37].
- *Analyzed part, i.e. the LE/TE regions*: The normal camber computed on the designed part is extrapolated at both ends and its intersections with the blade (i.e., actual *LE* and *TE*) are computed. The normal to the extrapolated portions are then computed and the intersection points with +/- surfaces (and subsequently normal thickness) are obtained (Figure. 3.4).

The next step is to ensure the smoothness of the camberline. The UDF is capable of constructing the 3D designed blade by two different approaches namely Morphing [38] and Fitting [39] approaches. If the designer chooses the fitting approach, there will be no need for any smoothing process as the fitting approach ensures the 3D camber surface is smooth in both streamwise and spanwise directions (section 3.4). If the designer chooses to use the Morphing method for the design process, the resulting camber profile is smoothed in two steps. The first step is to use the following elliptic form:

$$f_j = f_j + \omega_s[|f_{j+1} - f_j|(f_{j+1} - f_j) + |f_{j-1} - f_j|(f_{j-1} - f_j)] \quad (3-9)$$

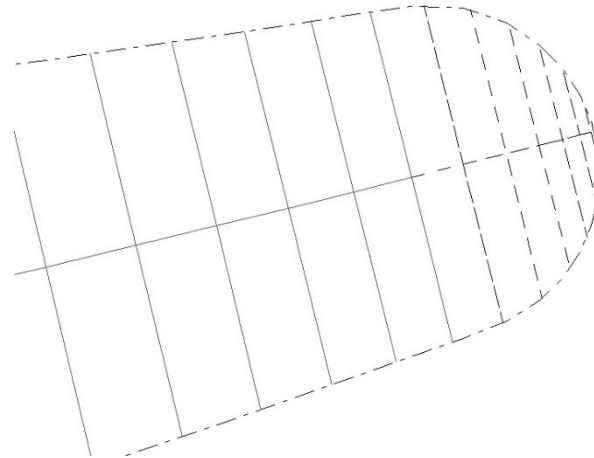


Figure 3.4. Normal camber & thickness: Solid line (Designed part of the blade) and dashed line (TE)

Where j refers to the position of the discrete points on the blade camberline which are sorted in an ascending order from minimum z to maximum z coordinate.

The typical value for the smoothing factor ' ω_s ' is 0.2 for subsonic flow and 0.05 for transonic cases. Using this smoothing factor helps to eliminate the possible small oscillations in the blade (or camber) geometry although it may delay design convergence.

As there might be still some high frequencies remaining over the camberline and in order to ensure a smooth camberline, high frequencies are removed at each time step by applying the following procedure:

The number of camber points (square symbols in Figure 3.5) are reduced such that only one point at each user defined percentage of chord (preferably 2-4%) is considered (triangle symbols in Figure 3.5). A B-spline curve [39] is then fitted through these nodes and the camberline is reconstructed by computing the x - and y - coordinates (spanwise and blade-to-blade coordinates respectively) corresponding to the axial location of the original number of nodes on the camberline. Once the camberline is smoothed, the discrete points are brought back to their original radial

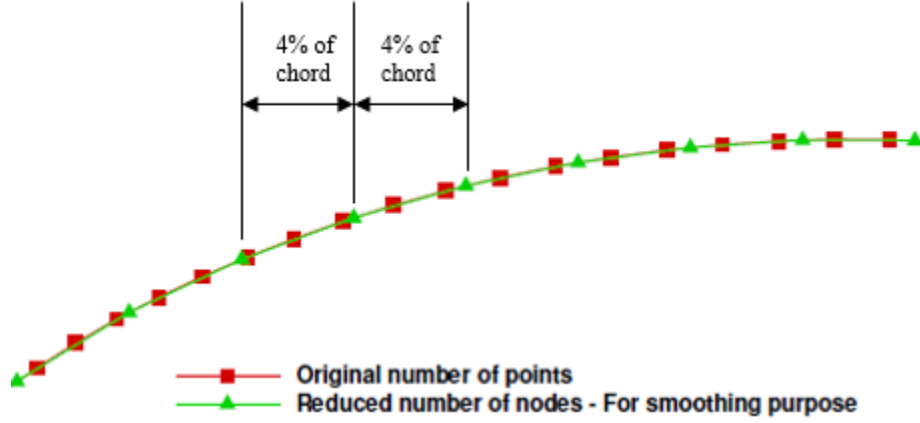


Figure 3.5. Camberline smoothing (High frequency removal)

position to make sure that airfoils maintain their spanwise position. The design constraints are then enforced, as detailed in section 3.5, before updating the final blade shape. The normal to the camberline at each discrete point is then computed and the prescribed normal thickness is added to the camberline in the normal direction (Figure 3.6). Considering the prescribed thickness to be the normal thickness of the original blade:

$$T_{Prescribed} = [(\Delta y_{PS-SS})^2 + (\Delta z_{PS-SS})^2]^{\frac{1}{2}} \quad (3-10)$$

where (α) is the angle of the normal to the camber with respect to the axial direction:

$$\alpha = \tan^{-1}(\Delta y_{PS-SS} / \Delta z_{PS-SS}) \quad (3-11)$$

the new blade surfaces may be generated as follows:

$$z_{new}^{\pm} = z'_{new} \pm 0.5 T_{Prescribed} \cos(\alpha)$$

$$y_{new}^{\pm} = y'_{new} \pm 0.5 T_{Prescribed} \sin(\alpha) \quad (3-12)$$



Figure 3.6. Airfoil reconstruction after adding normal thicknesses to the camberline

For the third choice of the design variables, in order to have smooth blade profile, the smoothing process is applied directly on the blade pressure and suction surfaces prior to computing the new normal camber line.

3.4.Reconstruction of the 3D designed blade

If the designer choose to design all spanwise airfoils, then the final 3D blade will automatically update as the new coordinates for all grids are obtained by implementing the inverse method. However, in many occasions the designer would like to ensure the loading along some spanwise sections hence the design variables are specified along these sections which brings on the issue of updating the remaining spanwise sections and so the final 3D blade shape. In this work for such cases, two different approaches are used for constructing the 3D designed blade shape:

One approach is the B-spline Morphing method which is used once the displacement field is computed for a certain number of airfoils from hub to the tip of the blade. This will provide the designer with the opportunity to only design a few spanwise sections rather than the whole blade. For this purpose and before implementing the inverse design at each step, the B-spline parameters (also known as natural coordinates) including the surface control points are first obtained. Then a robust and precise method called Global surface interpolation method (a B-spline surface generation method) is used to pass a surface through a certain number of airfoils (design sections) and obtain the B-spline representation of the blade. All the parameters values corresponding to the remaining spanwise sections (referred to as intermediate gridlines) are then computed by back interpolation. Upon implementing the inverse design and obtaining the new geometry for the chosen grids, B-spline Morphing method, which is a curve/surface reconstruction method is used to find the new coordinates of the intermediate gridlines [38]. The corresponding sections for the 2D and 3D interpolation and Morphing method are developed [40] and integrated into the main 3D inverse design code which is compiled with ANSYS-CFX. For example in Figure 3.7 there are 8 spanwise gridlines for rotor 67 which are inversely designed (the red curves) and the black grids or intermediate grids are obtained by Morphing method.

The second method is the Fitting approach which is a least square curve fitting method. This method is applied on the normal camberlines instead of the airfoil profile. First and before implementing the inverse design method, B-spline parameters are obtained for all the camberlines and then the fitting approach is used to best fit curves in streamwise direction through the camberlines and obtain a predefined number of control points in that direction for each. Then the approach is used again to best fit curves, through the previously obtained control points, in the spanwise direction and new surface control points in spanwise direction are computed. Computed

control points and parameters are saved and the whole process is repeated after the design and this time on the design camberlines only. The B-spline parameters on the original geometry that were computed and saved, along with the new surface control points obtained for the camberlines after the design are finally used to obtain the new coordinates of all camberlines which are all smooth in both streamwise and spanwise directions. Figure 3.8 shows the streamwise and final 11×8 spanwise (surface) control points for the NASA transonic rotor 37 after the design from which the final coordinates of the camberlines are calculated. It is notable that in Figure 3.8 the streamwise control points (black lines) are plotted for a few design sections only.

It is also worth mentioning another difference between Morphing and Fitting approaches. The former is more accurate in terms of target satisfaction because of the approximation embedded in

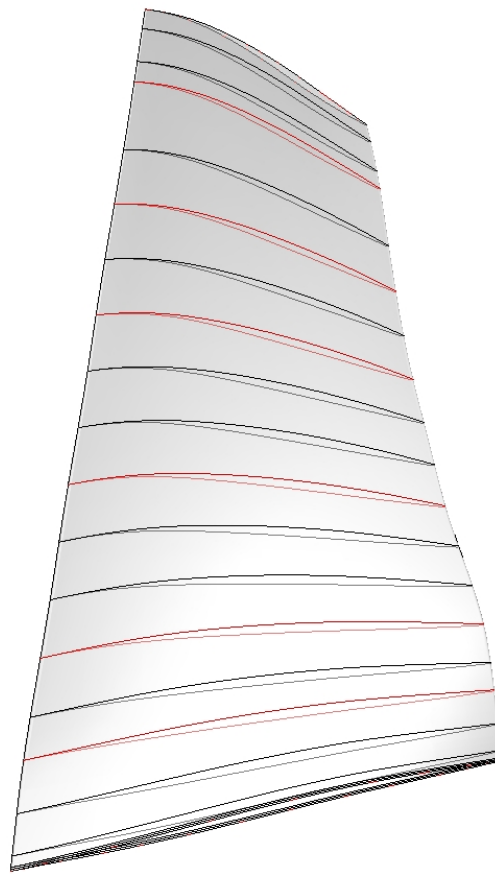


Figure 3.7. Design (red) and intermediate (black) gridlines for Rotor 67

the Fitting approach. When using Morphing method, the 3D surface will pass through every single node on the design airfoils while in Fitting approach, as explained, a curve is best fitted through the control points hence the final geometry might be slightly different from what comes out of the inverse design method. However using Morphing method requires more care as to obtain a smooth shape at the end of the design. Hence, the HFR (High Frequency Removal) process for smoothing purpose is only applied when using Morphing method.

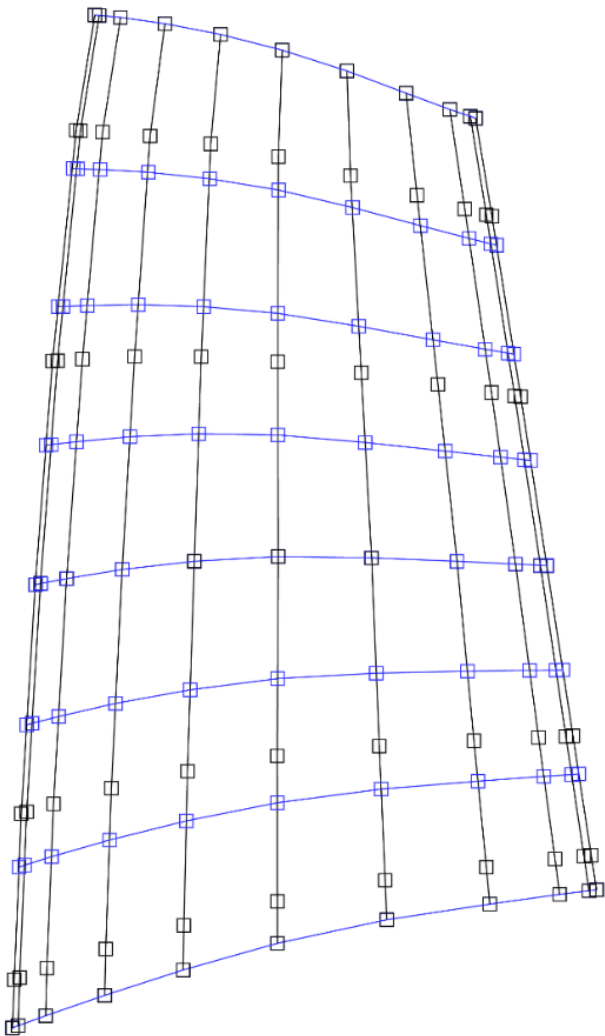


Figure 3.8. Streamwise (black) and spanwise (blue) control points for NASA Rotor 37

3.5. Design constraints

An arbitrary choice of target pressure distribution does not necessarily mean that the inverse design problem is well posed. For external flow as shown by Mangler [41], Lighthill [42] and later on by Volpe *et al.* [43], an arbitrary choice of the target pressure distribution may lead to crucial geometrical problems especially near the LE/TE regions of the blade where if proper care is not ensured, the design process may lead to an open leading edge or a trailing edge crossover. In the current method, in order to avoid facing this problem, the part between 1%-3% and 97%-99% of the axial chord is inversely designed while the remaining parts which fall in the LE/TE regions of the blade are analyzed, i.e. no design is done in these regions. In order to ensure camberline smoothness at the transient points, the slope of the camber line and the blade thickness are matched with those prevailing from the design region [25].

Also for the cases where there is tip clearance, because of the flow uncertainties and the adverse spanwise pressure gradient near the tip, the design is implemented from the hub to 98% span and the last 2% span is obtained by extrapolation [33].

3.6. Inverse design algorithm

ANSYS-CFX is first used to simulate the flow through compressor and turbine stages and the results thus obtained are compared with the available experimental data. Following that assessment, the inverse design method was implemented in ANSYS-CFX using the time accurate Eulerian-Lagrangian formulation of RANS equations [35].

Figure 3.9 shows the inverse design iterative process where the block on the right constitutes the inverse design module. The design module starts from a converged flow solution on an initial

geometry and the design (target) parameters e.g., the blade pressure loading and normal thickness distributions and stacking line. The difference between the target and the current design pressures are used to compute the virtual velocities. The virtual wall velocities are then translated into displacements that are used to modify the airfoil shape. The next step is to remesh the computational domain to match the new blade shape. The grid velocities are computed from mesh conservation Law [44]. The grid velocities are added on to the governing equations and, at each time-step, the stationary problem is solved until the residuals reach a predetermined convergence level. The design and target pressures are compared and the whole process is repeated until the L_2 -norm of either the grid displacement or the pressure change along the blade are within an acceptable tolerance value; this ensures that the airfoil has asymptotically reached a shape that would satisfy the target pressure distribution in a least squares sense.

The inverse methodology is embedded into ANSYS-CFX using a Junction Box (JB) routine. At each physical time-step, the blade geometry and flow parameters are called from within the JB routine. The spanwise airfoils are then identified inside the JB and a B-spline curve [19] is fitted once through the suction and pressure sides of each airfoil, to generate the same number of nodes on each side and in the same axial location (referred to as design mesh), and once through the pressure distribution curve of each side of the airfoil to obtain the pressure values corresponding to the design mesh. The blade loading distribution is then obtained by computing the static pressure difference at each axial location as well as the tangential camberline of each airfoil which, as explained before, is used as the initial guess for the normal camber computations.

The airfoil displacements are then computed using the inverse technique detailed earlier in this chapter. The designed airfoils are interpolated back to their original number of nodes (CFX mesh) and axial location and the new coordinates are then stored in CFX Memory Management System

(MMS) and returned to ANSYS-CFX by user "CFX Expression Language" CEL function for computing the mesh displacement (remeshing) and converging the stationary problem on the new airfoil shape. The physical time-step is then incremented and the process is repeated until the L_2 -norm of either the grid displacement or the pressure change along the blade has reached the tolerance value. The mesh quality is controlled by introducing a variable mesh stiffness (see section 2.1) that is inversely proportional to the distance away from the wall, so that it is maximum near the wall and minimum away from the wall. This ensures that the mesh quality and spacing near the wall remains almost unchanged as the blade wall moves [33].

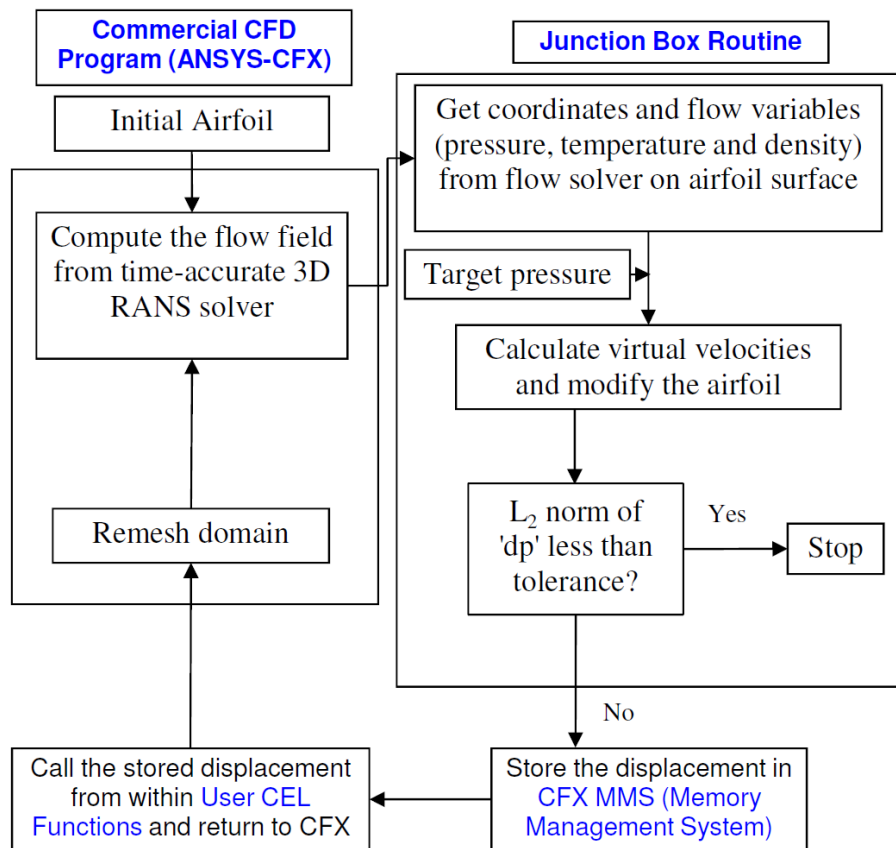


Figure 3.9. Computational algorithm for 3D inverse design

3.7. Challenges associated with 3D inverse design versus 2D inverse design

Extending the 2D inverse design to the inverse design in three-dimensional flow involved challenges throughout the development of the inverse design methodology and functions. In order to pass the blade coordinates and the flow variables back and forth between the CFD solver and the UDF, an interface was first needed for effective communication between the two. To do so, hundreds of lines of FORTRAN code was developed including data acquisition subroutines that are not available in CFX documentations. After several months of intensive effort and research the interface was created to properly receive the information from the solver, store the displacement in CFX Memory Management System (MMS) and return them to the solver to update the computational domain. Four different FORTRAN routines have been used for this purpose while in 2D inverse design the whole process was performed using a single routine connecting the UDF to the solver without the need for complicated acquisition routines.

Also, as mentioned in section 3.3, the tangential thickness and camberline computations were replaced with normal thickness and corresponding normal camberline computations. This single step was accomplished by over three thousand lines of programming including the development of algebraic algorithms and multiple times of interpolations to find the intersection point of the normal to the camber with the blade surface.

Integrating the blade reconstruction methods, namely Morphing and Fitting approaches, into the UDF and overcoming the resultant numerical errors and approximations was another important step in developing the 3D inverse design methodology.

These were just a few important challenges to mention and add to it the target pressure loading generation, the blade profile generation from bunch of raw data available in the literature and countless algebraic and geometrical issues confronted throughout the work.

Chapter 4

Validation of the Methodology & Design Convergence

The inverse design methodology and implementation was validated for four test cases. The transonic NASA Rotor 37 [45], the stator of the first stage of a two stage fan (Stage 67) which was designed and tested at NASA Lewis Research Center [46], the rotor blade of subsonic E/CO-3 compressor stage which was designed and tested at Rolls Royce compressor test facility and the rotor and stator blades of a low speed axial flow turbine stage [47] were selected for this purpose.

The goal was to demonstrate the capability and usefulness of the present inverse scheme in the redesign of compressor and turbine stages using the commercial CFD program ANSYS-CFX.

ANSYS-CFX was first run in analysis mode for all these cases. NASA Rotor 37 was then used to validate the inverse design methodology and its implementation into CFX. Once the implementation was validated, the inverse method was assessed in the design of stage 67 stator. Note that as the first design case, stator 67 was analyzed and redesigned as a single blade row for which arbitrary boundary conditions corresponding to well-behaved subsonic flow field were used.

The method was then further assessed in the redesign of E/CO-3 compressor and E/TU-3 turbine stages. By modifying the pressure loading or static pressure distributions on the blade surfaces, the inverse approach was used to design the blade into a desired shape which satisfies the prescribed target; this is achieved by calling the Junction Box (JB) and the CFX Expression Language (CEL) functions for the blade rows to be designed. In summary, this chapter addresses the inverse method validation and its use in the redesign of stage 67 stator, E/CO-3 compressor and E/TU-3 turbine

stages to assess the design convergence.

As the purpose of this chapter is to demonstrate the capability of the method to inverse design 3D blades and satisfy the prescribed target function, hence neither the analysis results nor the aerodynamic performance of the designed blades are discussed and are left to be presented in the next chapter.

4.1. Validation of the inverse design implementation in ANSYS-CFX

The inverse design method was implemented into CFX using the JB Routine and the user CEL functions. The JB and CEL allow for extracting the flow variables and geometry parameters, implement the design method and return the new blade geometry. NASA Rotor 37 was used to verify the consistency of the inverse methodology and validate its implementation by two different approaches for constructing the 3D designed blade namely Morphing and Fitting approaches.

The blade consisted of 51 spanwise airfoils, each with 273 nodes. Figures 4.1 and 4.2 respectively illustrate the mesh near the rotor hub and tip sections. The rotor tip gap is 0.356 mm (0.5% span) and as explained in section 3.5 the design is implemented up to 98 % span and the last 2% span is obtained by extrapolation. Also the first 2% span is obtained by interpolation which means the airfoils located at the hub and 2% span are designed and the airfoils between them are obtained by Morphing method. This is done because airfoils are clustered near the hub and interpolation ensures the blade smoothness in spanwise direction. For all other spanwise sections (between 2% - 98%) the pressure loading distribution that is obtained from the 3D flow simulation on the original NASA Rotor 37 geometry is specified as the target loading distribution. In this case, when CFX is run in design mode starting from the original geometry, the virtual velocity and hence the

blade displacement would be (and should continue to be) zero, hence the L_2 -norm of displacements will also be zero and the geometry will remain unchanged. However, due to the blade smoothing which is done by applying the HFR (High Frequency Removal) process and add to it a few steps of back and forth interpolation on the spanwise airfoils, a minor displacement is introduced to the blade geometry which is not affecting the performance and it is a safe action to take to obtain a smooth blade shape and pressure distribution. The validation was performed by inversely designing Rotor 37 for 400 design steps and verifying that the L_2 -norm of the blade displacement remained in the order of 10^{-5} (Figure 4.3) while the L_2 -norm of DP remained in the order of ($10^{-3} - 10^{-2}$) as shown in Figure 4.4. Figure 4.5 shows the original and the designed loading distribution for the airfoils located at the hub, 60% and 100% blade spans. The resulting airfoil shapes are shown in Figure 4.6 where the agreement between the original and the design geometry and loading distributions indicate that the geometry has remained unchanged throughout the all 400 design steps.

It is also notable that there is no limitation for the number of design steps and validation could have continued further but since the design and solver residuals showed a steady trend throughout the run it was expected to obtain the same results after any number of design steps.

Once again the inverse design methodology was validated and this time using the Fitting approach [33] and on the same geometry and with the same design conditions (i.e., the same design variables, times step size, etc.) where 8 spanwise and 11 streamwise control points were used to reconstruct the designed blade (Figure 3.8). Since the results obtained by both approaches were almost identical only those for Morphing method are provided in this thesis. The validation performed by making use of the Fitting approach is presented in Appendix A [33].

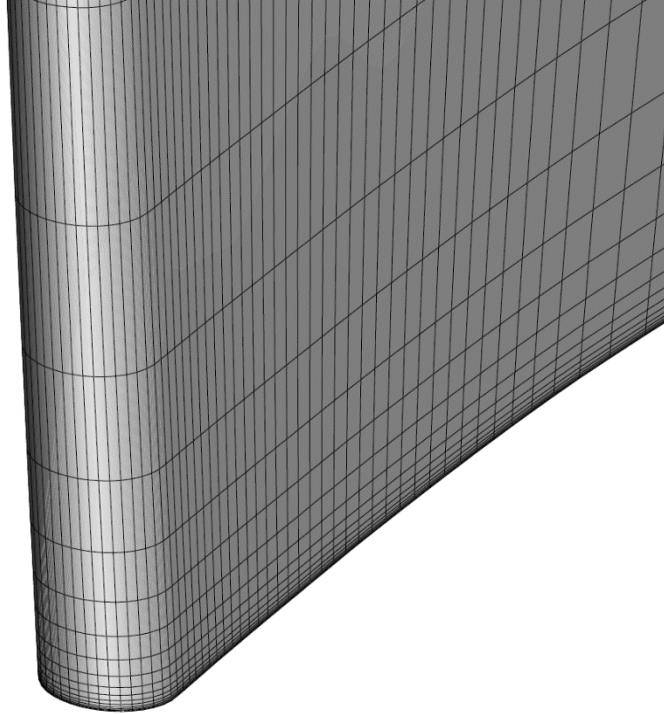


Figure 4.1. Rotor 37: Mesh close-up near the LE of the hub

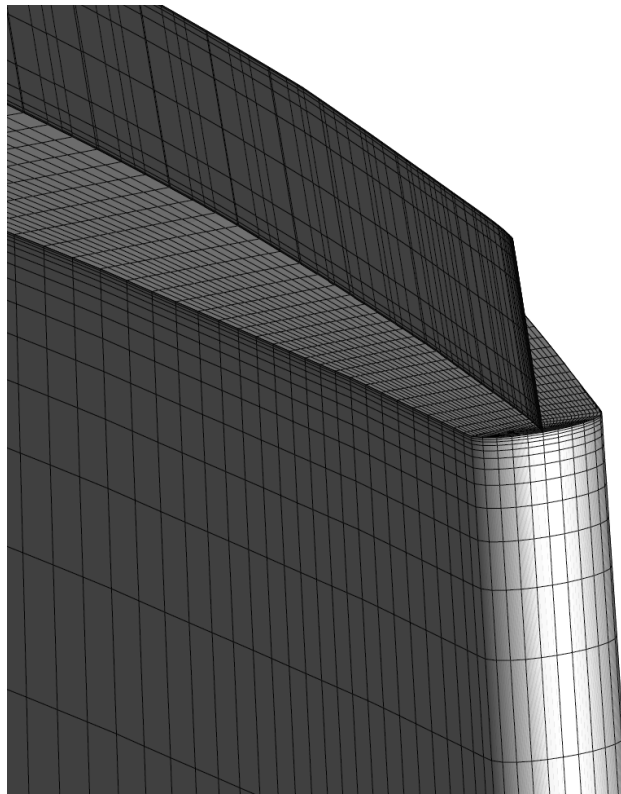


Figure 4.2. Rotor 37: Mesh close-up near the TE of the tip

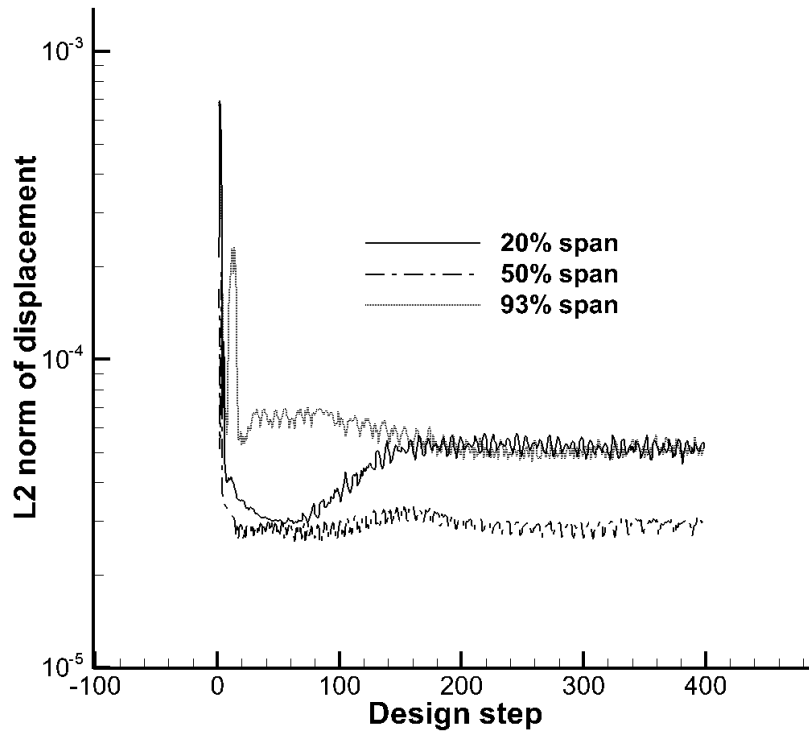


Figure 4.3. Rotor 37: L2 norm of Displacement

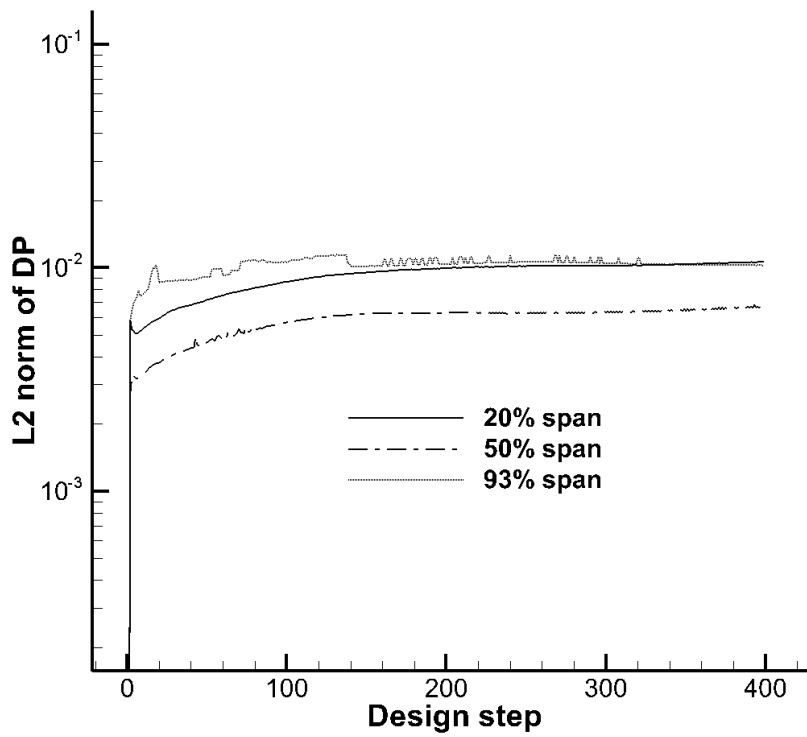
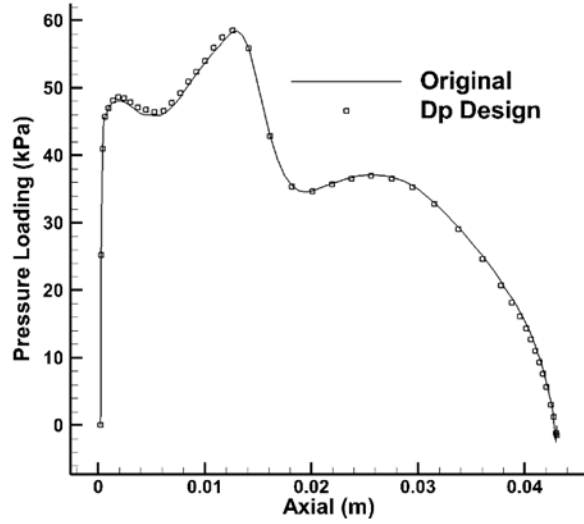
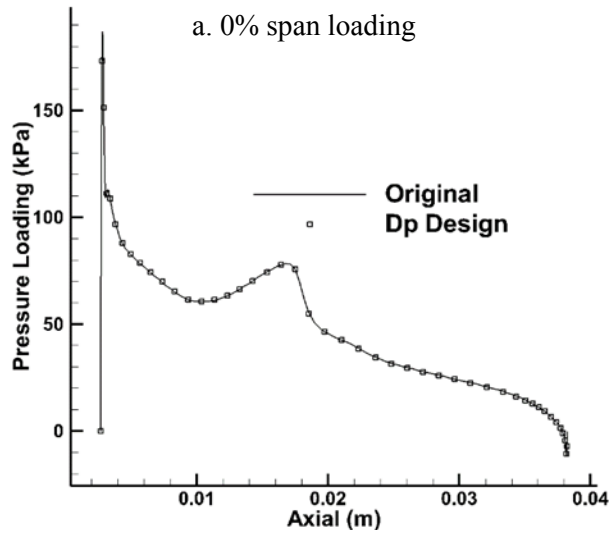


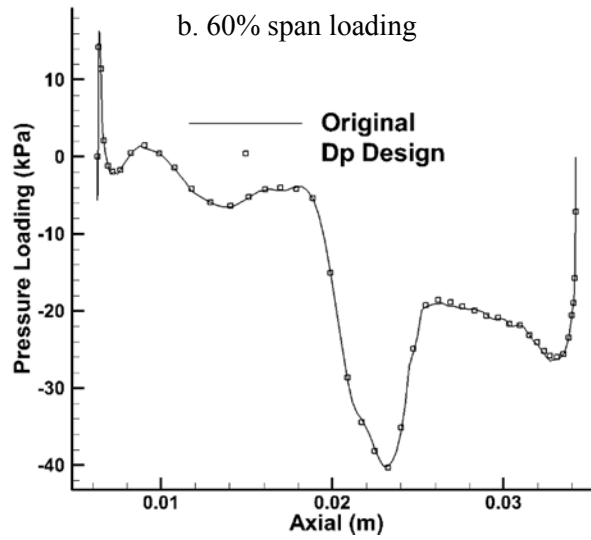
Figure 4.4. Rotor 37: L2 norm of DP



a. 0% span loading



b. 60% span loading



c. 100% span loading

Figure 4.5. Rotor 37 validation: Original and design pressure loading

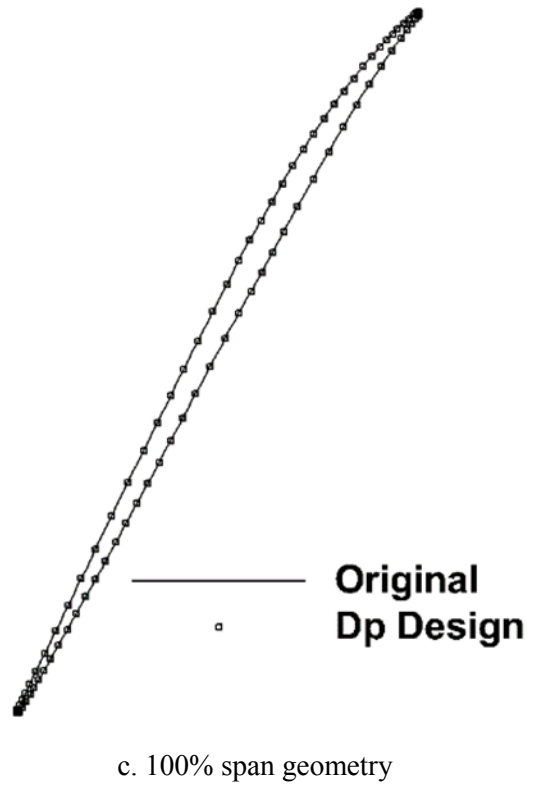
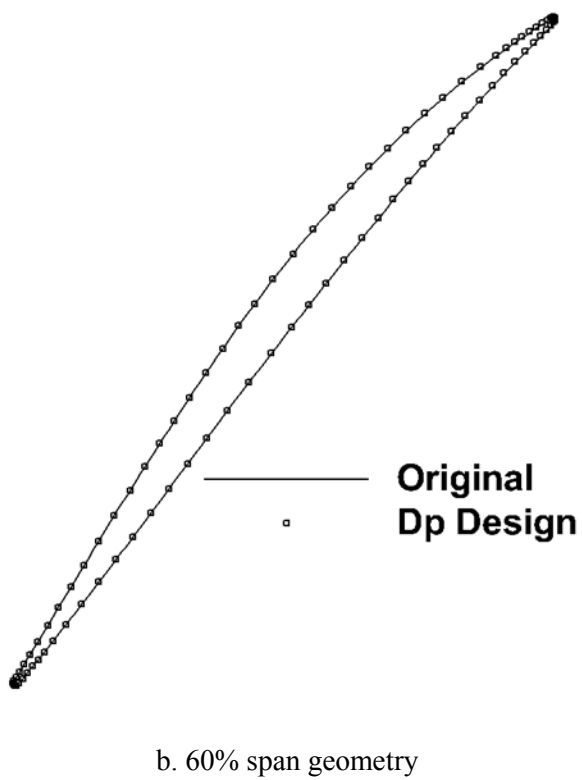
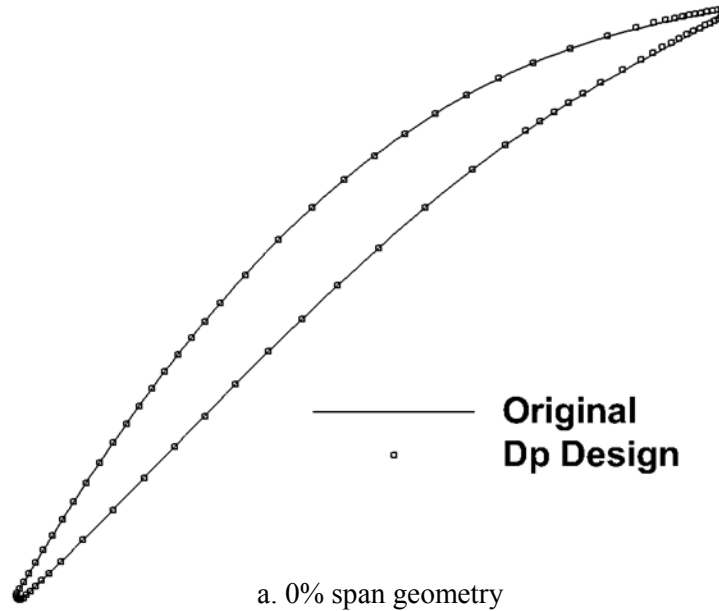


Figure 4.6. Rotor 37 validation: Original and design airfoil geometry

4.2.Redesign of the stator 67 as a single blade row

As the first reloaded 3D inverse design case, the method was applied to the redesign of the stage 67 stator as a single blade row where the design variables are target loading distribution, blade thickness distribution and stacking line at 40% of the axial chord. This blade consisted of 21 spanwise airfoils, each with 281 nodes. Three airfoils located at hub, mid-span and tip are designed and the remaining airfoils (or intermediate airfoils) are obtained by interpolation and Morphing method. The problem took 150 design steps, equivalent to about two flow simulations, to satisfy the target with more than 90% of accuracy. Figures 4.7 and 4.8 show and compare the original and design airfoil geometry and pressure loading at hub, mid-span and the tip.

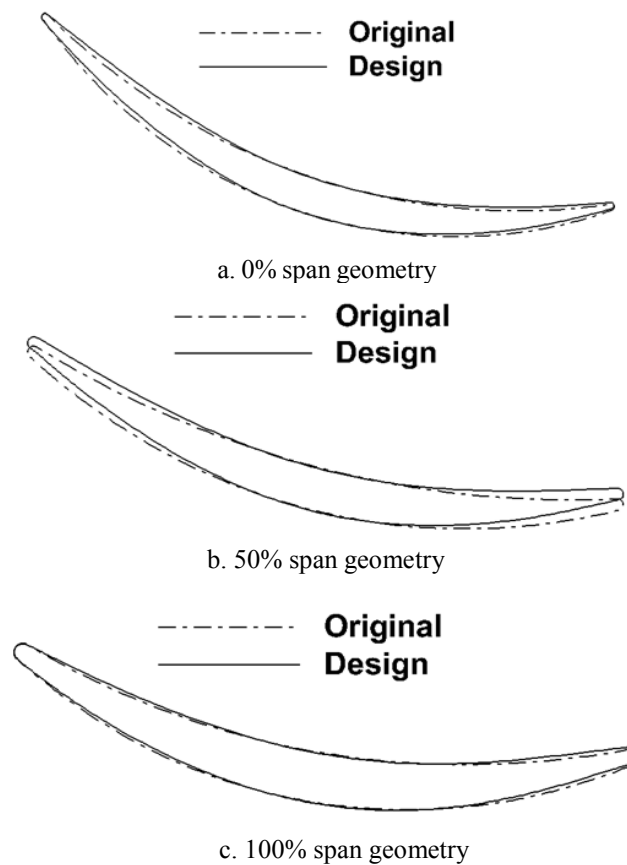
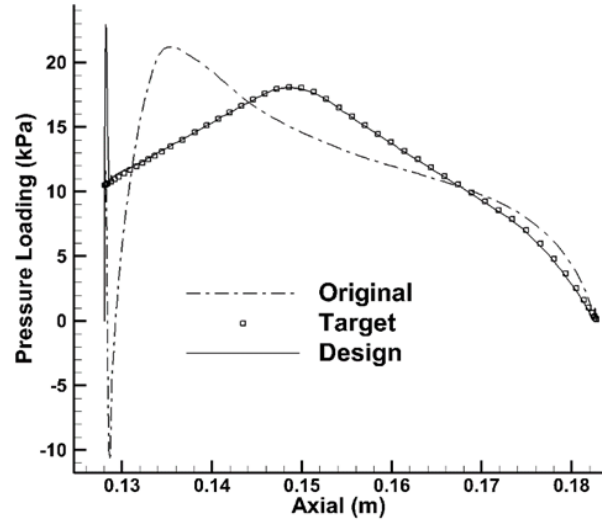
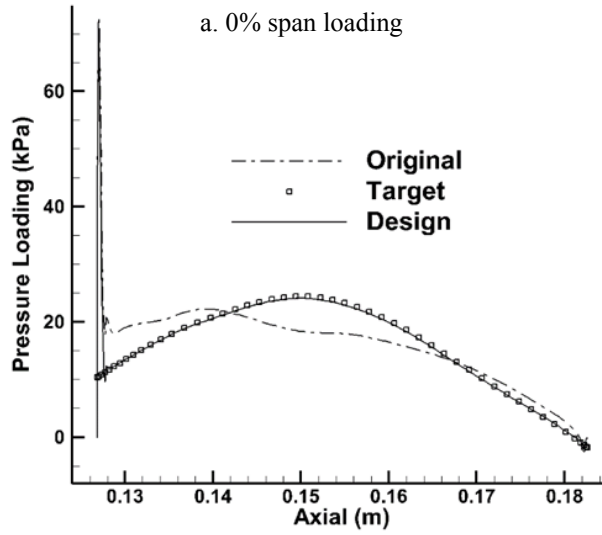


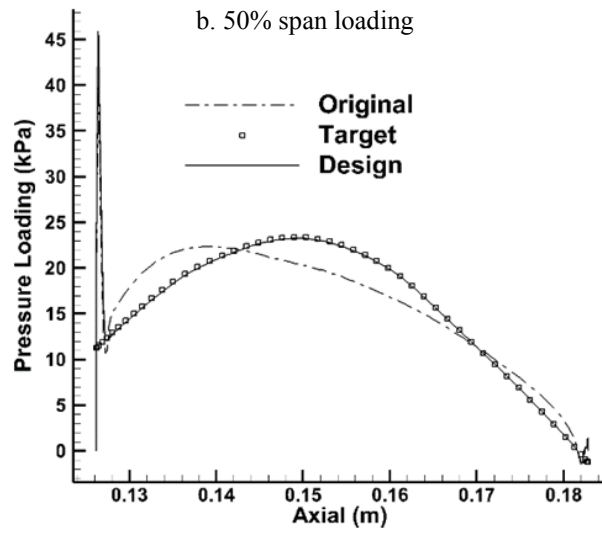
Figure 4.7. Stator 67: Original and design spanwise airfoils



a. 0% span loading



b. 50% span loading

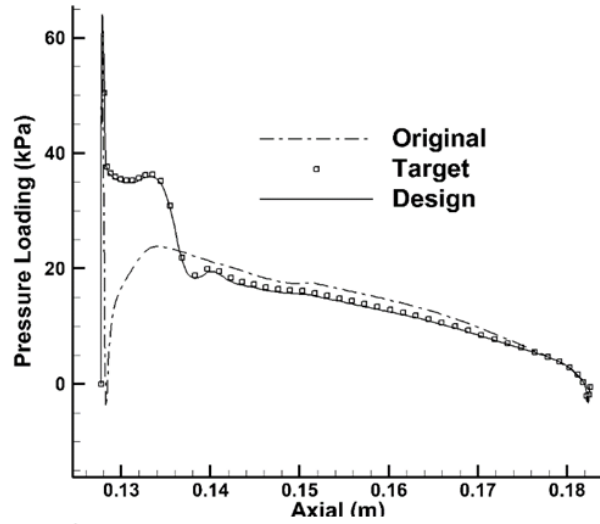


c. 100% span loading

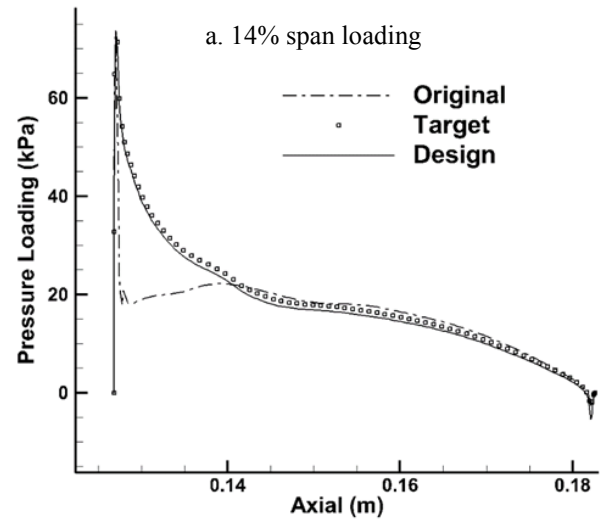
Figure 4.8. Stator 67: Original, target and design loading distribution

It can be understood from Figures 4.7 and 4.8 that the repositioning of the maximum pressure loading towards the mid-chord has been transposed into the geometry where the maximum camber has moved accordingly.

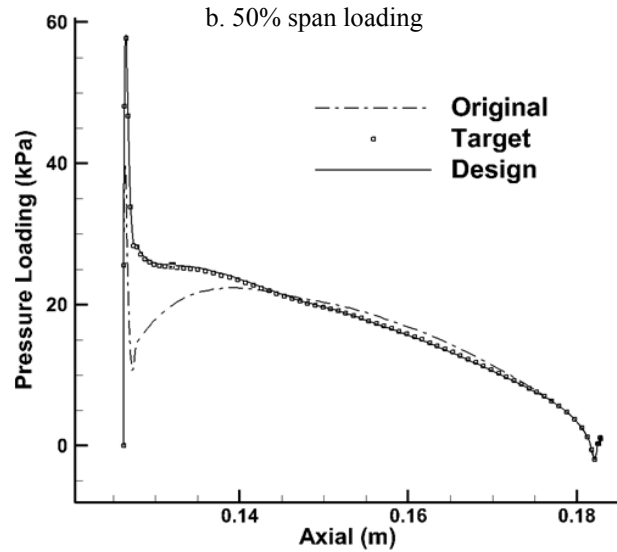
The method was further evaluated with an incidence increase by changing the inlet flow angle by a few degrees. The goal was to design a 3D blade geometry which is rotated enough in a direction such that the flow incidence angle increases and matches with that of the steady state solution and consequently satisfies the target. Then CFX was run to obtain the steady state solution for the new boundary condition and on the original geometry. The loading thus obtained was set as the target loading and inverse design started from the original blade geometry and original inlet flow angle as boundary condition. This time, nine spanwise airfoils were designed and the rest obtained by interpolation. The goal was achieved after 200 design steps. It was also observed that the higher input values for relaxation factor and time step size could help reduce the required number of design steps to satisfy the target, but care should be taken not to choose the values too large and destabilize the problem. Figures 4.9 and 4.10 show the original and design pressure loading and airfoil geometry at three designed sections located at 14% and 50% and 86% blade span. It can be seen from Figure 4.10 that the spanwise airfoils were rotated in the desired direction and satisfied the target by more than 90% of accuracy. Two points to be noted here: First, the use of the term "rotation" does not mean that the airfoil has simply rotated as a whole, but the blade has deformed based on the point by point difference between the instantaneous (current) and target pressure values which has finally shaped the resultant geometry. The second point is that although the inlet flow angle had changed uniformly from hub to tip, the spanwise airfoils do not rotate uniformly as well, especially near the hub and tip due to the flow uncertainties and boundary layer effects.



a. 14% span loading



b. 50% span loading



c. 86% span loading

Figure 4.9. Stator 67: Original, target and design pressure loading

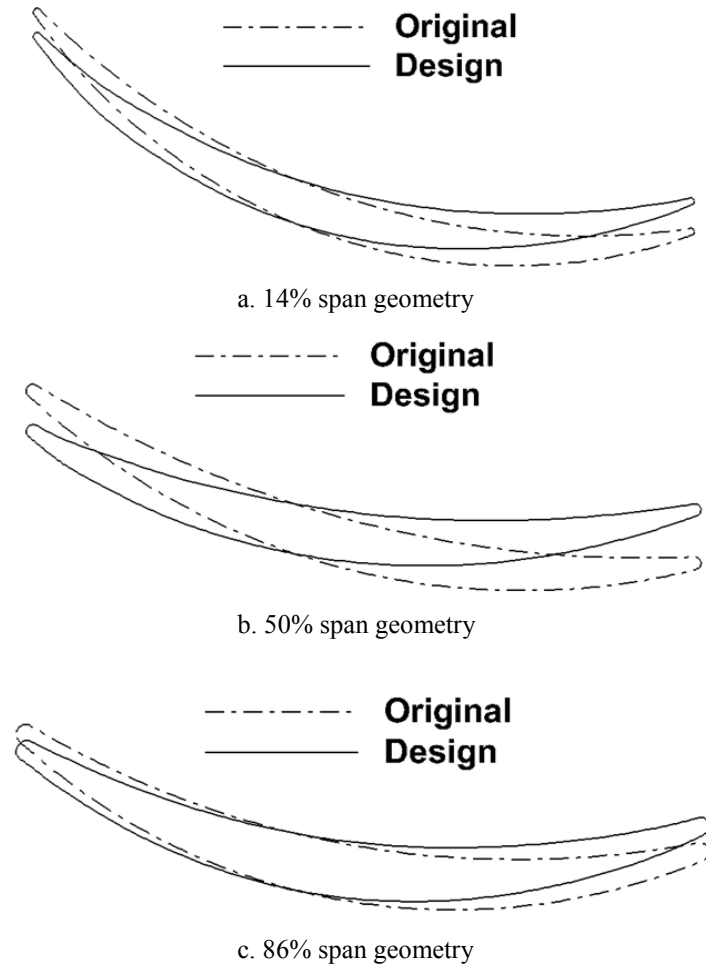


Figure 4.10. Stator 67: Original and design airfoil geometry

4.3. Redesign of the E/CO-3 compressor rotor

The inverse design method was then used to redesign the E/CO-3 compressor stage [47]. The rotor was redesigned at design conditions while the stator blade shape was fixed. The design variables were target pressure distribution on pressure and suction surfaces and the stacking line at the blade LE. The target was prescribed such that the pressure surface maintains the original pressure distribution unchanged while the peak Mach number over the suction surface is lowered and

shifted downstream. The blade consists of 31 spanwise airfoils out of which six airfoils located at hub, 15%, 40%, 60%, 85% and 98% span are designed and the rest between 0-98% span are to be obtained by interpolation and Morphing method. Because of the blade tip clearance, as said in section 3.5, the last 2% is excluded from the design and it is obtained by extrapolation. Figures 4.11 and 4.12 show the original and design static pressure and geometry of two airfoils at 40% and 85% span. The problem needed 95 design steps to converge and satisfy the target on +/- surfaces by about 80%. As mentioned in section 3.2, in this choice of design variables the thickness is the design solution and Figure 4.12 clearly shows that the design thickness differs from the original blade. Another observation from Figures 4.11 and 4.12 is that although the blade PS keeps the original pressure distribution unchanged, the original and design geometry are not the same. This indicates that the geometry change of one surface or one spanwise section, is affecting the flow on the other surface or other spanwise section.

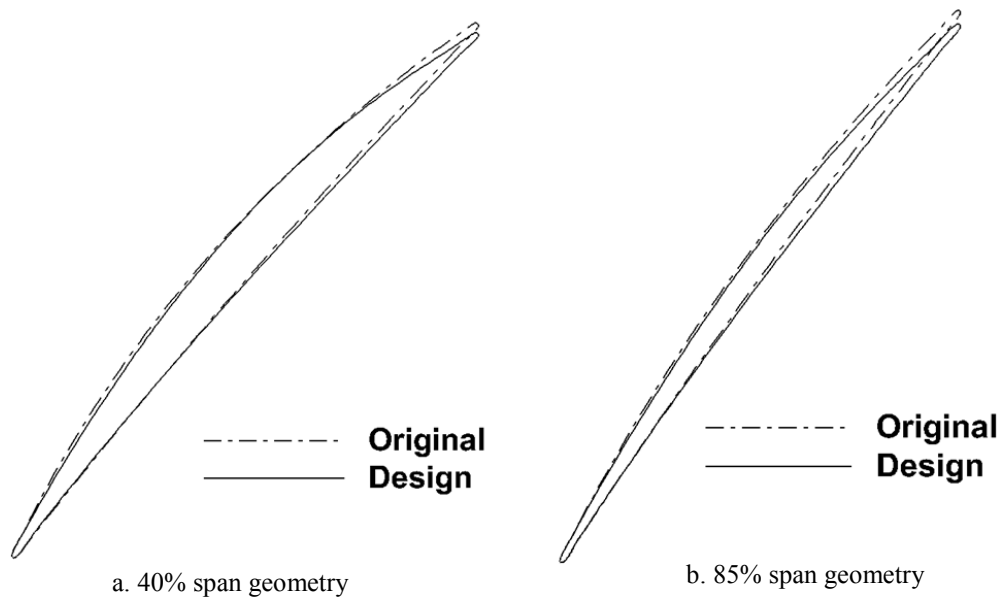
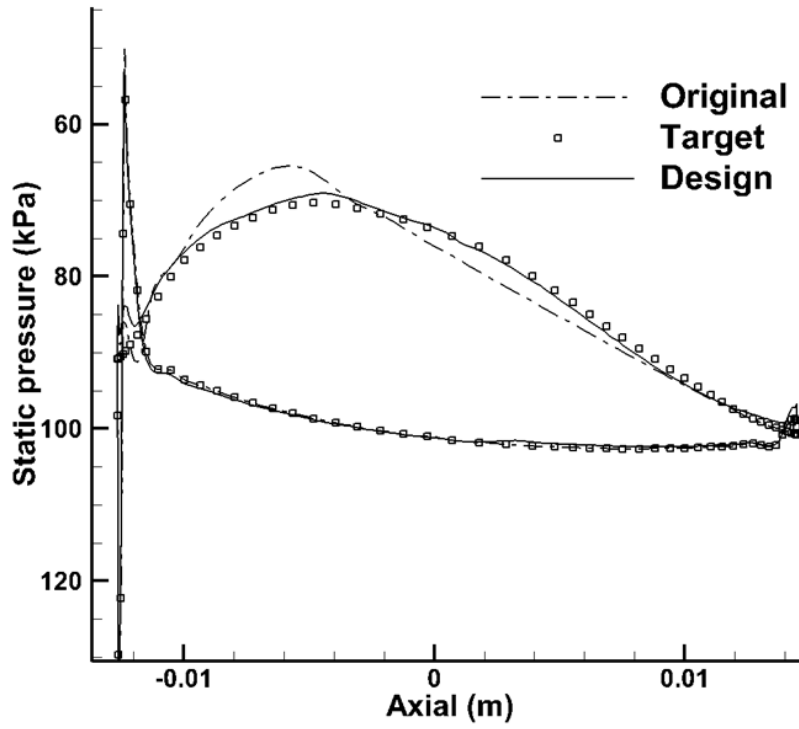
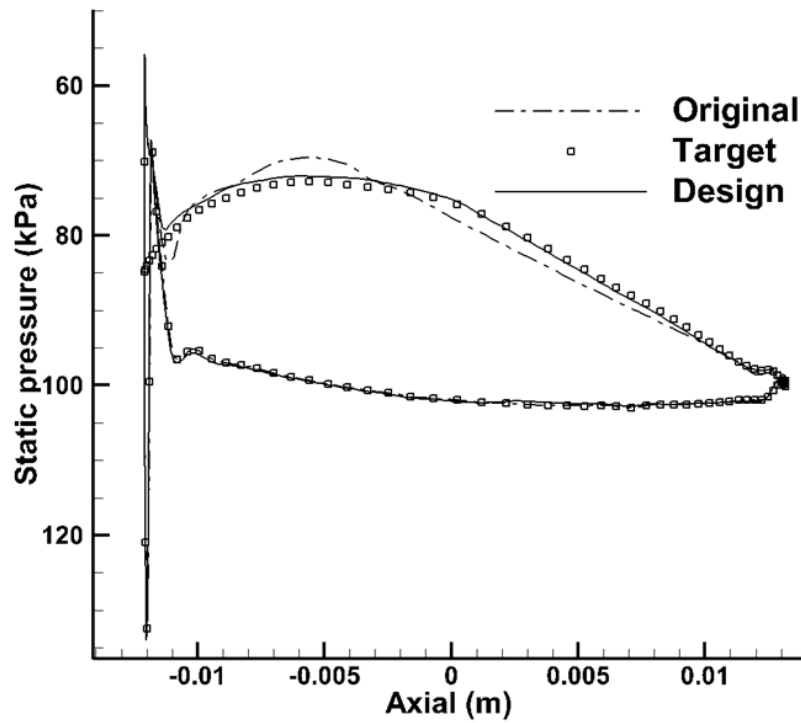


Figure 4.11. E/CO-3 Compressor Rotor: Original and design static pressure



a. 40% span static pressure



b. 85% span static pressure

Figure 4.12. E/CO-3 Compressor Rotor: Original and design airfoil geometry

After successful implementation of the inverse design method into the redesign of compressor stages, the method was used to redesign the E/TU-3 turbine stage [47].

The rotor was redesigned first while the stator blade shape was fixed, then the rotor was fixed and the stator was redesigned.

4.4. E/TU-3 turbine rotor redesign

The rotor blade is consisted of 38 spanwise airfoils with 215 nodes on each. Six almost equally spaced airfoils in the spanwise direction were selected to be designed while the rest are obtained by Morphing method and interpolation. The rotor blade is run without tip clearance hence the tip section (100% span) is one of the design sections and there is no need for extrapolation in this case. The design variables are target SS pressure distribution, normal thickness distribution and stacking line at the LE. The HFR process is applied at each 2% chord for the smoothing process. It took only 45 design steps for the problem to converge by 90%. Figures 4.13 and 4.14 show the original and design airfoil geometry and static pressure distribution at two designed sections located at 35%, 55% blade span.

4.5. E/TU-3 turbine stator redesign

The stator blade consisted of 46 spanwise airfoils, each with 208 nodes. Five spanwise airfoils were selected to be designed while the rest are obtained by Morphing method and interpolation. Similar to the rotor blade, the stator also is run without tip clearance hence the tip section (100% span) is one of the design sections. The design variables are target loading distribution, normal

thickness distribution and stacking line at the LE and similar to the rotor design the HFR process is applied at each 2% chord for the smoothing process. After 45 design steps the problem converged by about 80%. Figures 4.15 and 4.16 show the original and design airfoil geometry and loading distribution at two designed sections located at 45%, 80% blade span.

At this point it is beneficial to address an advantage of the inverse method versus analysis method which has been a common question. Figure 4.16a shows a clear difference between the original and design pressure loading where the peak loading is reduced and shifted upstream. However, it is very difficult to distinguish between the original and design blade geometry shown in Figure 4.15a. To make these kind of tiny geometry modifications by analysis method would be extremely difficult and time consuming, if not impossible. Although the designer could select as minimum as three design airfoils, the shape of the blade and its parametric variation in spanwise direction such as stagger angle and thickness could enforce the selection of more number of design sections to avoid structural issues when interpolating the intermediate airfoils.

4.6. Concluding remarks

Let us recognize that the target blade shape would exist only if the target pressure distribution is realizable (hence physical), therefore the L_2 -norm of either the mesh displacement or the pressure change with time can decrease or increase depending on whether the target pressure distribution is 100% realizable or not. That is why the prescribed target pressure will not be satisfied with 100% accuracy if the target pressure is the designer input which does not necessarily correspond to a real geometry. Add to it the numerical errors arising from multiple back and forth interpolations, 3D blade reconstructions etc. Moreover, the level at which this L_2 -norm will level off expresses how

well the design pressure has reached the target one [28]. For the compressor redesign cases presented in this section, the L_2 -norm of DP, which is the difference between the current (instantaneous) and target pressure distribution in a least square sense, was reduced by about an order of magnitude on average (means target satisfaction by 90%). The observations however have shown that convergence by 70% is enough to attain the main features of the prescribed target e.g., the peak loading, pressure gradient and incidence angle.

A second note that is specific to the present approach to inverse design is the following. As mentioned previously in the Abstract, The inverse design process is an unsteady process with the blade displacement being the source of unsteadiness. Hence, the design process was interrupted a few times, when the L_2 -norm of DP levels off, and the designed blade (at that stage of the design) was run in analysis mode so as to remove any accumulated flow unsteadiness during the transient run. The design process was then continued from the latest obtained designed blade. This process replaces the instantaneous flow field with a steady state one; it is used when the design convergence starts leveling off and was found to improve convergence [28], [35].

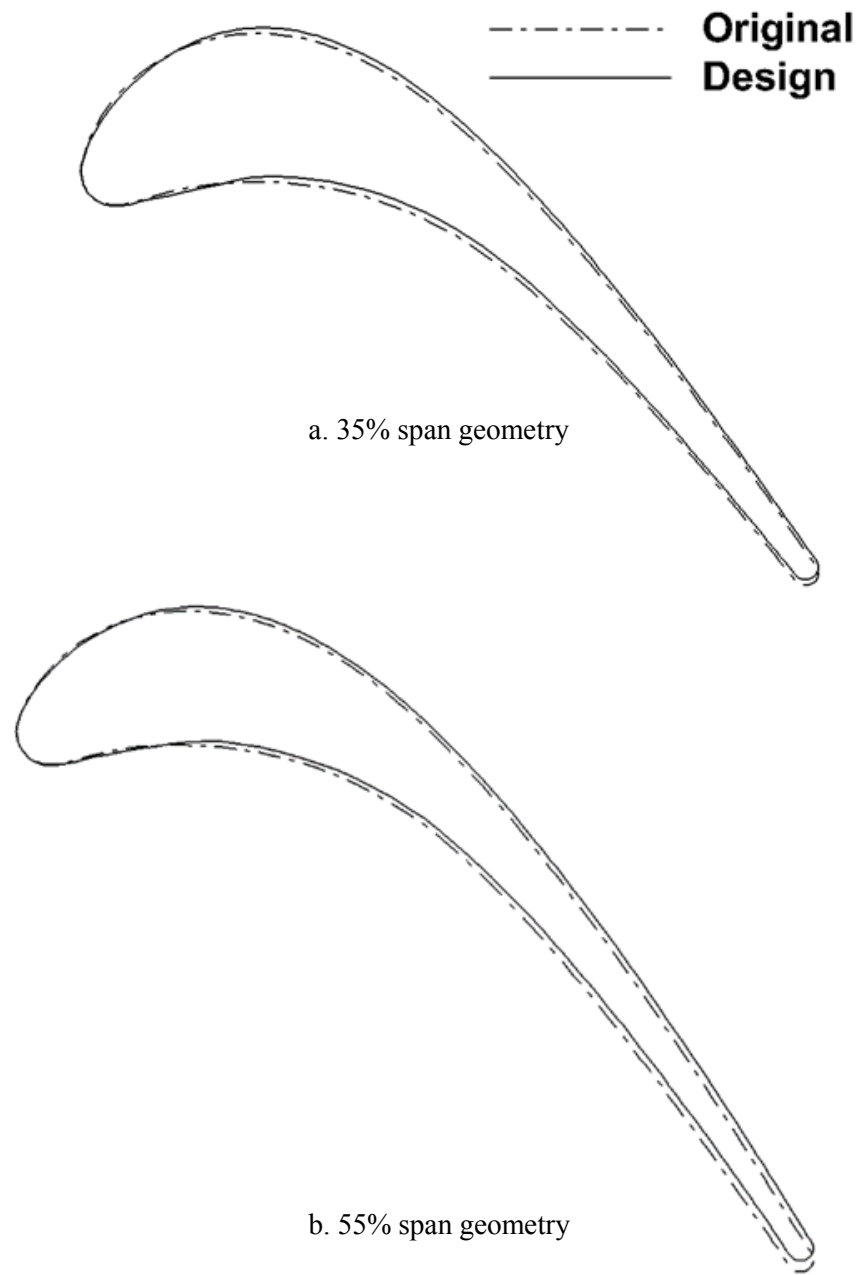
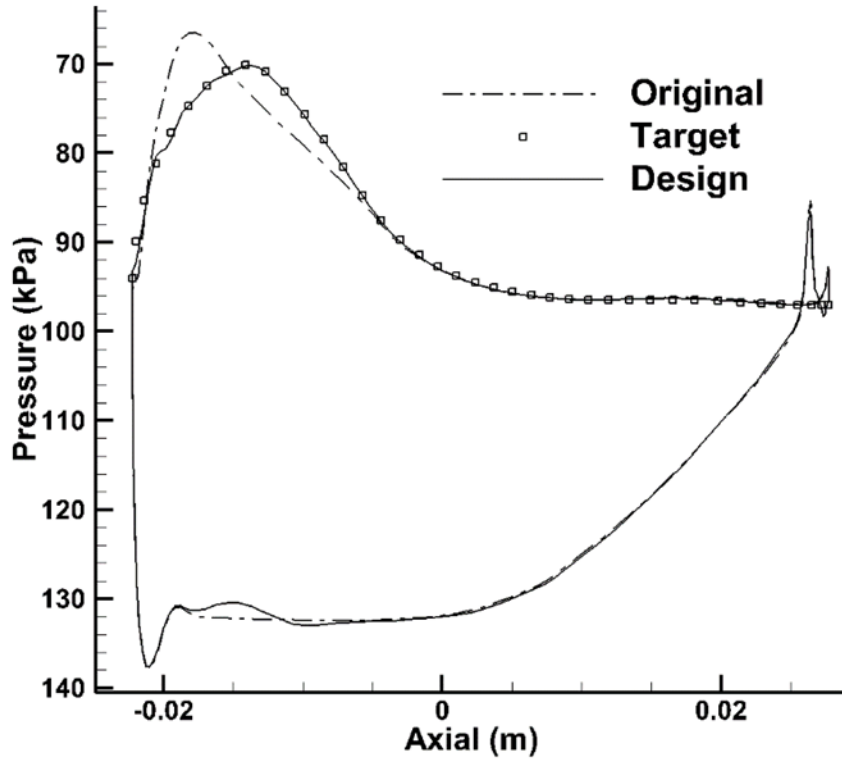
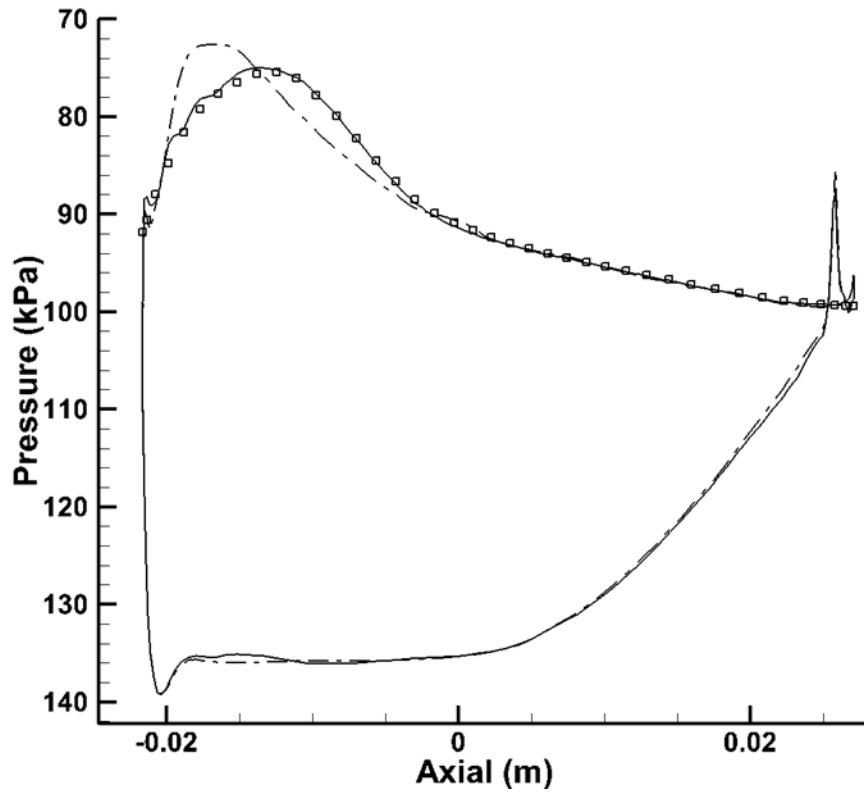


Figure 4.13. E/TU-3 Turbine Rotor: Original and design airfoil geometry

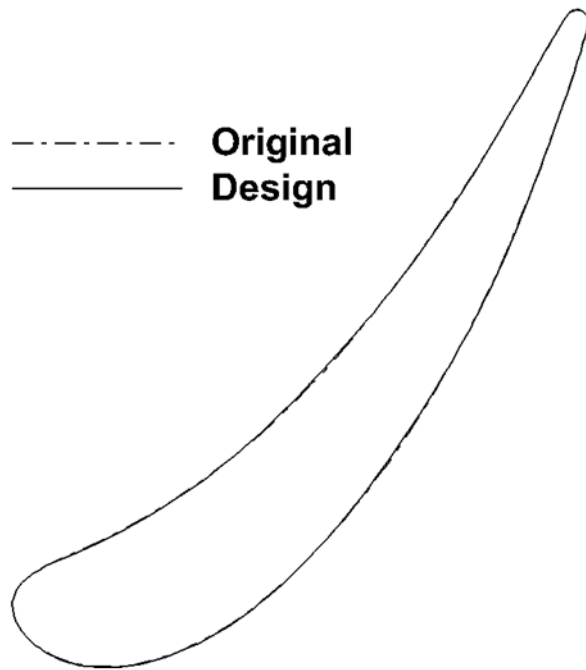


a. 35% span static pressure

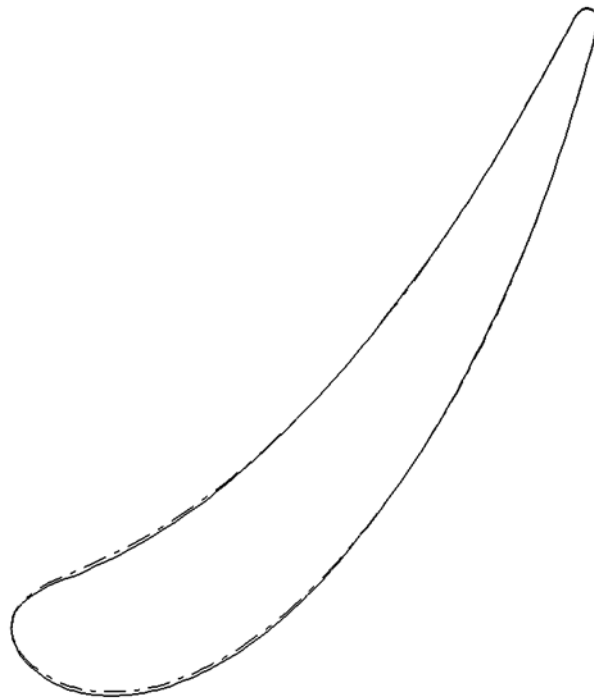


b. 55% span static pressure

Figure 4.14. E/TU-3 Turbine Rotor: Original, target and design static pressure

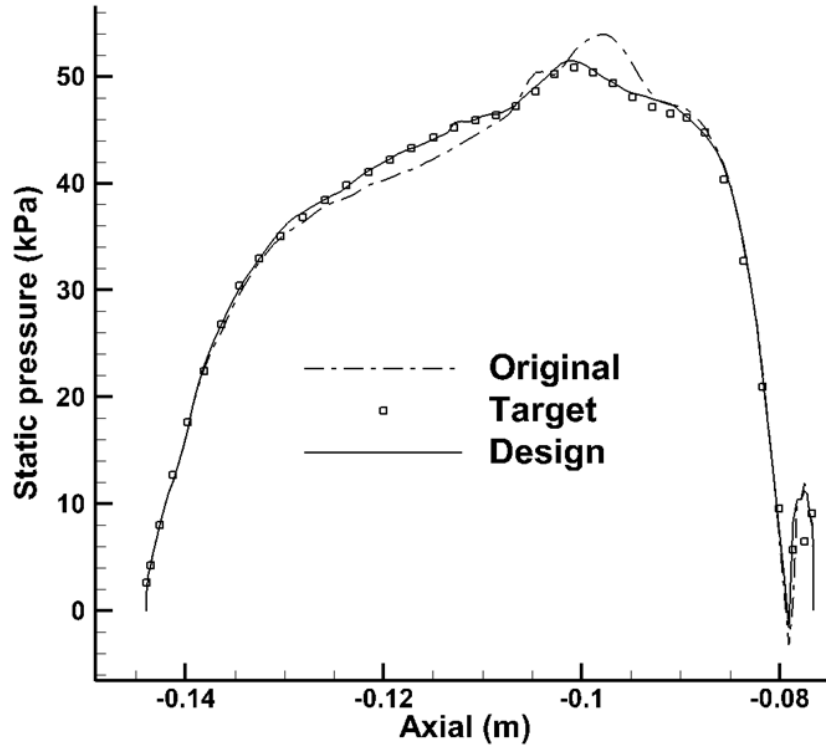


a. 45% span geometry

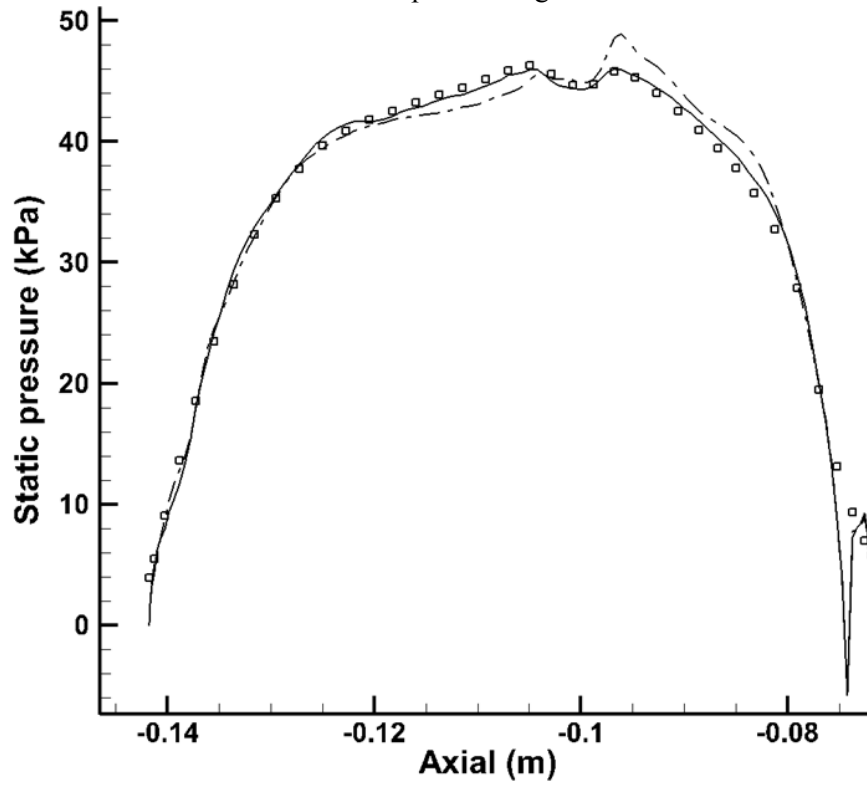


b. 80% span geometry

Figure 4.15. E/TU-3 Turbine Stator: Original and design airfoil geometry



a. 45% span loading



b. 80% span loading

Figure 4.16. E/TU-3 Turbine Stator: Original, target and design pressure loading

Chapter 5

CFD analysis and inverse design of axial compressor and turbine stages

The E/CO-3 compressor stage at two different operating conditions, namely max flow and design points, was first analyzed in ANSYS-CFX and the results were evaluated against the available experimental data [47]. At maximum flow conditions a mesh sensitivity study was carried out and the analysis was performed using three different turbulence models for each mesh. The inverse design methodology was then implemented to the redesign of the compressor stage at both operating conditions. The transonic compressor stage 67 and E/TU-3 turbine stage were then analyzed in ANSYS-CFX. After validating the analysis results, the inverse design method was used to redesign the stages so as to improve their aerodynamic performance. The details of the computational mesh for all the test cases investigated in this research are provided in Appendix B.

5.1. Analysis of the E/CO-3 Compressor Stage

The single stage subsonic compressor, called E/CO-3, is first analyzed in ANSYS-CFX at two points on the design speed line (of 9,262.5 rpm), namely Maximum Flow and Design Points. The geometric characteristic of the stage is shown in Table 5.1.

Mesh sensitivity study (two different meshes) using 3 different turbulence models (K-Omega, BSL and SST) was performed at maximum flow conditions where for the fine mesh there are 1.17m nodes on the rotor and 680k nodes on the stator blades. Each blade row consisted of 40 spanwise grids and the blade boundary layer is resolved with more than 20 mesh lines as shown in Figure

Table 5.1. E/CO-3 Stage geometric *characteristics* (Ref. [47])

	Rotor	Stator
Inlet blade angle	57.79°	36.64°
Exit blade angle	43.03°	-9.23°
Number of blades	41	73
Stagger angle	49°	14°
Space to chord ratio	0.9	0.7
Reynolds number	0.7×10^6	0.6×10^6

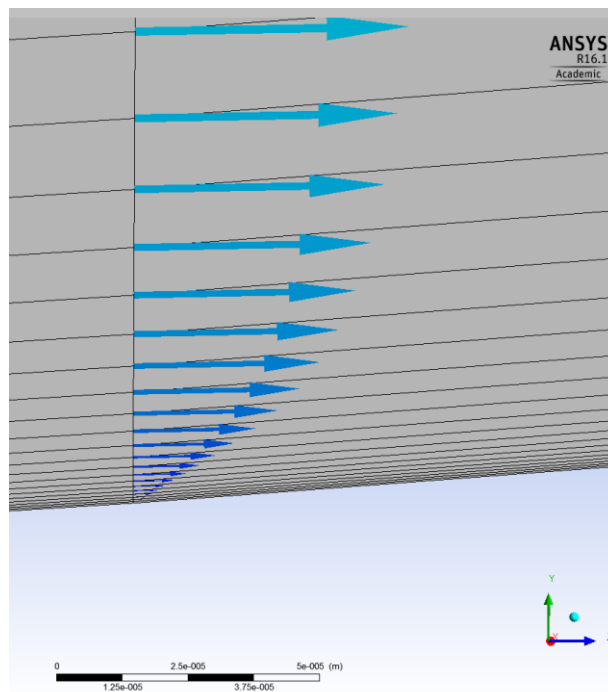


Figure 5.1. Velocity profile inside the boundary layer of the fine mesh

5.1. The results obtained for the BSL and K-omega turbulence models were almost identical and more accurate (when compared to the experimental data [47]) than the results obtained for the SST model. In addition, due to the extra equation in SST turbulence model, the analysis took more time

to converge.

For the coarse mesh there are 760k nodes on the rotor and 440k nodes on the stator blades; each blade row consisted of 30 spanwise grids and the boundary layer is resolved with more than 15 mesh lines as shown in Figure 5.2. Again the BSL and K-Omega turbulence models resulted in the same and more accurate solution than SST model. The chosen number of mesh lines in the boundary layer, for both meshes, guarantees the boundary layer resolution specifically when the

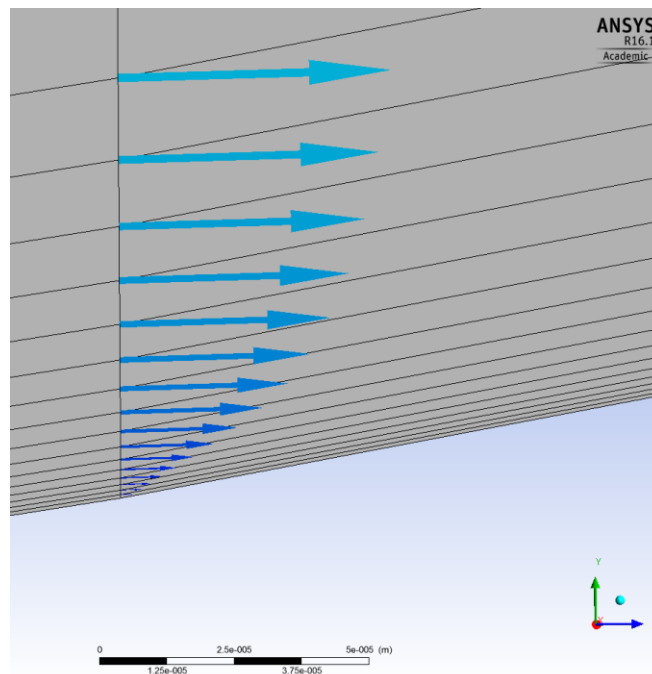


Figure 5.2. Velocity profile inside the boundary layer of the coarse mesh

SST turbulence model is used. The mass-averaged parameters obtained for both meshes were then compared against the experimental data which are provided in Table 5.2.

The values provided under the ‘Measured’ column (experimental data) are the averaged values at 10 different spanwise location. The static pressure, which is set as the exit boundary condition, is

Table 5.2. E/CO-3 compressor stage analysis results at Maximum Flow

	Measured [47]	Coarse mesh			Fine mesh		
		BSL	K-Omega	SST	BSL	K-Omega	SST
Turbulence model	-	BSL	K-Omega	SST	BSL	K-Omega	SST
Inlet tot. P (kPa)	95.7	95.57	95.57	95.57	95.48	95.48	95.48
Inlet tot. T(K)	288	288	288	288	288	288	288
Stage PR	1.196	1.193	1.193	1.191	1.194	1.195	1.192
Efficiency (%)	85.7	85.71	85.66	86.1	86.1	86.1	86.5
Stage exit Mach	0.419	0.419	0.419	0.417	0.419	0.42	0.417
TRR	0.0612	0.0605	0.0605	0.0596	0.0605	0.0606	0.0596
Mass flow (kg/s)	9.9	9.89	9.89	9.85	9.89	9.89	9.83
Exit flow angle (deg)	-1.5	-1.99	-2.08	-2.1	-1.95	-2.03	-2.1
Exit tot. T (K)	305.62	305.41	305.44	305.17	305.43	305.46	305.17
Exit tot. P (kPa)	115	114.03	114.05	113.85	114.04	114.08	113.85

tailored a bit (about 1 kPa) for the analysis so as to match the experimental mass flow rate and stage pressure ratio. Comparison of the coarse and fine mesh results for each turbulence model shows the agreement between the flow parameters except for a small discrepancy in the efficiency value which is because of a negligible change of 0.1% in the inlet total pressure which is caused by different number of spanwise airfoils and pressure averaging.

The E/CO-3 stage was then analyzed at design conditions. Based on the observations in mesh sensitivity study at maximum flow where the fine and coarse mesh results were comparable, the analysis at the design point is carried out using the coarse mesh and BSL turbulence model only

and the results obtained were compared with experimental data as listed in Table 5.3. Small discrepancies were observed for some of the flow parameters such as exit total pressure for which two reasons could be the cause. The first is the small change in the stage back pressure (2 kPa or about 2% of the experimental back pressure) to obtain the mass flow rate and stage pressure ratio as close as possible to the experimental data. The second reason is the geometry itself which may be slightly different from the real geometry. To construct the geometry used in this thesis, the raw data available in [47] has been used through which b-spline curves are fitted to obtain the airfoils at different spanwise sections. However, the discrepancy does not exceed 2.5% at worst.

Table 5.3. E/CO-3 compressor stage analysis results at Design Point

	Measured	Computed
Turbulence model	-	BSL
Inlet tot. P (kPa)	95.0	95.3
Inlet tot. T(K)	288	288
Stage PR	1.236	1.233
Efficiency (%)	88.3	89.6
Stage exit Mach	0.375	0.385
TRR	0.0707	0.0690
Mass flow (kg/s)	9.4	9.5
Exit flow angle (deg)	1.1	2.0
Exit tot. T (K)	308.35	307.849
Exit tot. P (kPa)	119.4	117.6

5.2. Redesign of the E/CO-3 compressor stage at Maximum Flow

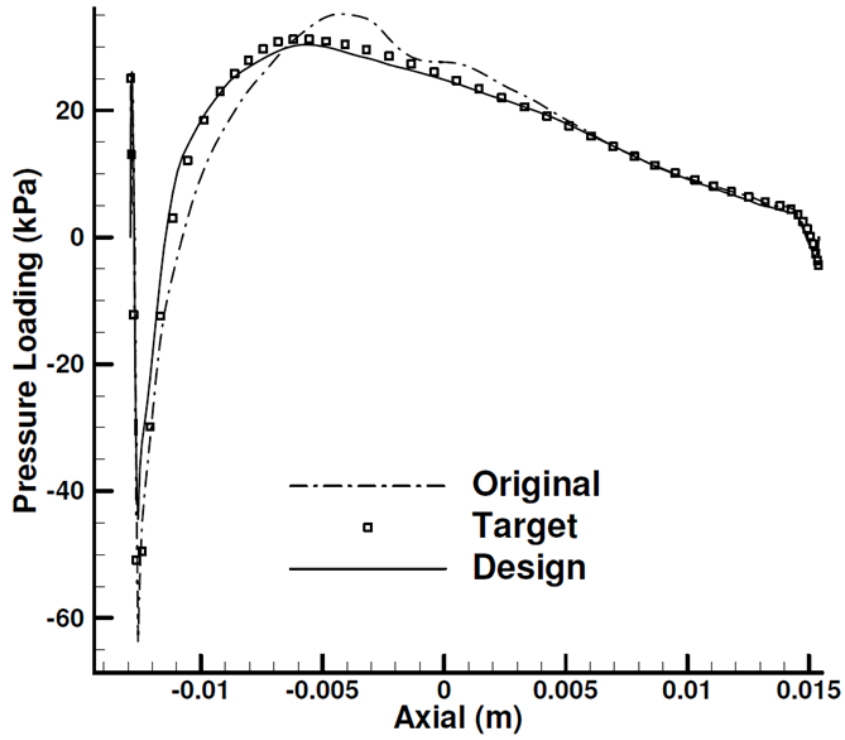
After validating the inverse design methodology and analyzing the original geometry, the inverse design method was applied to the redesign of the E/CO-3 compressor stage. The rotor was redesigned first at maximum flow conditions; while the stator blade shape was fixed. This is obtained by running ANSYS-CFX for the stage with one row running in inverse mode while the other is running in analysis mode.

The blade consisted of 30 spanwise airfoils, each with 294 nodes. Six spanwise grids located at the hub, 15%, 40%, 60%, 85% and 98% span were selected as the design airfoils. The rotor blade has tip clearance. Hence, the last 2% of the blade (in spanwise direction) is obtained by extrapolation. The rest of the airfoils are obtained by interpolation and Morphing method.

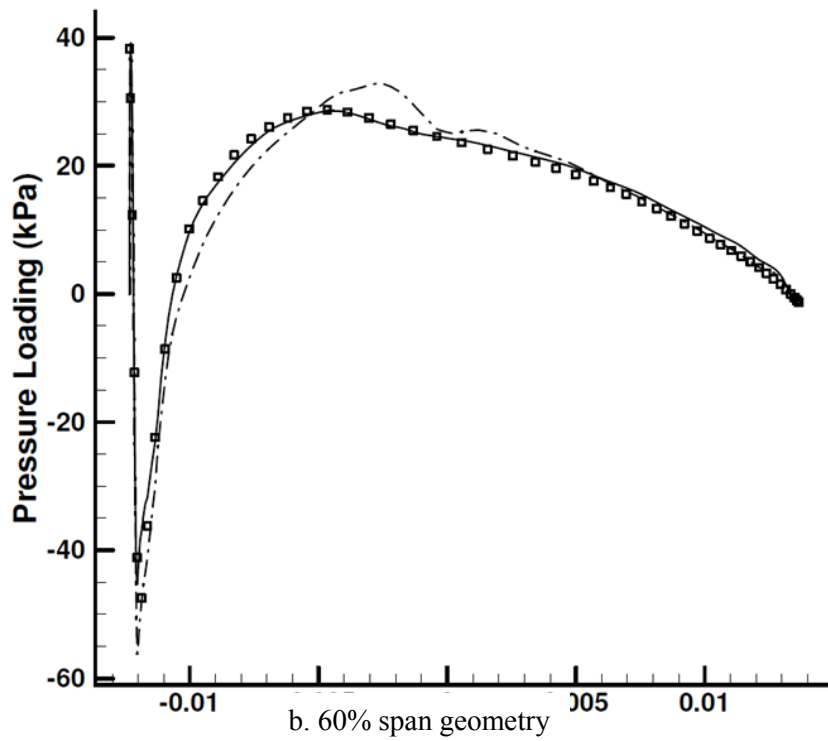
The design intent was to increase the total-to-total efficiency of the stage by specifying a target loading pressure distribution that would correspond to a lower negative incidence on the rotor as well as lower peak Mach number on the blade suction surface compared with the original blade so as to reduce the diffusion and the chance of flow separation. Care was taken to maintain the same overall loading.

The design took 70 steps to satisfy the prescribed target loading by about 80%. The design computational time is approximately equivalent to one flow simulation. Figures 5.3 and 5.4 show the original and design pressure loading and airfoil geometries at 15% and 60% span.

It can be seen from the figures that the peak loading, hence the peak Mach number over the suction surface, as well as the adverse pressure gradient are reduced which leads to the reduction of diffusion and consequently a reduction in stage pressure loss. Moreover the negative incidence at rotor inlet has also been reduced. These factors together increased the stage total-to-total efficiency from 85.7% to 86.5% (i.e., 0.8%). Table 5.4 compares flow parameters before and after the design.

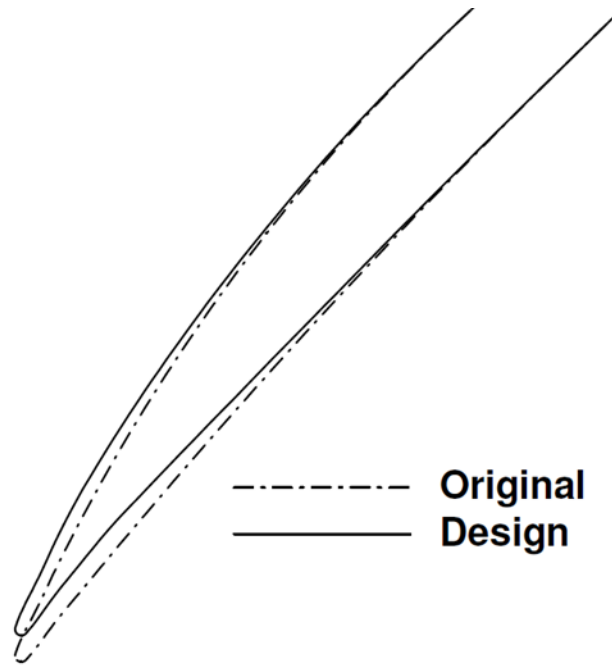


a. 15% span loading

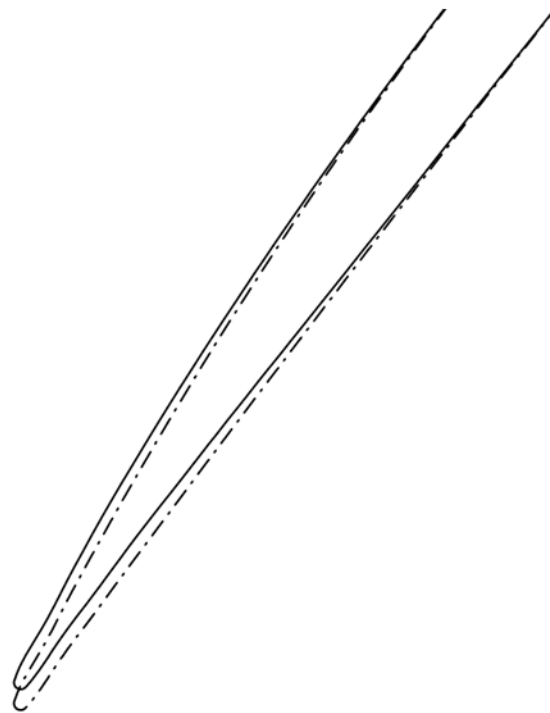


b. 60% span geometry

Figure 5.3. E/CO-3 Rotor redesign at maximum flow conditions: pressure loading



a. 15% span geometry



b. 60% span geometry

Figure 5.4. E/CO-3 Rotor redesign at maximum flow conditions: geometry

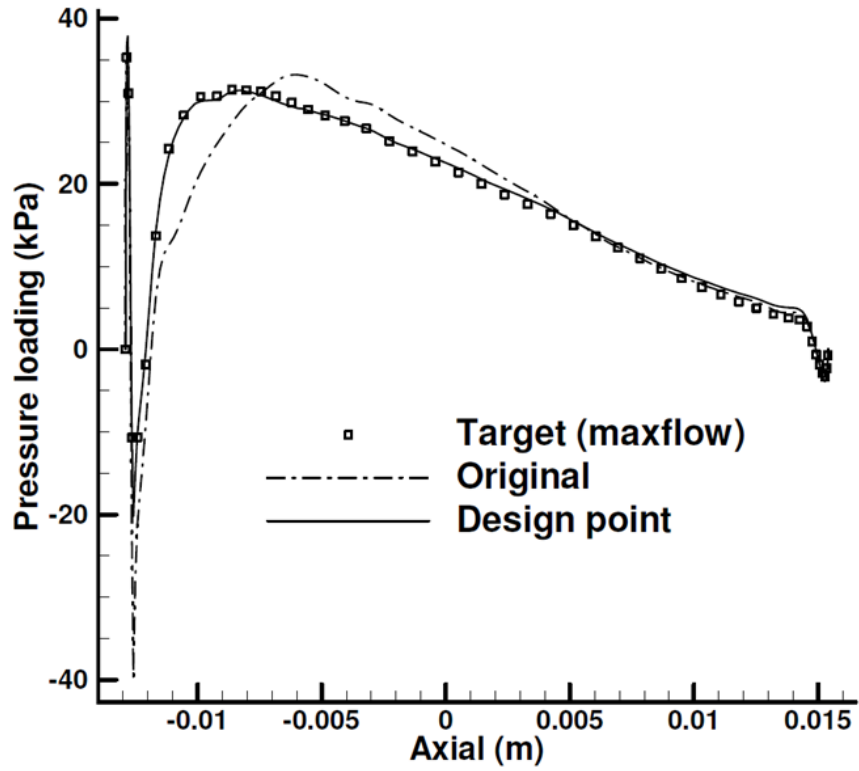
Table 5.4. Original and design flow parameters at maximum flow conditions

	Original	Design
Stage PR	1.193	1.196
Efficiency (%)	85.71	86.50
Stage exit Mach	0.419	0.424
TRR	0.0605	0.0608
Exit flow angle (deg)	-1.99	-1.95
Exit tot. T (K)	305.41	305.52
Exit tot. P (kPa)	114.03	114.33

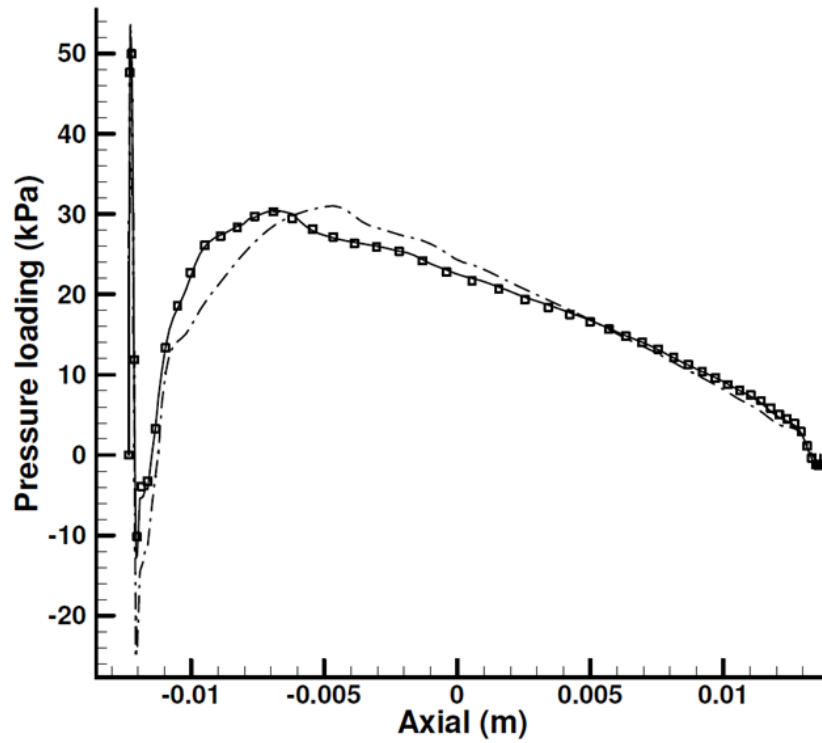
5.3. Redesign of the E/CO-3 compressor stage at Design Point

The method was then applied to the redesign of the rotor blade in design conditions. This redesign case was also another way to validate the 3D inverse design implementation. The redesigned stage at maximum flow was analyzed in design conditions. The rotor blade loading distribution thus obtained was set as the target loading for the original rotor blade to be designed at design conditions. All other design variables, number and location of design airfoils are the same as those at maximum flow design case. It was expected to improve the stage efficiency because of the slightly lower peak loading for some airfoils, reduction of pressure gradient by shifting the peak loading a bit upstream plus the reduction of the negative incidence. Another expectation was to retrieve the target blade i.e., the blade designed at maximum flow which was in fact fulfilled. After 95 design steps, it was observed that both target blade profile and pressure loading distributions for all the design airfoils were satisfied by 90%.

Figures 5.5 and 5.6 show the original and designed loading distribution and airfoils geometry located at 15% and 60% span.

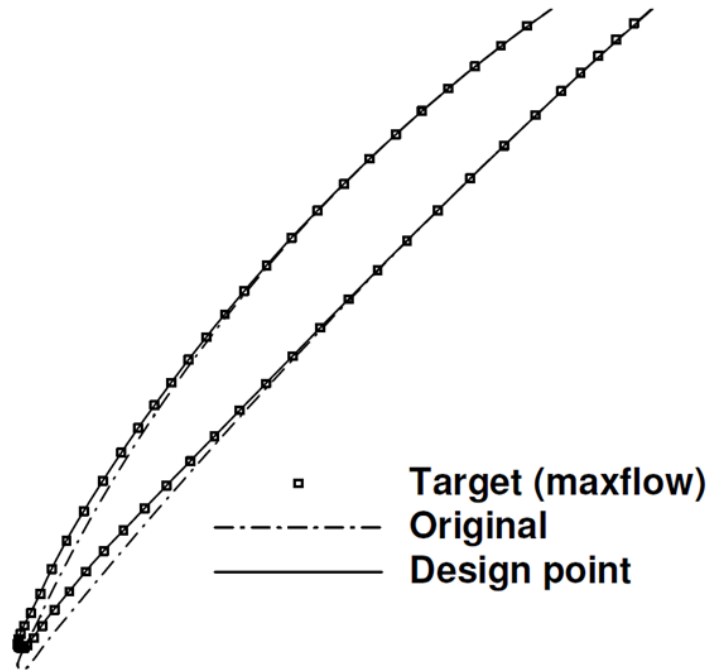


a. 15% span loading

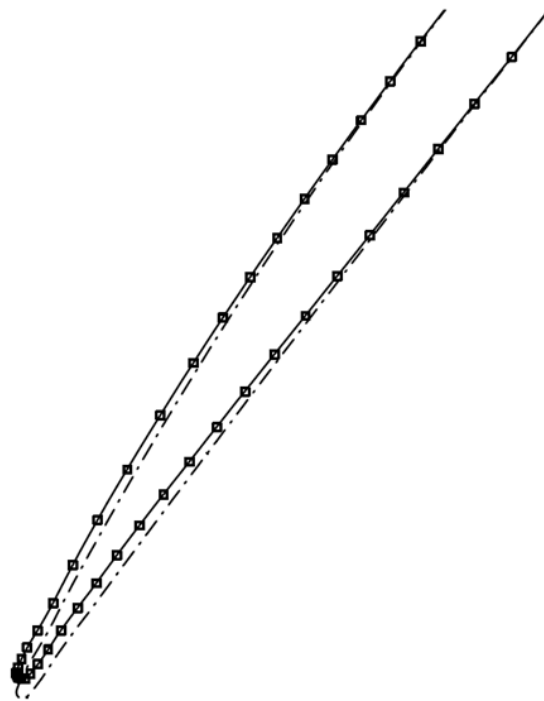


b. 60% span loading

Figure 5.5. E/CO-3 Rotor redesign at Design Point: pressure loading at 15% and 60% span



a. 15% span geometry



b. 60% span geometry

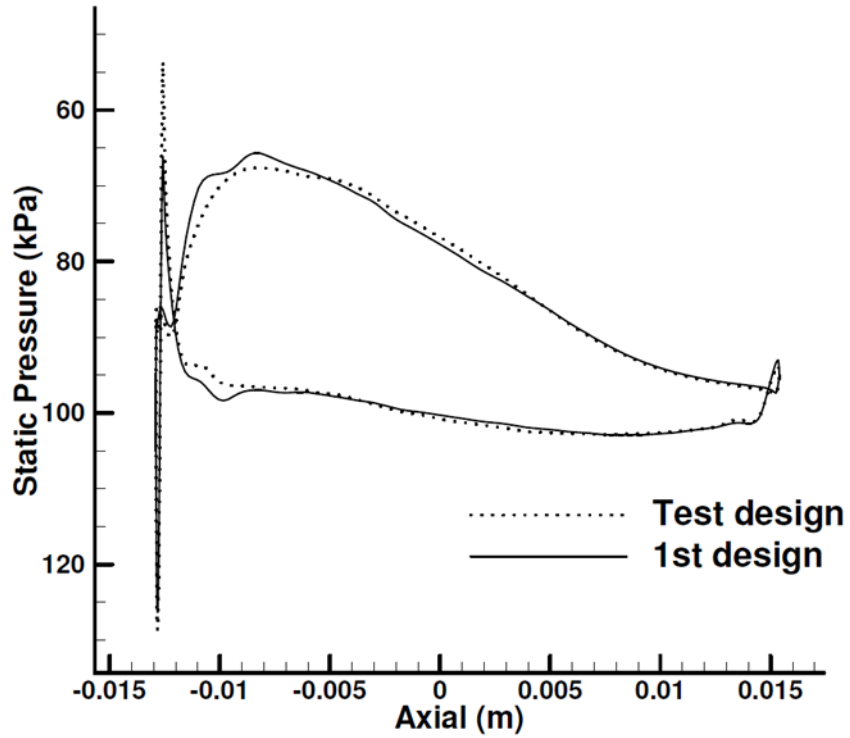
Figure 5.6. E/CO-3 Rotor redesign at Design Point: geometry at 15% and 60% span

Before assessing the performance of the designed stage, it would be worthwhile to comment on the convergence level. The reason why the problem converges by 80% for maximum flow and 90% for the design point may be linked the fact that at the maximum flow the target loading is the pure input of the designer and it may not correspond to a real blade shape while at the design point the performance of a real blade shape is set as the target hence the target is more likely to be reached. However, regardless of the above mentioned difference, one could clearly see from the figures that even convergence by 80% is safe enough to simply say that the problem is converged since all the main features of the target are accurately satisfied and the remaining small areas that are not fully matched have almost no effect on the performance and could be safely ignored.

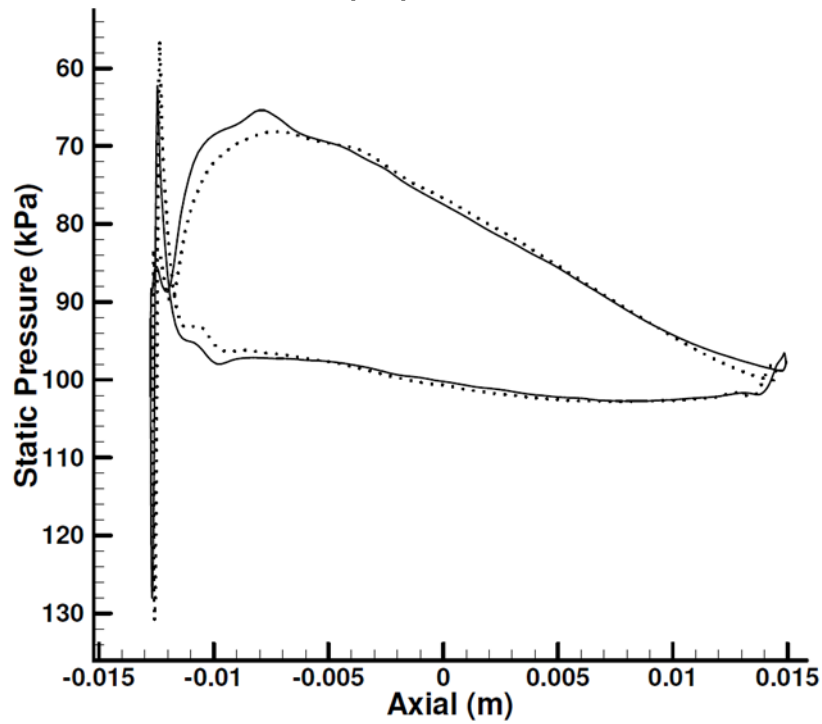
The assessment of the designed stage performance revealed 0.25% of improvement in the total-to-total efficiency at the design point.

By again looking at the Figure 5.5, it can be seen that there is still room for target modification by further repositioning and/or reduction of the peak loading and also reduction of the incidence. However, which factor dominates and plays the main role in the performance improvement? To find the answer, a test design was performed in which the target loading has a lower peak (suction surface has a lower peak Mach number) compared to the first design. Figure 5.7 shows the resultant pressure distribution on 15% and 40% span for both test and design cases.

The dotted line represents the pressure distribution corresponding to the test design which has a lower peak and larger incidence compared to the solid line representing the pressure for the first design case. The point here is that the efficiency improvement resulted from the test design is about 0.1% which is even less than the original design where the peak Mach number on SS is larger. Although the result suggests the peak Mach number value has smaller share on the efficiency improvement compared to the incidence angle, still it has a positive effect.



a. 15% span pressure distribution



b. 40% span pressure distribution

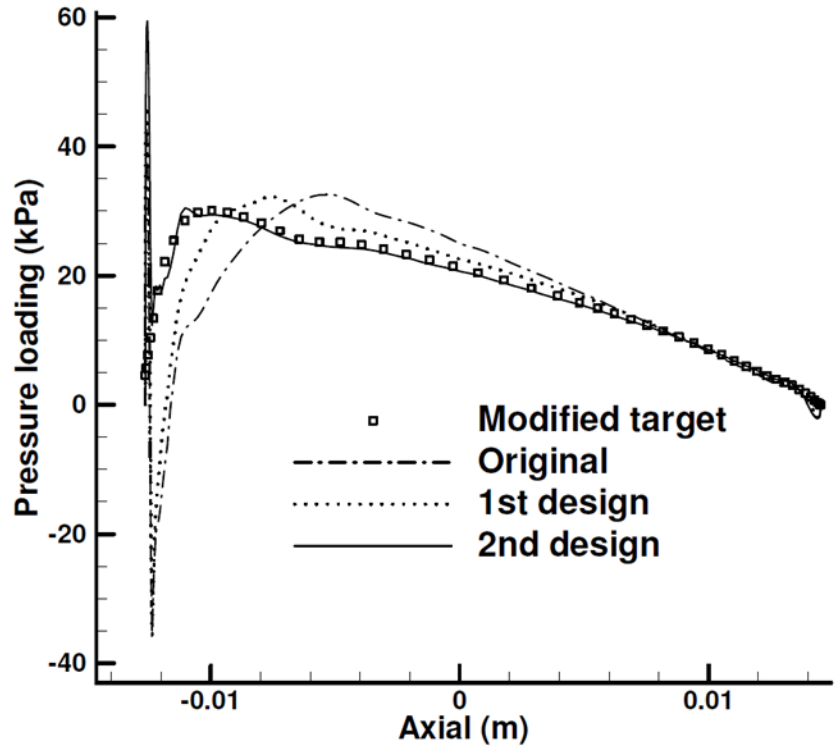
Figure 5.7. E/CO-3 Rotor redesign at Design Point: 1st and test designed pressure distributions

Hence, another design was performed at the design conditions where it was tried to modify all the above mentioned factors. The peak loading is shifted further upstream and the target loading corresponds to a lower incidence angle, peak value as well as the lower pressure gradient compared to the original design case.

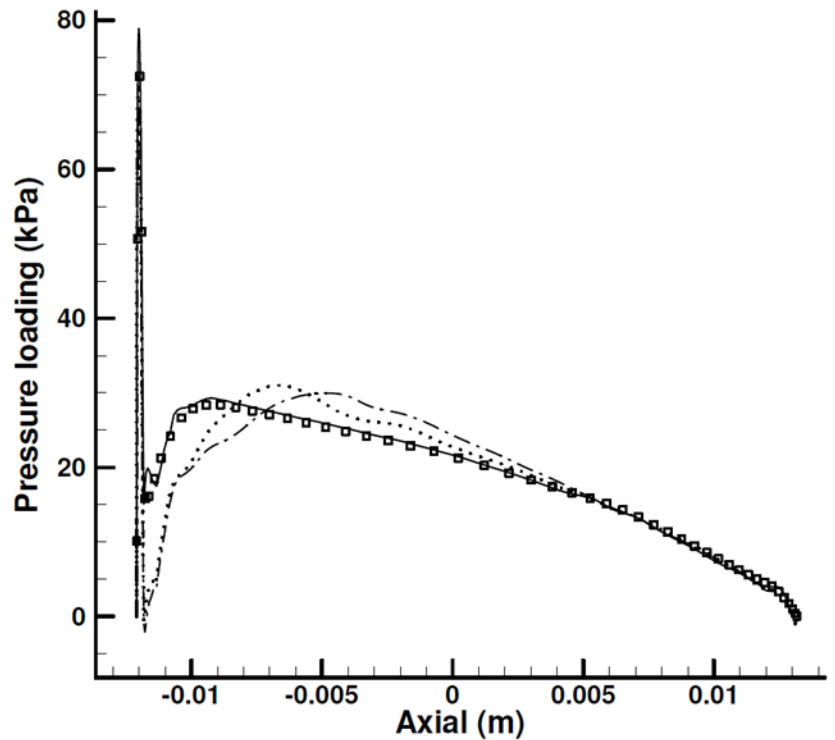
The design started from the first design case and performed for 130 steps until the target was satisfied by more than 80%. Table 5.5 summarizes the flow parameters for both design cases and compares them with the original stage. Figures 5.8, 5.9 and 5.10 respectively compare the loading, geometry and the static pressure of the 1st and 2nd design cases at 40% and 85% span. It could be seen from Figure 5.8 that the peak loading is pushed further upstream and the negative incidence is reduced until complete elimination as the minimum loading near the LE does not reach a negative value. Figure 5.10 also confirms the previous statement where for the 2nd design case (solid line) the pressure of suction and pressure surfaces do not cross each other at the LE. The pressure gradient as well as the peak Mach number on the suction surface are also further reduced and all these factors together led to an additional improvement of 0.2% in the total-to-total efficiency or about half a percent in total (from 89.6% to 90.05%) compared to the original stage and at the design conditions.

Table 5.5. Original and design flow parameters at Design Point

	Original	1st Design	2nd Design
Stage PR	1.233	1.236	1.236
Efficiency (%)	89.6	89.86	90.05
Stage exit Mach	0.385	0.390	0.390
TRR	0.0690	0.0695	0.0693
Exit flow angle (deg)	2.0	2.0	2.0
Exit tot. T (K)	307.849	308.024	307.97
Exit tot. P (kPa)	117.6	117.89	117.88

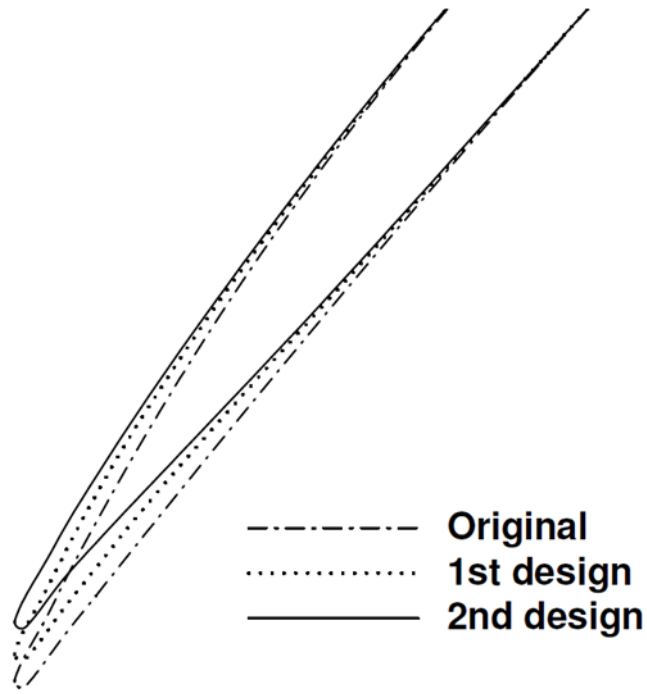


a. 40% span loading

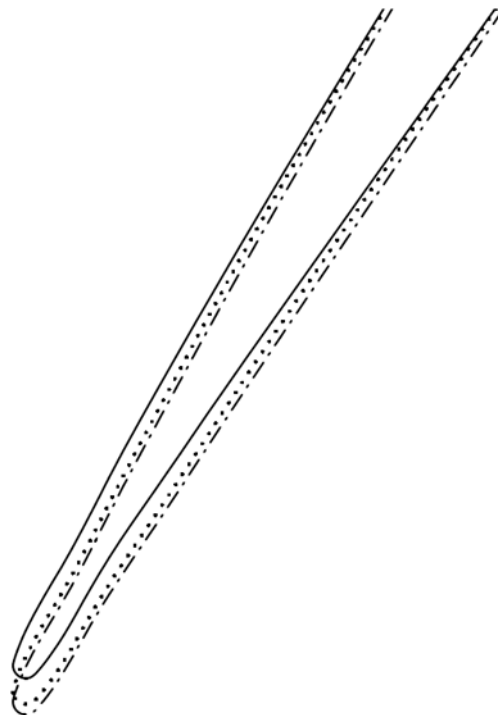


b. 85% span loading

Figure 5.8. E/CO-3 Rotor redesign at Design Point: Original and designed loading distribution

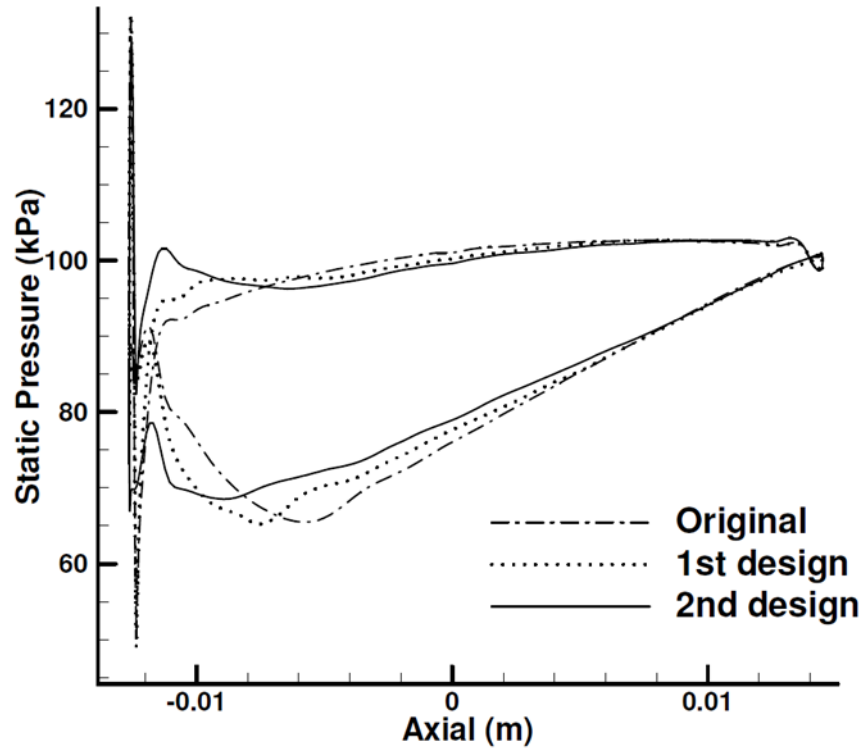


a. 40% span geometry

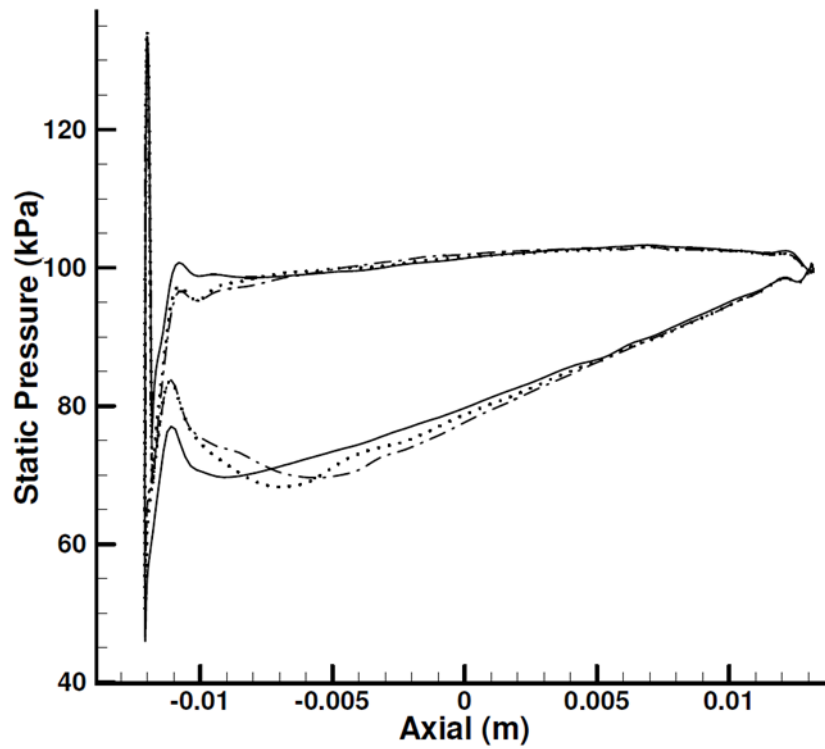


b. 85% span geometry

Figure 5.9. E/CO-3 Rotor redesign at Design Point: Original and designed airfoils



a. 40% span pressure



b. 85% span pressure

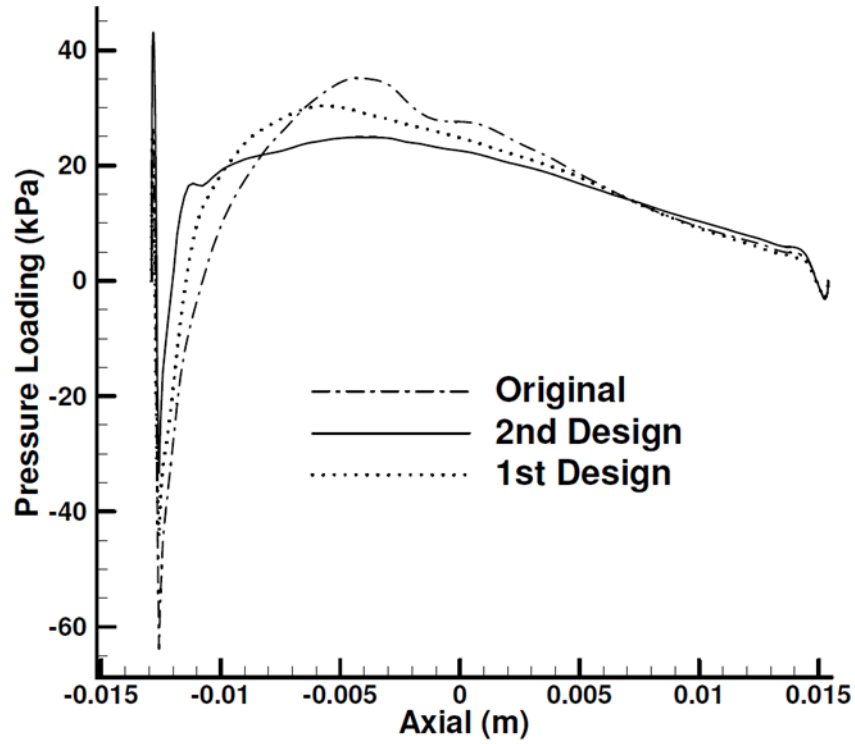
Figure 5.10. E/CO-3 Rotor redesign at Design Point: Original and designed static pressure

Now the 2nd designed stage is analyzed at maximum flow conditions and the results were compared with the 1st design at maximum flow conditions, with an expected improved performance. In fact, the achievement was remarkable. Table 5.6 gives the flow parameters for both design cases and compares them with the original stage. Figures 5.11 and 5.12 show the original and design loading and pressure distributions. It can be seen that both negative incidence and peak Mach number as well as the adverse pressure gradient on the suction surface are significantly reduced resulting in a considerable improvement of 1.9% in total-to-total efficiency (from 85.7% to 87.6%) of the stage at maximum flow conditions.

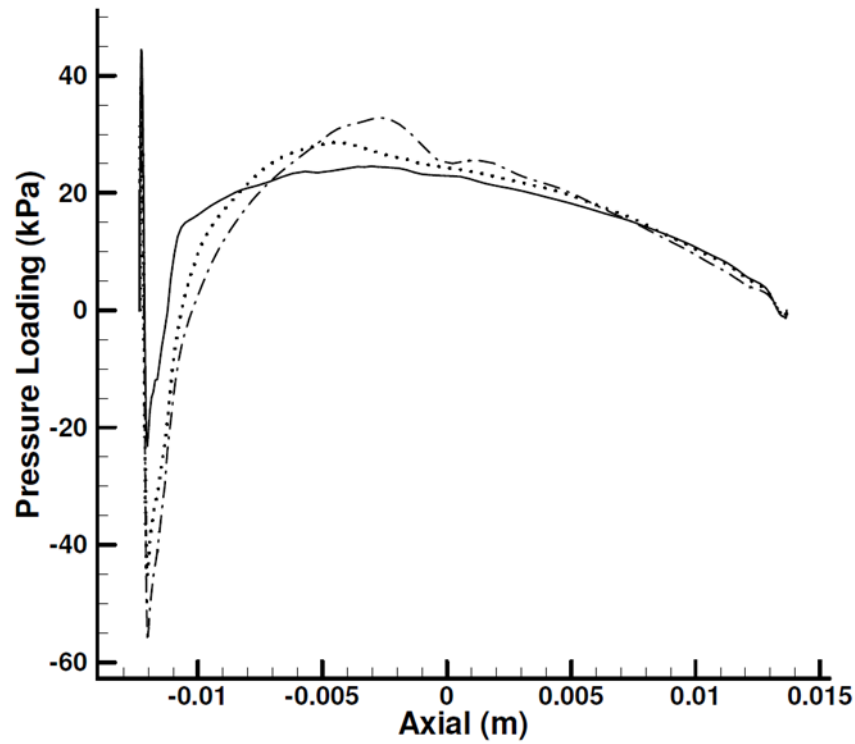
The efficiency improvement and reduction of the adverse pressure gradient in the spanwise direction at mid-chord are shown in Figures 5.13 and 5.14 respectively. Figure 5.15 compares the adverse pressure gradient in the streamwise direction at mid-span for the original and both design cases at maximum flow conditions.

Table 5.6. Original and design flow parameters at Maximum Flow

	Original	1st Design	2nd Design
Stage PR	1.193	1.196	1.199
Efficiency (%)	85.71	86.50	87.6
Stage exit Mach	0.419	0.424	0.427
TRR	0.0605	0.0608	0.0607
Exit flow angle (deg)	-1.99	-1.95	-1.92
Exit tot. T (K)	305.41	305.52	305.51
Exit tot. P (kPa)	114.03	114.33	114.56

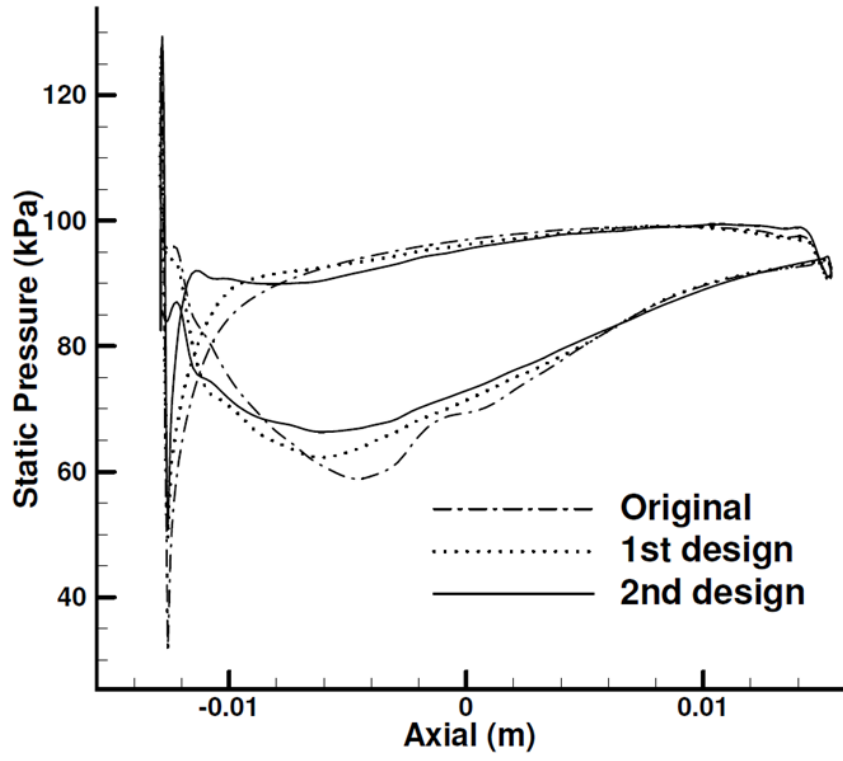


a. 15% span loading

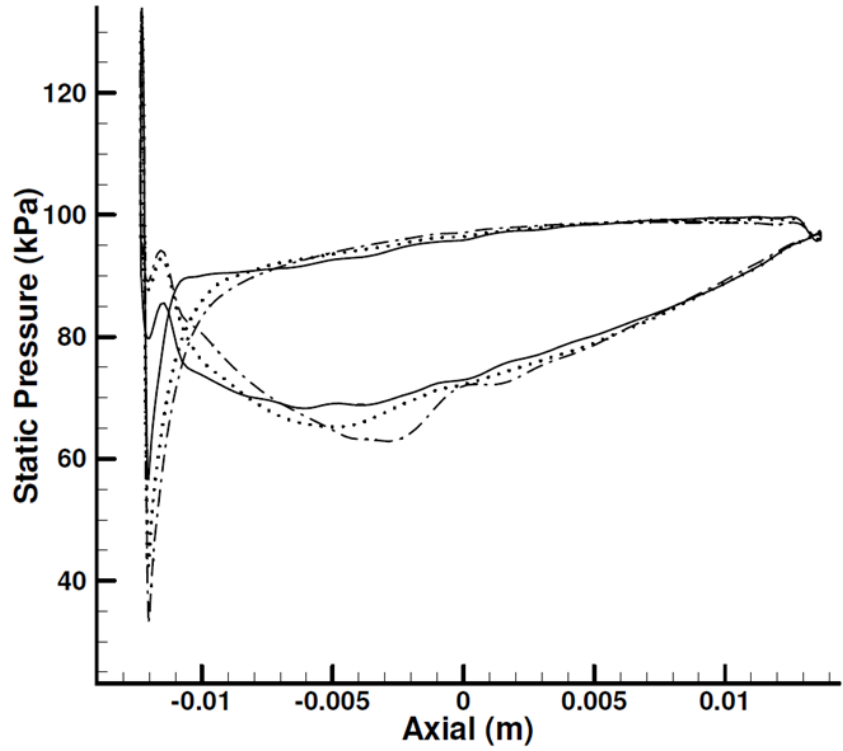


b. 60% span loading

Figure 5.11. E/CO-3 Rotor redesign at Maximum Flow: Original and designed loading distribution



a. 15% span static pressure



b. 60% span static pressure

Figure 5.12. E/CO-3 Rotor redesign at Maximum Flow: Original and designed static pressure

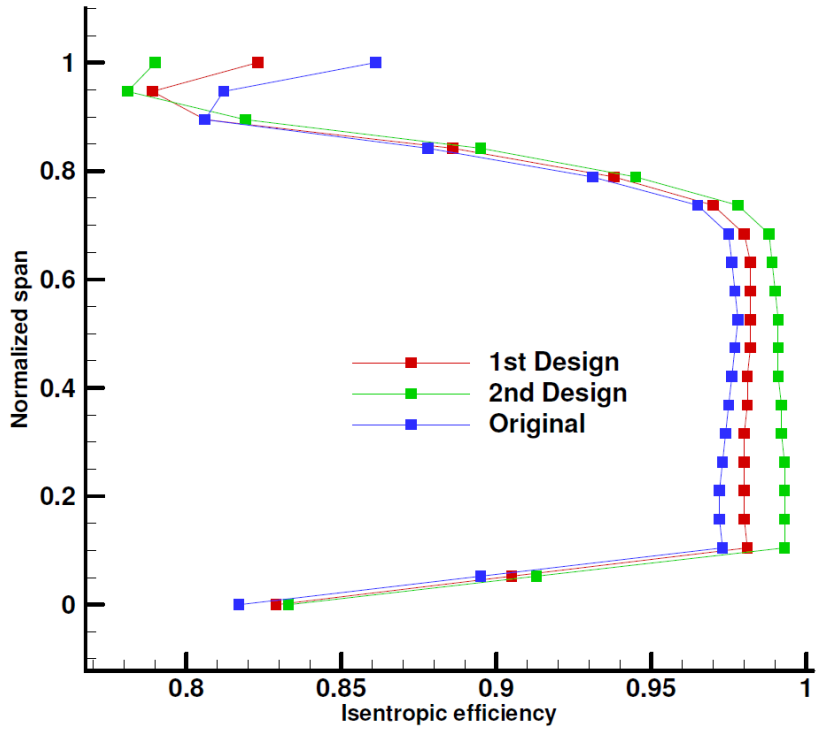


Figure 5.13. Original and designed efficiency in spanwise direction (mid-chord)

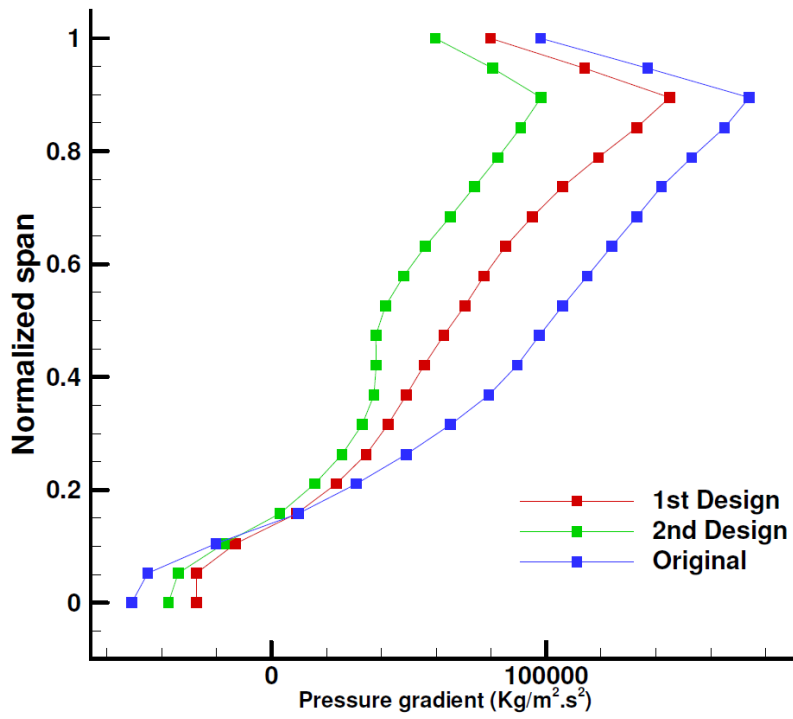


Figure 5.14. Original and designed pressure gradient in spanwise direction (mid-chord)

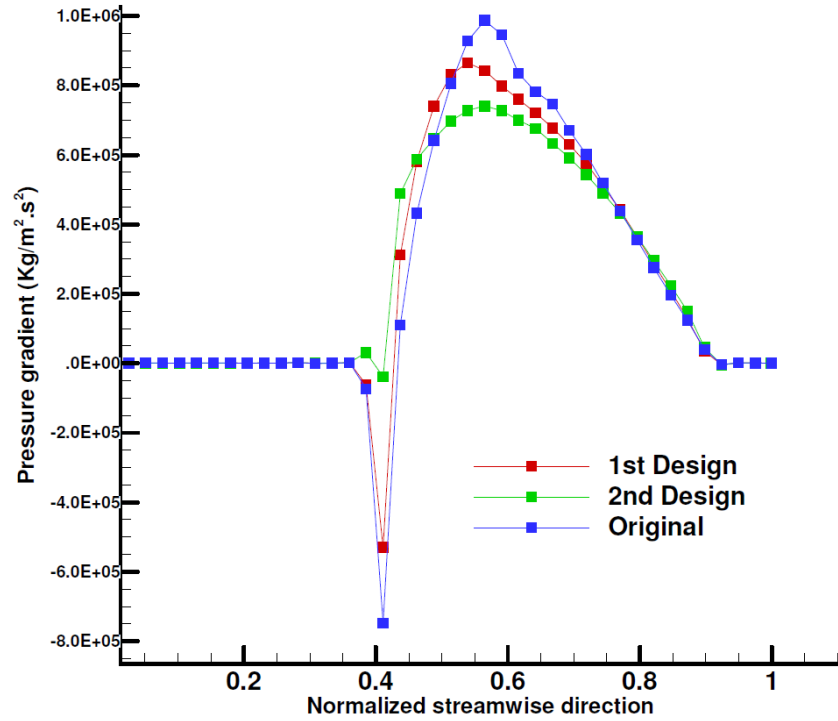


Figure 5.15. Original and designed pressure gradient in streamwise direction (mid-span)

The figures provided in this chapter so far belonged to the design airfoils. As mentioned previously, the intermediate airfoils are obtained by interpolation and Morphing method. Figure 5.16 shows the original airfoils and the designed and intermediate airfoils after the design process. In Figure 5.16, the solid and dotted black lines represent the design and intermediate airfoils before the design, respectively. The red and blue lines show the final obtained design and intermediate airfoils, respectively.

5.4. Analysis of the transonic compressor stage 67

The first stage of a two-stage transonic axial flow fan (Stage 67) is analyzed near the design point (rotor speed = 16,043 rpm). The numerical results thus obtained were compared with the available

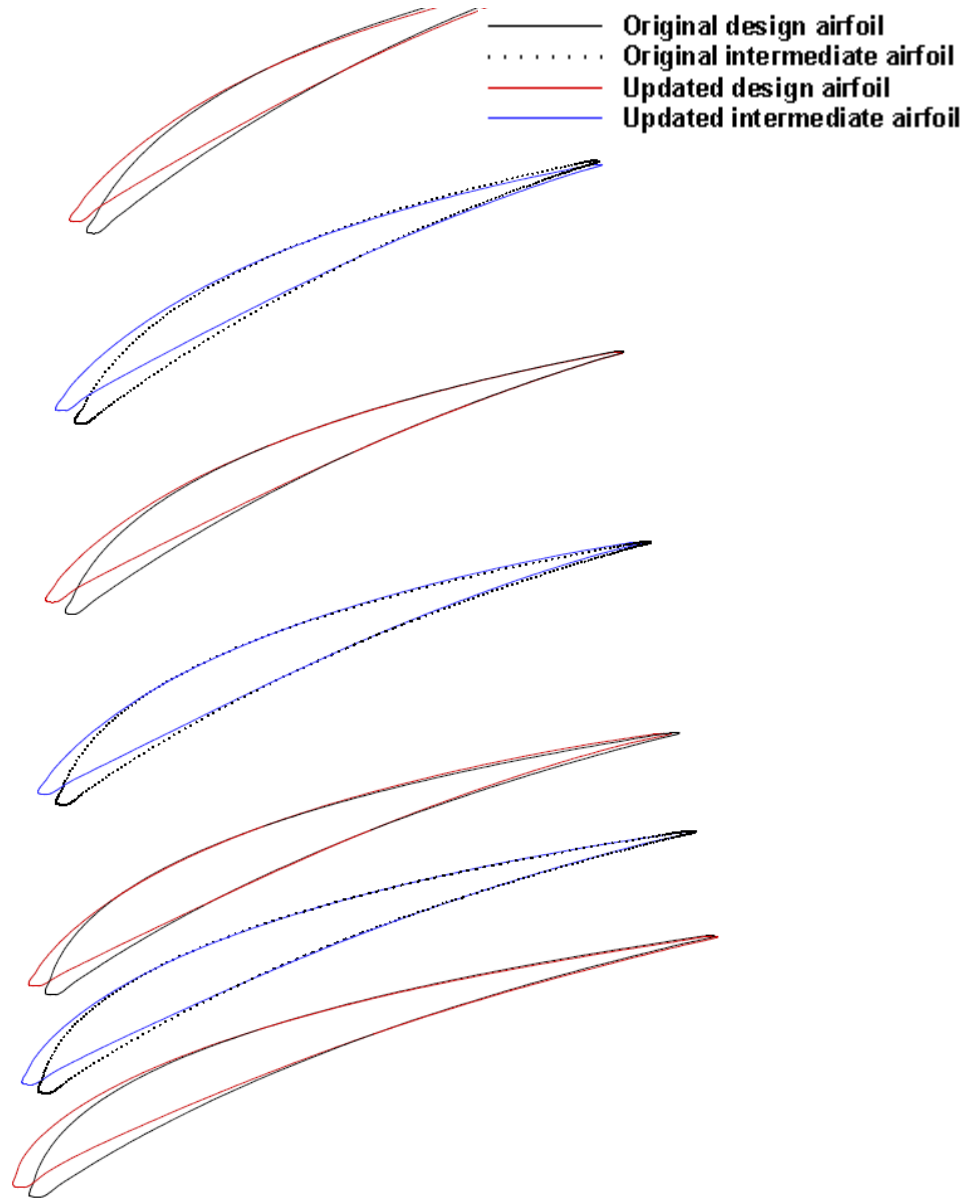


Figure 5.16. E/CO-3 Rotor: Design and intermediate airfoils before and after the design

experimental data [47]. A summary of the stage geometric parameters is provided in Table 5.7 and the analysis results are given in Table 5.8. It can be seen from Table 5.8 that the computed and measured data match reasonably well. The mesh generation package available in CFX specifically for turbomachinery blading, namely ‘TurboGrid’, is used for meshing Stage 67. An O-Grid mesh is constructed around the blade to resolve the boundary layer; the rest of the domain is filled with

structured mesh by using the so-called "Automatic ATM Optimized topology" setting available in TurboGrid. The rotor and stator domains contained 650K and 340K nodes, respectively (Figure 5.17). The BSL turbulence model was used for the analysis.

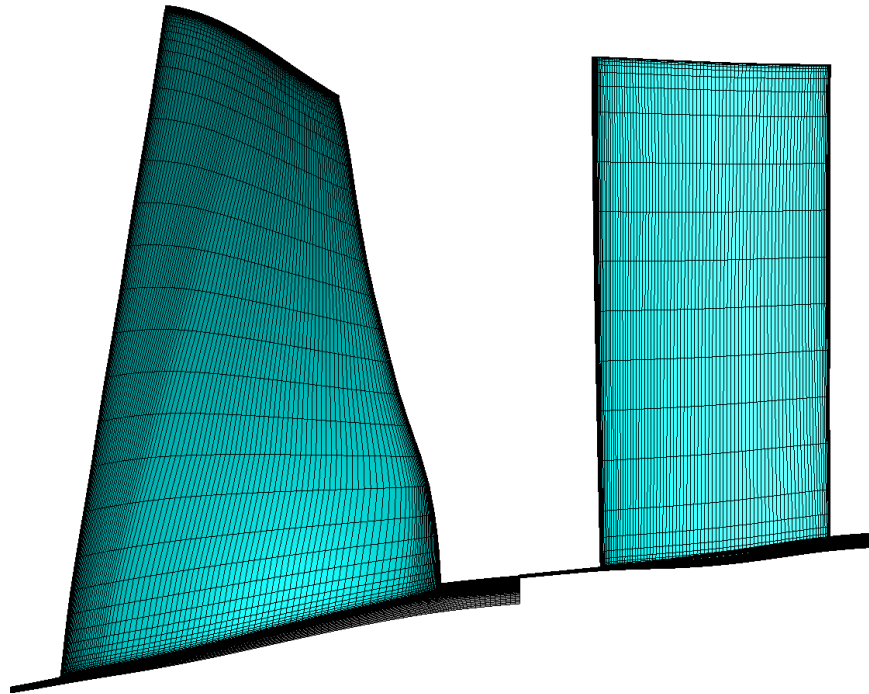


Figure 5.17. stage 67 meshed by TurboGrid

Table 5.7. Stage 67 geometric parameters

	Rotor	Stator
Number of blades	22	34
Running tip clearance (mm)	1	-
Tip chord (cm)	9.522	5.768
Hub chord (cm)	9.264	5.728
Tip solidity	1.290	1.271
Hub solidity	3.144	2.485
Maximum thickness-to-chord at tip	0.029	0.060
Maximum thickness-to-chord at hub	0.085	0.080

Table 5.8. Stage 67 analysis results at design point

	Measured	ANSYS-CFX
Stage PR	1.59	1.61
Mass flow (kg/sec)	33.25	33.42
Inlet flow angle	0.0°	0.0°
Efficiency (%)	83.8	84.91
<i>Rotor</i>		
Inlet P₀ (kPa)	101.35	101.49
Inlet T₀ (K)	288.16	288.16
Exit P₀ (kPa)	165.48	167.47
Exit T₀ (K)	337.3	337.9
<i>Stator</i>		
Exit P₀ (psi)	160.3	164.02
Exit T₀ (K)	337.2	338
Exit flow angle	-0.0°	0.16°
Exit Mach number	0483	0.477

5.5. Redesign of the transonic axial flow compressor

The inverse design method was applied to the redesign of Stage 67. The stator was redesigned at design point while the rotor blade shape was fixed. The design intent was to increase the total-to-total efficiency, by specifying a target blade pressure loading distribution that would correspond to a lower positive incidence on the stator compared with the original one. Care was taken to

maintain the same overall loading. Due to a large incidence angle, there was an area of the reversed flow in the region near the stator tip LE on the suction surface (see Figure 5.18) which was eventually eliminated by rotating the LE of the tip section to satisfy the target loading hence reducing the losses associated with the reversed flow [33].

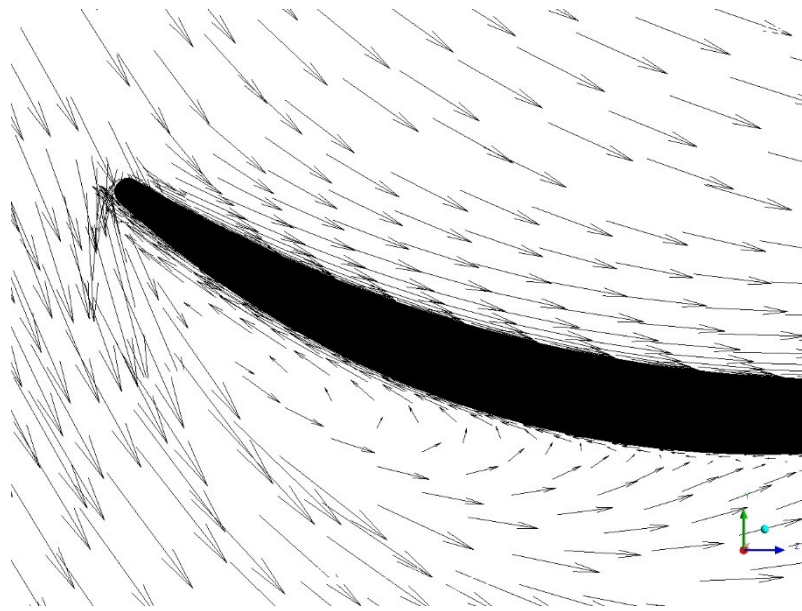


Figure 5.18. Velocity vectors near the tip section of original Stator 67

The Dp Design was chosen where the design variables are the blade pressure loading and normal thickness distributions, and the stacking line which was set at 50% of the axial chord. The stator blade consists of 31 airfoils in the spanwise direction, each with 206 nodes. Six spanwise airfoils located at the stator hub, 20%, 40%, 60%, 80% and the stator tip section were chosen as the design airfoils for which a target pressure loading was generated. The remaining airfoils were then obtained by fitting a surface through the chosen six spanwise locations from hub to tip (using the Fitting approach). This approach ensures that the designed 3D blade is smooth in both streamwise

and spanwise directions. The first and last 2% of the stator blade were run in analysis mode to ensure that the blade shape is closed and is smooth. The inverse design converged in 110 design steps in total. As explained, in order to remove accumulated flow unsteadiness, resulted from the blade movement, the design process was interrupted a few times and the designed blade (at that stage of the design) was run in analysis mode. The design process was then continued from the latest obtained designed blade. The convergence is measured by the L2-norm of DP which was reduced by about an order of magnitude (i.e., 90%) for most of the six spanwise design airfoils. The design results are listed in Table 5.9. The original, design and target pressure loading distributions for these airfoils are shown in Figure 5.20, the resulting airfoil shapes are shown in Figure 5.21. It can be seen that the target loading was closely satisfied at 40% and 60% span while at the hub and tip, the main features of the target loading were fulfilled, namely reducing the positive incidence. The rotation of the designed airfoils so as to reduce incidence can be clearly seen in the figures [33].

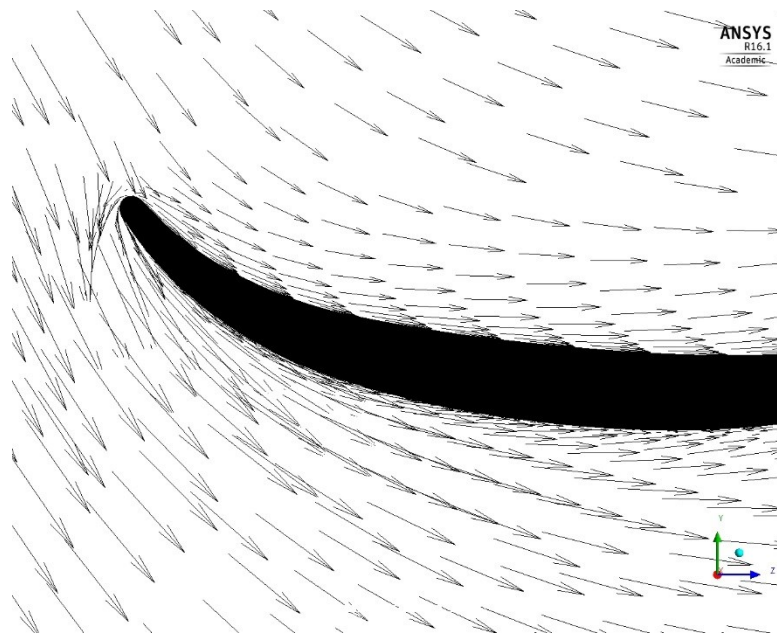


Figure 5.19. Velocity vectors near the tip section of designed Stator 67

The most interesting behavior was observed near the stator blade tip LE on the suction side where the very large incidence angle resulted in a large flow recirculation area showing on the original geometry (Figure 5.18). As explained, the target loading for this airfoil was prescribed so as to reduce the incidence. The blade rotated during the design process and as the design steps progressed, the recirculation area kept decreasing until its complete elimination near the LE of the tip section (Figure 5.19). However, it can be seen from Figure 5.20d that the peak design loading is larger than the original loading. The lower original peak loading is believed to be due to the reversed flow which is in the direction opposite to the approaching flow, hence the flow hitting the LE on suction surface is decelerated and the pressure on the suction surface increases. By eliminating the reversed flow, the resistance to the incoming flow is eliminated as well so the flow on the suction surface is accelerated as the reversed flow area is weakened gradually (pressure on the suction surface decreases near the LE) and the loading in the tip LE increases rapidly [33].

The reduction of the positive incidence all the way from hub to tip and the elimination of the reversed flow in the tip region, altogether led to the increase in total-to-total efficiency from 84.9% to 85.9% (i.e., 1%) as well as a reduction of about 0.5% in the stator total pressure loss.

Table 5.9. Stator 67 DP Design parameters

	Original	Design
Stator PR	0.9817	0.9863
Efficiency (%)	84.9	85.9
Mass flow (kg/sec)	33.42	33.64
Exit T₀ (K)	337.3	338.0
Exit flow angle (deg)	0.16	2.27

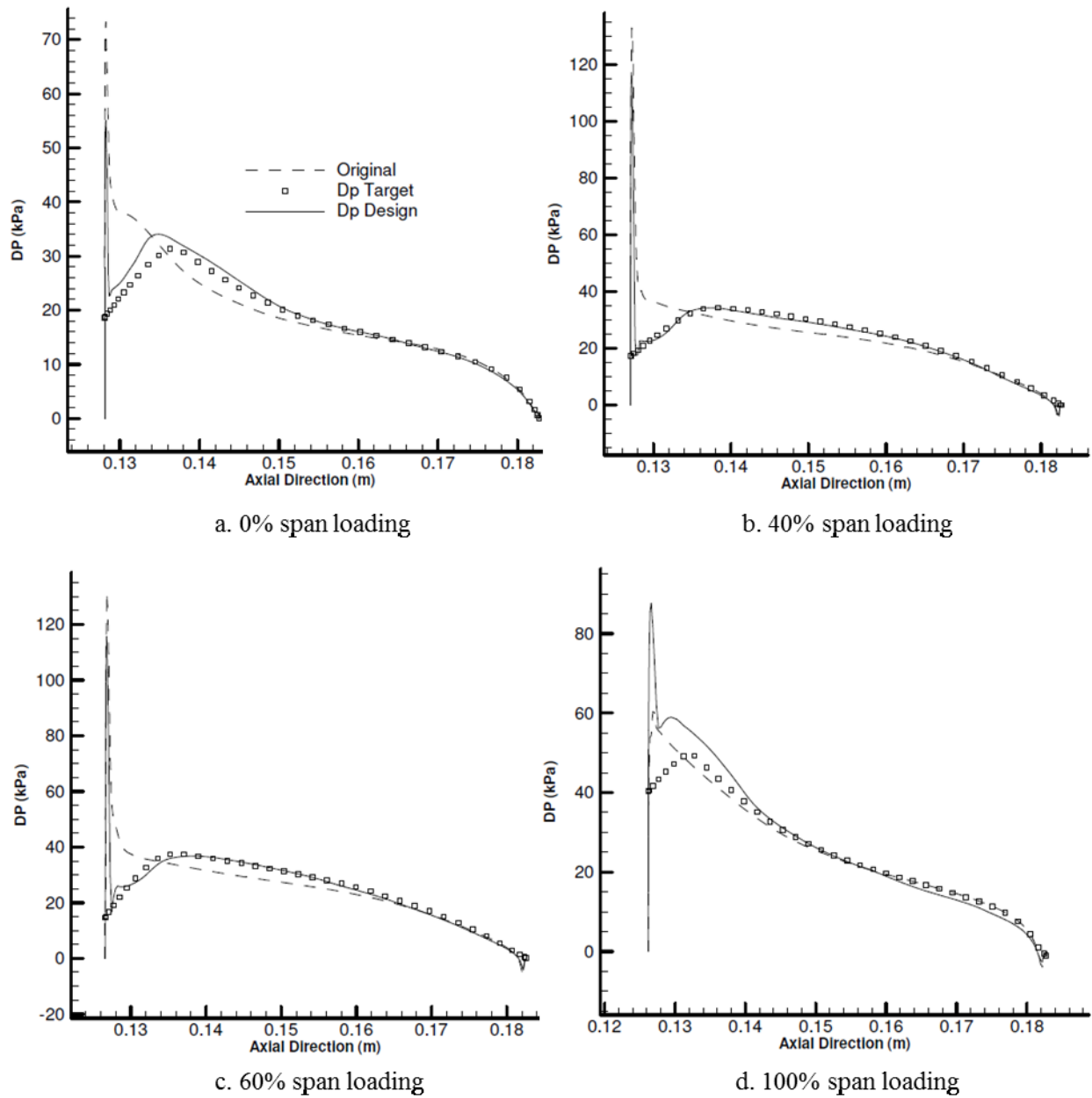


Figure 5.20. Stage 67 stator design: Target and design pressure loading

The total pressure gain in the outer half of the span could be clearly seen in Figure 5.22. Figure 5.23 also illustrates the stage efficiency improvement in the spanwise direction. The original and final designed 3D blades are compared and shown in Figure 5.24.

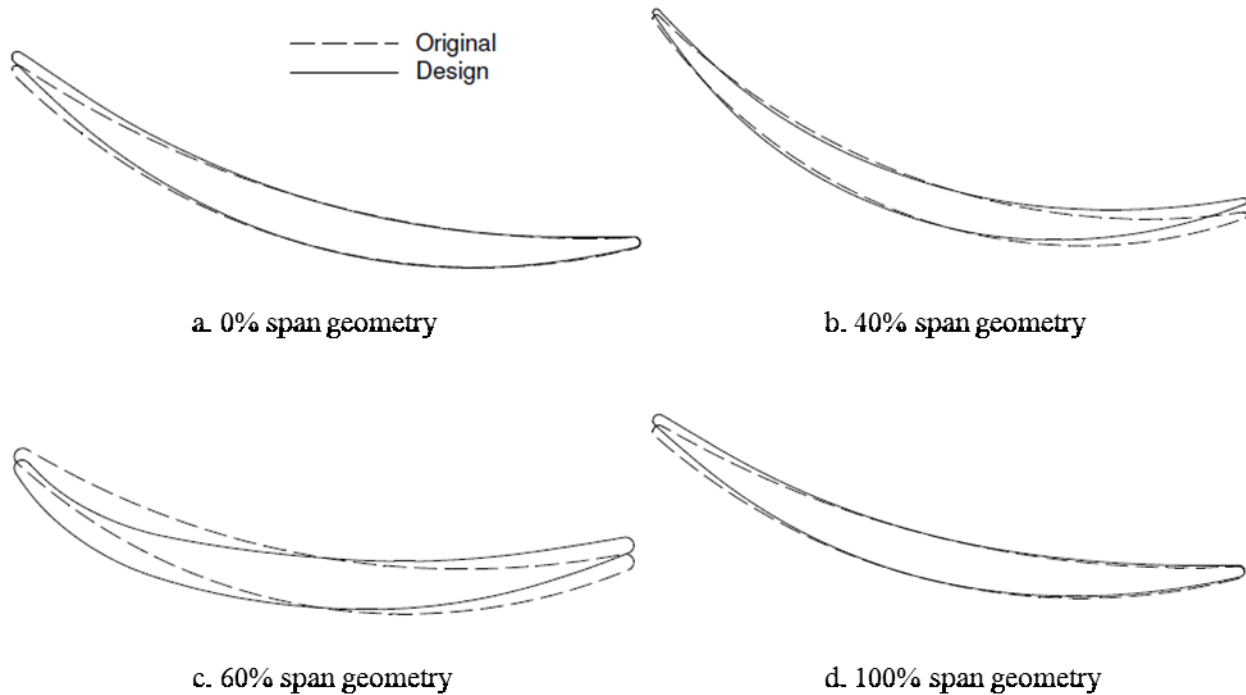


Figure 5.21. Stage 67 stator design: Original and design blade shape

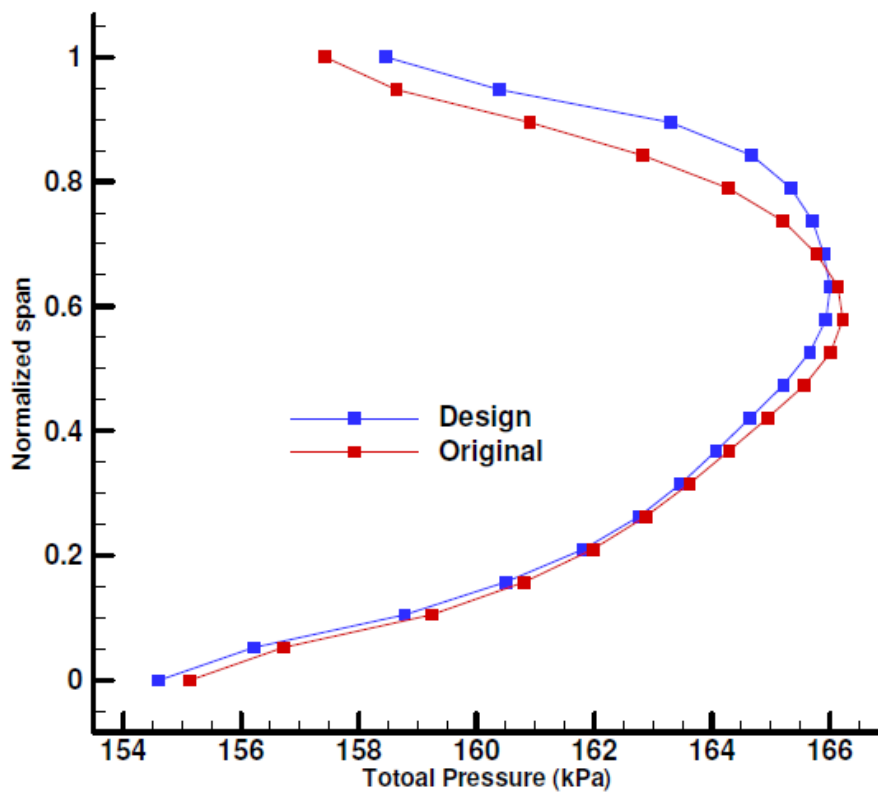


Figure 5.22. Stage 67 stator design: Original and design spanwise total pressure

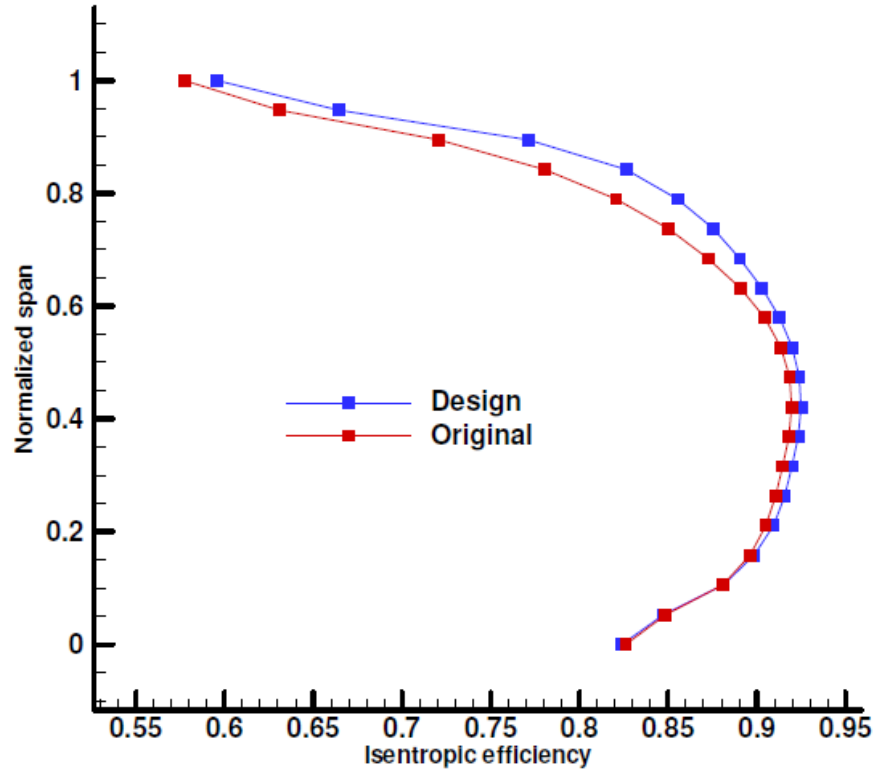


Figure 5.23. Stage 67 stator design: Original and design spanwise efficiency

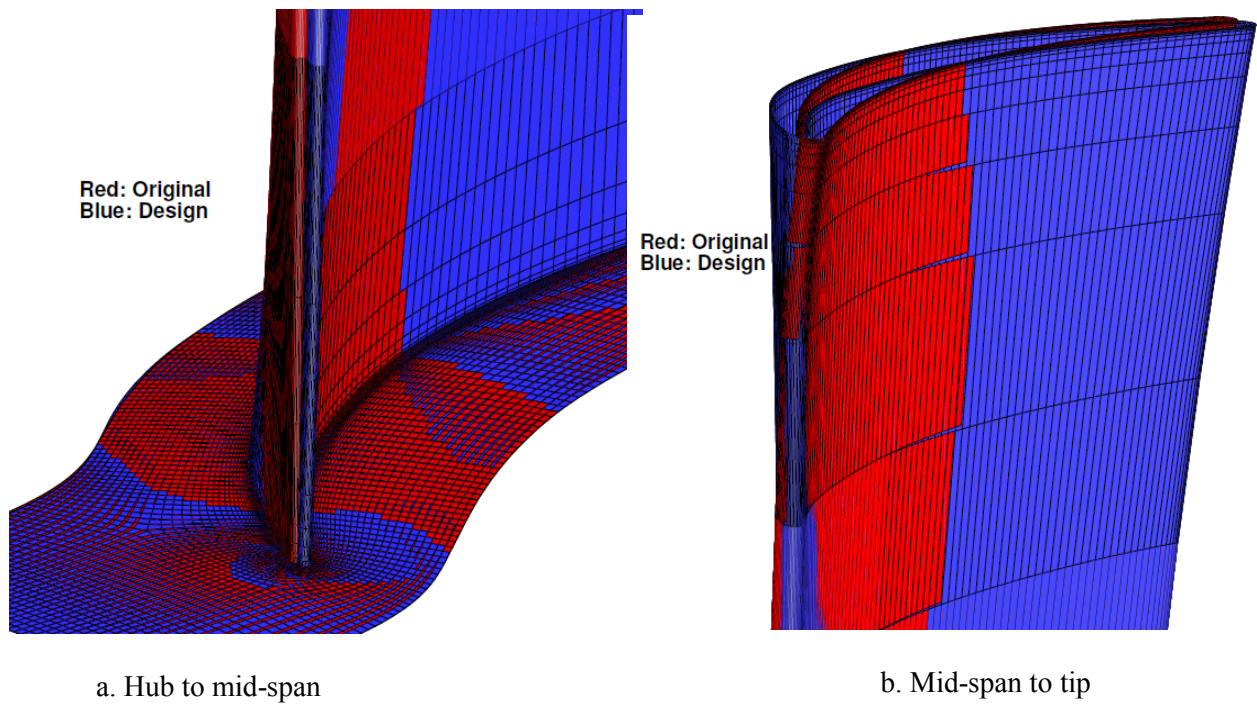


Figure 5.24. Stage 67 stator geometry: Original vs. Designed

5.6. Analysis of the E/TU-3 Turbine Stage

The flow through the E/TU-3 turbine stage was simulated using ANSYS-CFX and the resulting flow field was compared with the experimental data [47].

Similar to previous cases, TurboGrid, was used to generate an O-Grid mesh around the blades and fill the rest of the domain with H-grid mesh and BSL turbulence model was used for the analysis.

The rotor and stator domains contained 303K and 316K nodes, respectively.

A 3D view of the stage is shown in Figure 5.25. The geometric characteristics and the flow parameters at design point are given in Tables 5.10 and 5.11.

It can be seen from table 2 that the computed and measured data match reasonably well and the discrepancy between the computed results and the experimental data were found to be below 1.5%.

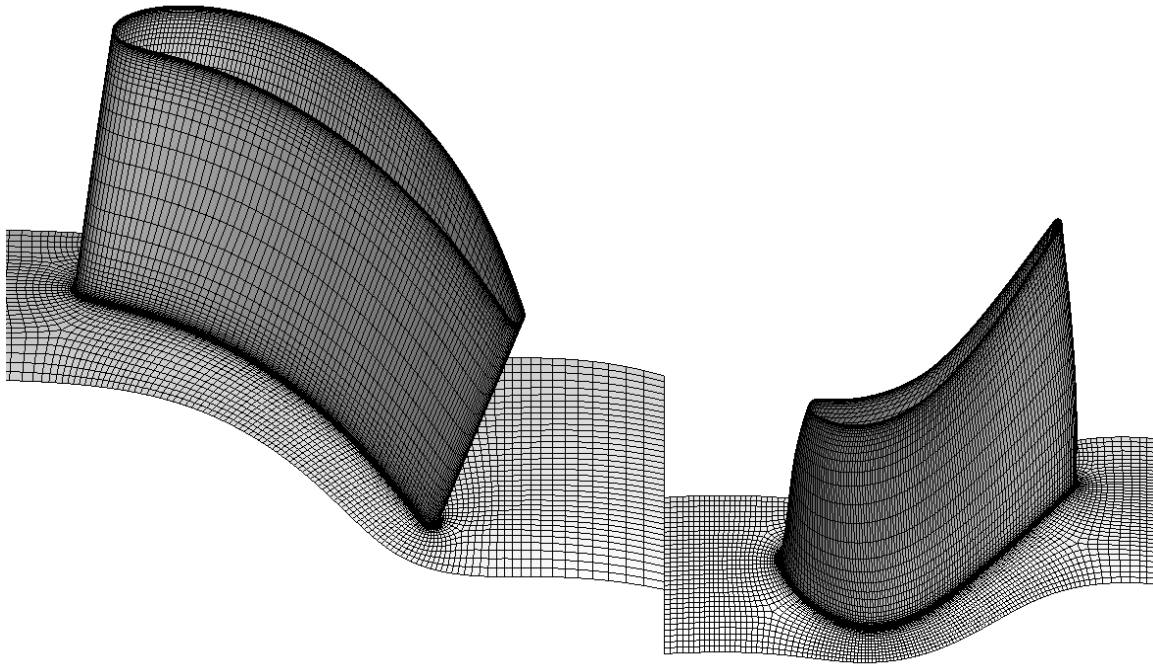


Figure 5.25. 3D view of E/TU-3 Turbine Stage

Table 5.10. E/TU-3 stage geometric characteristics

	Stator	Rotor
<i>Number of blades</i>	20	31
Blade aspect ratio	0.85	1.1
Flow turning (°)	69	105
Mid-span chord (mm)	95.5	60.8
Flow channel		
Tip diameter (mm)	450	
Hub-to-tip-ratio	0.756	

Table 5.11. E/TU-3 turbine stage analysis results at Design Point

	Measured	Computed
<i>Turbulence model</i>	-	BSL
Inlet tot. T(K)	346	346
Stage PR	0.57	0.57
Reduced mas flow (kg.k/s.bar)	97	97.7
Efficiency (%)	89.6	89.8
Exit tot. T(K)	300	299.6
Enthalpy drop (J/(kg.K))	132	134
Rotor inlet Rel. flow angle	44.7	44.4
Stator exit flow angle (°)	68.3	68.5

5.7. Redesign of the E/TU-3 turbine stage at Design Point

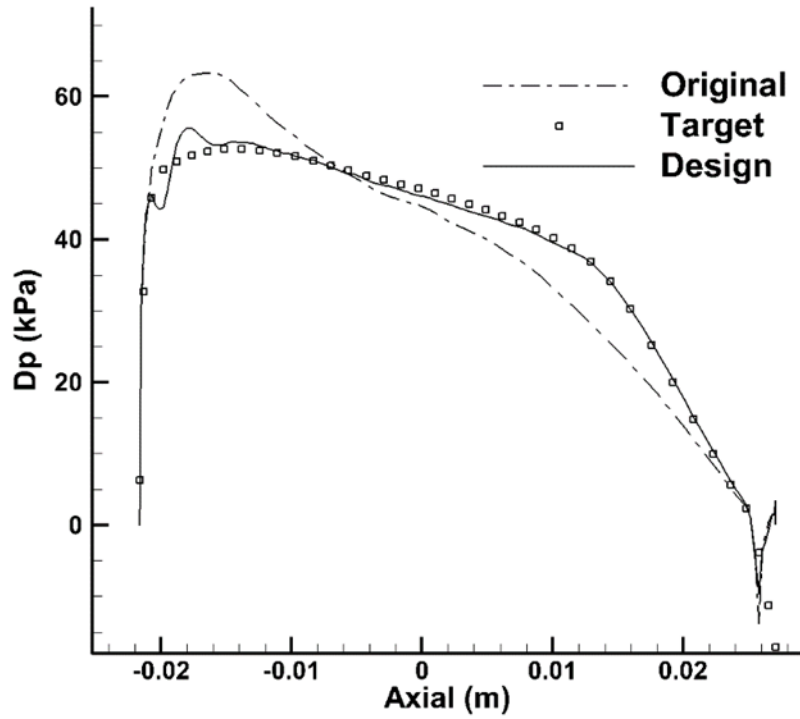
The inverse design method was then used to redesign the E/TU-3 turbine stage. The rotor was redesigned at design point (rotor speed = 7,800 rpm) while the stator blade shape was fixed. In this

case, in addition to the reduction of the peak Mach number on suction surface, the overall loading was slightly increased (by 3%) in order to increase the stage reaction which was expected to have positive impact on the stage efficiency.

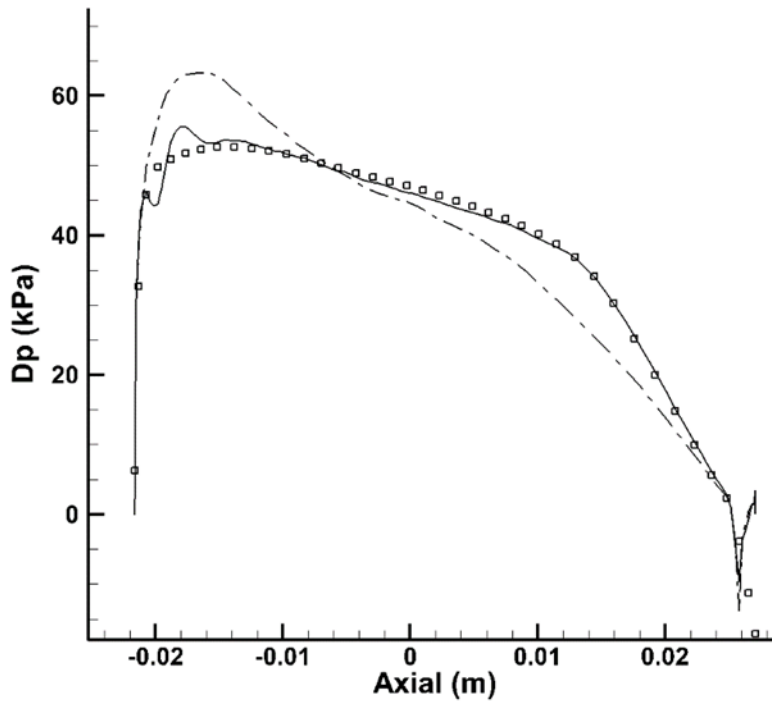
The design variables were the blade pressure loading and normal thickness distributions and the stacking line which was set at the LE. The rotor blade consists of 38 airfoils in the spanwise direction, each with 214 nodes. Six spanwise airfoils located at the rotor hub, 17%, 35%, 55%, 80% and the rotor tip section were chosen as the design airfoils for which target pressure loading was generated. Since there was not a tip clearance for this case, there was no need to extrapolate the last 2% of the blade span. The remaining airfoils were then obtained by Morphing method. The HFR process was applied at each 2-4% of the chord to ensure the smoothness of the blade.

The first and last 5% of the blade were run in analysis mode to ensure that the blade shape is closed and smooth while the non-designed LE/TE portions in compressor blades is 2-3% chord. The reason is the larger thickness of turbine blades where the LE/TE circles cover around 5% of the chord which is aimed to be left outside the design region. The inverse design converged in 150 design steps in total. Again the design process was interrupted a few times and the designed blade was run in analysis mode so as to get rid of flow unsteadiness during the design. The design process was then continued from the latest obtained designed blade. At the end of design process the prescribed target loading was satisfied by 80% on average. Figures 5.26, 5.27 and 5.28 show the original and design loading, airfoil geometry and static pressure at 55% and 80% span.

The reduction of the peak loading and peak Mach number on SS could be clearly seen from Figs. 5.26 and 5.28. The designed blade shape (Figure 5.27) also shows that the maximum camber at about 10-20% chord is reduced and shifted downstream the blade which resulted in loading gain at mid-chord.

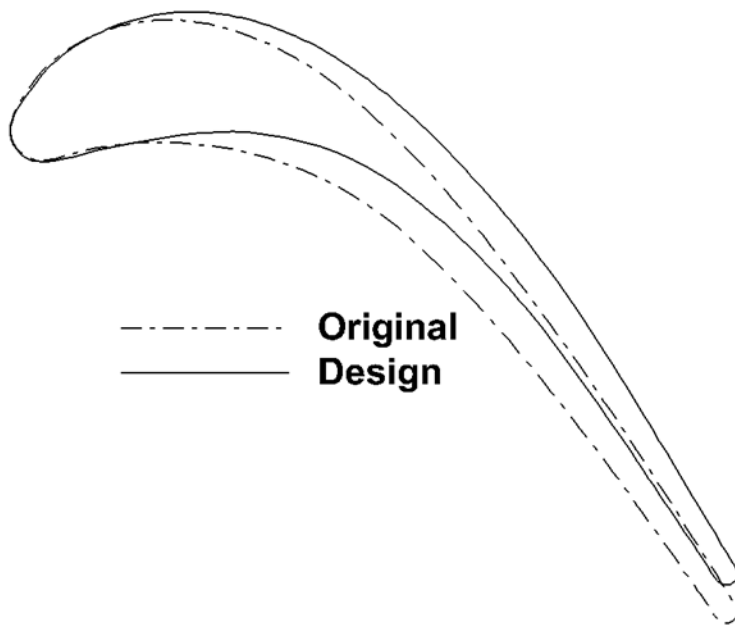


a.55% span loading

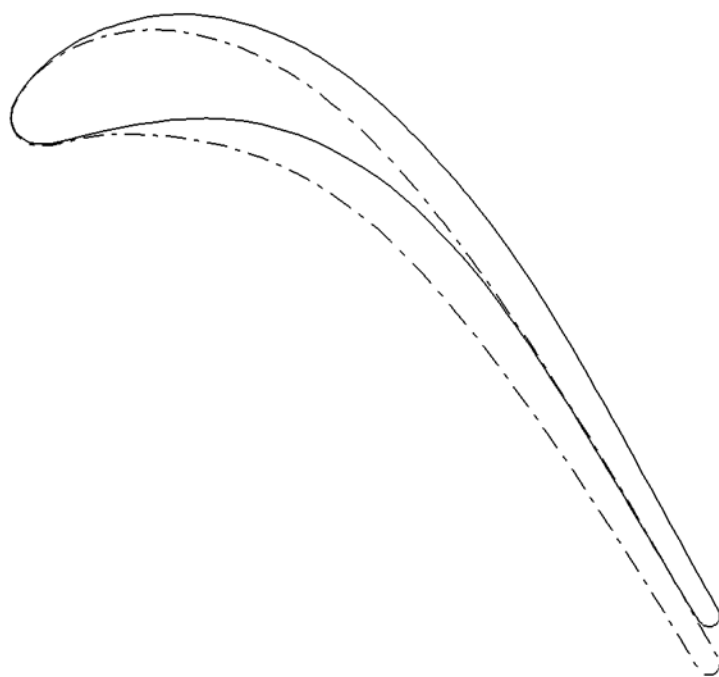


b.80% span loading

Figure 5.26. E/TU-3 Rotor redesign: Original, target and design loading at 55% and 80% span

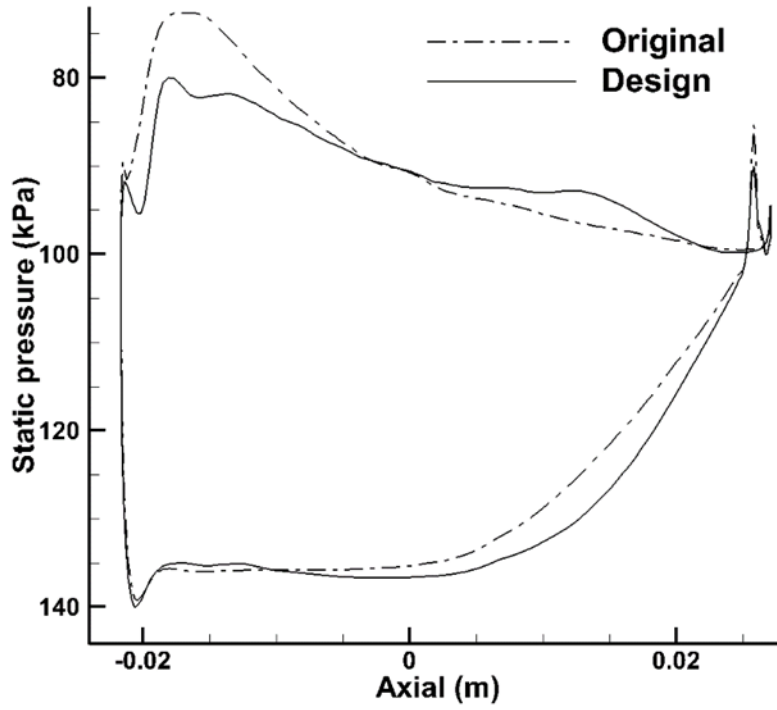


a.55% span geometry

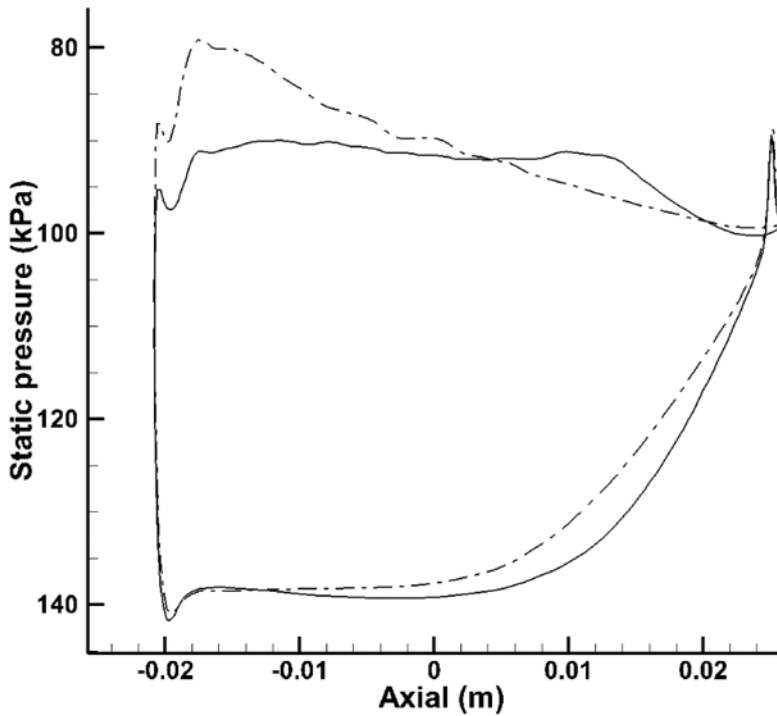


b.80% span geometry

Figure 5.27. E/TU-3 Rotor redesign: Original and design geometry at 55% and 80% span



a.55% span pressure



b.80% span pressure

Figure 5.28. E/TU-3 Rotor redesign: Original and design static pressure at 55% and 80% span

The slight loading gain by the rotor has also caused the increase in stage reaction by 2% and all the mentioned modifications led to the increase in stage total-to-total efficiency from 89.8% to 90.2% (i.e., 0.4%). The design results are listed in Table 5.12.

Table 5.12. E/TU-3 turbine stage: Original and design flow parameters

	Original	Design
Efficiency	89.8	90.2
Enthalpy drop (J/(kg.K))	134	135
Stage PR	0.57	0.57
Reduced mas flow (kg.k/s.bar)	97.7	97.6
Exit tot. T(K)	299.6	299.4
Rotor exit Rel. flow angle (°)	-53.03	-53.67
Mach at rotor exit	0.656	0.663
Stage reaction (%)	31	33

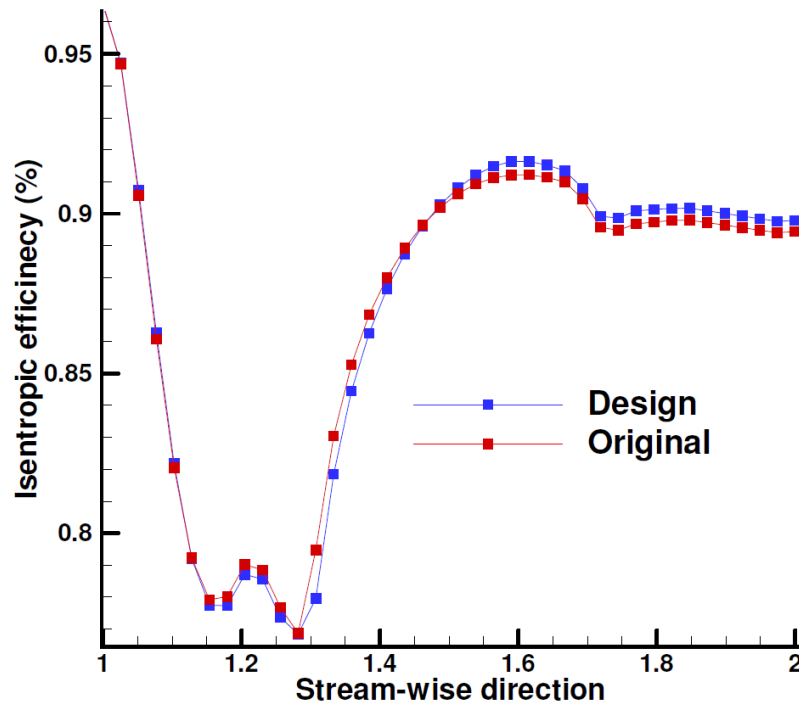


Figure 5.29. E/TU-3 Rotor: Original and designed efficiency in streamwise direction

The streamwise efficiency and adverse pressure gradient of the original and designed rotor blade at design point are shown in Figures 5.29 and 5.30. Although the performance is slightly suffered at the first 30% chord due to the loading loss at that area (Figures 5.26 and 5.28), the reduction of adverse pressure gradient and suction surface Mach number at mid-chord as well as the loading gain at downstream region improved the overall performance.

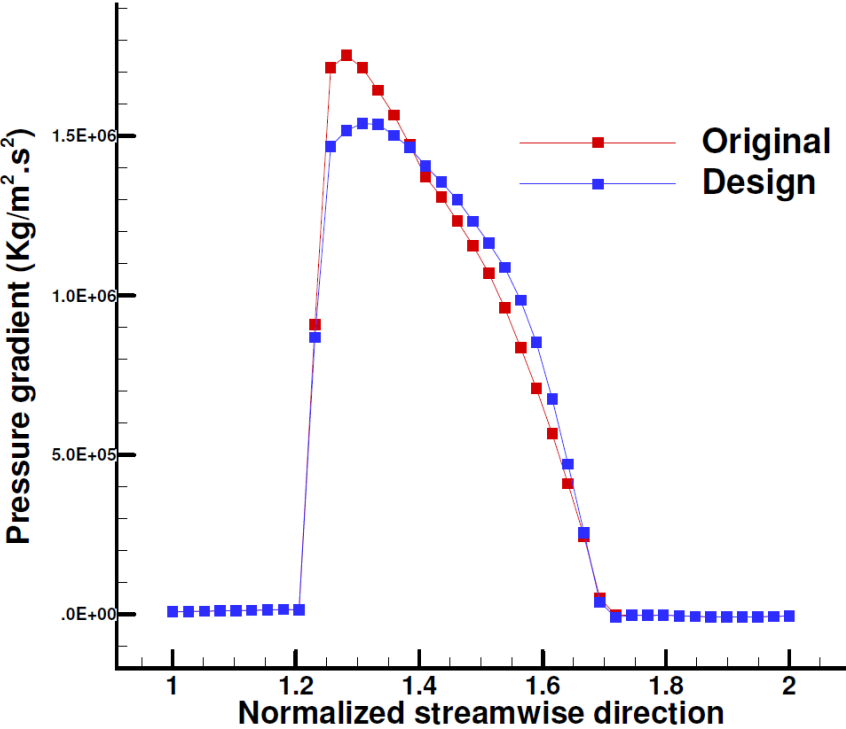


Figure 5.30. E/TU-3 Rotor: Original and designed pressure gradient in streamwise direction

Chapter 6

Conclusion

6.1. Summary

In this research, the aerodynamic inverse design theory that was originally developed by Daneshkhan and Ghaly [23], [25] for viscous compressible flow and was later on implemented into ANSYS-CFX in the context of axial compressor and turbine airfoils in two-dimensional flow [35], has been developed for the aerodynamic inverse blade design in three-dimensional flow. The set of equations resulting from this theory is fully compatible with the Navier-Stokes equations and has been successfully implemented into CFX in the limit of 2D flow [35] and 3D flow in the present work. This is an added flexibility that was not previously available to the designer.

The method was then successfully implemented into ANSYS-CFX using Junction Box Routines and User CEL Functions [34]. The blade deformation is obtained from a virtual velocity that is computed from the difference between the current (instantaneous) and target (fixed) momentum fluxes. The design variables are either the static pressure distribution on the blades pressure and suction surfaces, or the blades pressure loading and thickness distribution which are the same design variables used in the two-dimensional design method. Upon the extension of the method to three-dimensional flow, a third design variable was introduced: a stacking line from hub to tip which identifies the airfoils positions relative to one another in the spanwise direction. An algorithm was also developed to compute the blade normal thickness and normal camberline to

replace the tangential thickness and camberline computations used in 2D inverse design (section 3.3). These two main steps cover the “Future work” mentioned in this author’s Masters’ thesis [35]. Also this work, gives the designer flexibility of prescribing the target pressure distribution on the spanwise airfoils of his/her interest. For such cases, two surface re-construction methods, namely Fitting and Morphing, are programmed and integrated into the main UDF so as to update the full designed 3D blade shape.

The Reynolds-averaged Navier Stokes (RANS) equations are used in analysis (steady state) mode to calculate the flow field when the mesh is stationary and the unsteady Reynolds-Averaged Navier Stokes (URANS) equations written for a moving and deforming mesh using the Arbitrary Lagrangian–Eulerian (ALE) formulation are used in the design mode [35].

The method was first validated for the transonic Rotor 37, and then the design convergence level was evaluated by implementing the method on a single stator blade row, a compressor and a turbine stage axial machines. The 3D inverse design method was finally used to redesign a transonic compressor stage [33], a subsonic compressor and a subsonic turbine stages with the intention to improve their overall aerodynamic performance. It was shown, in Chapter 5, that the transonic Stage 67 efficiency was improved by 1% (from 84.9% to 85.9%), the E/CO-3 compressor stage efficiency was improved by 0.5% (from 89.6% to 90.05%) at the design point and by 1.9% (from 85.7% to 87.6%) at maximum flow, and the E/TU-3 turbine stage efficiency was improved by 0.4% (from 89.8% to 90.2%).

It was shown that the integration of the inverse method into a CFD code [28], [33] is advantageous in different aspects. This work demonstrates the ability to inverse-design turbomachinery stages using the same CFD code used in analyzing them. Combined with an established CFD program the user can take advantage of all features available in the chosen CFD code e.g., turbulence

models and mesh generation tools (such as ICEM-CFD and TurboGrid) as well as new models that may be developed in the future. It will also make the inverse method readily available to the designers who are using the same CFD solver to analyze the flow in turbines and compressors. The overall design process will be also considerably simplified as the designer will only need to set up the proper boundary conditions and take care of a few design parameters.

6.2. Future work

By extending the 2D inverse design method to the redesign of blades in three-dimensional flow, now the method could be used to deal with the real life problems and its successful implementation into a commercial code provides the designer with a practical tool to improve the design of any existing axial turbine or compressor configuration in the aerospace industry. So at this level, the “Future work” on this method is to be sought in its various possible applications.

The very first next step could be using the inverse method for the redesign of transonic cases where passage shocks are involved. The usefulness of the method in e.g. weakening or removing shocks and improving stage performance similar to what was done in two-dimensional flow as shown in [23] and [25].

Also, the method-solver interaction gives the designer access to all flow parameters and blade coordinates which, combined with the designer’s knowledge and experience, could be widely used to:

- Re-stack the blade in order to manipulate the stress or to have desired mass flow rate distribution in spanwise direction

- Change the blade lean or stagger angle in order to control the 3D blade shape which depending on the input may result in a straight or bowed blade, blade with or without stagger change in spanwise direction, etc.
- Re-stagger the stator blades so as to guide the flow in a desired direction at the inlet of the downstream stage.

Finally, the design cases presented in this work were all performed in serial mode (only a single-core processor is involved). However, the time taken to inverse-design them did not exceed a few hours. The use of parallel mode breaks apart the computational tasks and assigns them to several processors which means the flow field, including the blade wall, will be shared among different processors and the blade nodal values, in one shot, will not be available in a single call from within JB routine and the design fails. Upon resolving this issue, the computational time for the redesign of a medium-size compressor/turbine stage is expected to be just a matter of a few minutes.

References

- [1] S. Pierret, A. Demeulenaere, B. Gouverneur, C. Hirsch and R. van den Braembussche, "Designing turbomachinery blades with the function approximation concept and the navier-stokes equations," *AIAA paper 00-4879*, 2000.
- [2] M. Nemec and D. Zingg, "Towards efficient shape optimization based on navier-stokes equations," *AIAA paper 2001-2532*, 2001.
- [3] T. Mengistu and W. Ghaly, "Single and multipoint shape optimization of gas turbine blade cascades," *AIAA paper 2004-4446*, 2004.
- [4] A. Oyama and M. Liou, "Multiobjective optimization of multi-stage compressor using evolutionary algorithm," *AIAA paper 2002-3535*, 2002.
- [5] J. Nocedal and S. Wright, "Numerical Optimization", Berlin: Springer, 1999.
- [6] A. Jameson, "Aerodynamic Design via Control Theory," ICASE, 1988.
- [7] A. Ashrafizadeh, S. Okhovat, M. Pourbagian and G. Raithby, "A semi coupled solution algorithm in aerodynamic inverse shape design," *Inverse Problems in Science and Engineering*, vol. 19, no. 4, pp. 509-528, 2011.
- [8] W. Thompkins and S. Tong, "Inverse or design calculation for nonpotential flows in turbomachinery cascades," *ASME Journal of Engineering for Power*, 104(4), pp. 281-285, 1982.

- [9] L. Zannetti, "A natural formulation for the solution of two-dimensional or axisymmetric inverse problems," *International Journal for Numerical Methods in Engineering*, vol. 22, no. 2, pp. 451-463, 1986.
- [10] M. Giles and M. Drela, "Two-dimensional transonic aerodynamic design method," *AIAA*, vol. 25, pp. 1199-1205, 1987.
- [11] A. Demeulenaere, O. Leonard and R. Van den Braembussche, "A two-dimensional navier-stokes inverse solver for compressor and turbine blade design," *Proceedings of the Institution of Mechanical Engineers*, vol. 211, no. 4, pp. 299-307, 1997.
- [12] L. de Vito, R. V. den Braembussche and M. Deconinck, "A novel two-dimensional viscous inverse design method for turbomachinery blading," *Journal of Turbomachinery*, vol. 125, pp. 310-316, 2003.
- [13] O. Leonard and R. van den Braembussche, "Design method for subsonic transonic cascades with the prescribed mach number distribution," *Transaction ASME*, vol. 114, no. 3, pp. 553-560, 1992.
- [14] L. Zannetti and M. Pandolfi, "Inverse design techniques for cascades," *NASA CR-3836*, 1984.
- [15] T. Dang, "Inverse method for turbomachinery blade using shock-capturing techniques," *AIAA paper 95-2465*, 1995.
- [16] S. Damle, T. Dang, J. Stringham and E. Razinsky, "Practical use of a 3d viscous inverse method for the design of compressor blade," *Journal of Turbomachinery*, vol. 121, no. 2, pp. 321-325, 1999.

- [17] M. Ahmadi and W. Ghaly, "Aerodynamic design of turbomachinery cascades using a finite volume method on unstructured meshes," *Journal of Inverse Problems in Engineering*, vol. 6, no. 4, pp. 281-298, 1998.
- [18] B. Choo and M. Zangeneh, "Development of an (Adaptive) Unstructured 2-D Inverse Design Method for Turbomachinery Blades," in *Proceedings of ASME mTurbo Expo, GT2002-30620*, 2002.
- [19] J. P'ascoa, A. C. Mendes and L. M. C. Gato, "A Fast Iterative Inverse Method for Turbomachinery Blade," *Mechanics Research Communications*, vol. 36, no. 5, p. 630–637, 2009.
- [20] G. S. Dulikravich, "Aerodynamic shape design and optimization: Status and trends," *Journal of Aircraft*, vol. 29, no. 6, pp. 1020-1026, 1992.
- [21] T. Yang and F. Ntone, "Viscous compressible flow direct and inverse computation with illustration," *NASA-CR-175037*.
- [22] S. Tong and W. Thompkins, "A design calculation procedure for shock-free or strong passage shock turbomachinery cascades, ASME Paper 82-GT-220," 1982.
- [23] K. Daneshkhah and W. Ghaly, "Aerodynamic inverse design for viscous flow in turbomachinery blading," *AIAA Journal of Propulsion and Power*, vol. 23, no. 4, pp. 814-820, 2007.
- [24] X. Qiu, M. Ji and T. Dang, "Three-dimensional viscous inverse method for axial blade design," *Journal of Inverse Problems in Science and Engineering*, vol. 17, no. 8, pp. 1019 - 1036, 2009.

- [25] K. Daneshkhah and W. Ghaly, "An inverse blade design method for subsonic and transonic viscous flow in compressors and turbines," *Journal of Inverse Problems in Science and Engineering*, vol. 14, no. 3, pp. 211-231, 2006.
- [26] B. Roidl and W. Ghaly, "Redesign of a Low Speed Turbine Stage Using a New Viscous Inverse Design Method," *Journal of Turbomachinery*, vol. 133, no. 1, 2011.
- [27] V. Mileschin, I. Orekhov, S. Shchipin and A. Startsev, "3D Inverse Design of Transonic Fan Rotors Efficient for a Wide Range of RPM," in *Proceedings of ASME Turbo Expo - GT2007-27817*, 2007.
- [28] A. Arbabi and W. Ghaly, "Inverse Design of Turbine and Compressor Stages Using a Commercial CFD Program," in *Proceedings of ASME Turbo Expo - GT2013-96017*, San Antonio, 2013.
- [29] F. Poursadegh, A. Hajilouy-Benisi and M. Nili-Ahmadabadi, "A Novel Quasi-3D Design Method for Centrifugal Compressor Impeller on the Blade-to-Blade Plane," in *Proceedings of ASME Turbo Expo, GT2011-45451*, Vancouver, 2011.
- [30] J. H. Page, P. Hield and P. G. Tucker, "Inverse Design of 3D Multi-Stage Transonic Fans at Dual Operating Points," in *Proceedings of ASME Turbo Expo, GT2013-95062*, 2013.
- [31] P. Hield, "Semi-Inverse Design Applied to an Eight Stage Transonic Axial Flow Compressor," in *Proceedings of ASME Turbo Expo, GT2008-50430*, 2008.
- [32] T. Korakianitis, I. Hamakhan, M. Rezaenia and A. Wheeler, "Two- and Three-Dimensional Prescribed Surface Curvature Distribution Blade Design (CIRCLE) Method for the Design of High Efficiency Turbines, Compressors, and Isolated Airfoils," 2011.

- [33] A. Arbabi and W. Ghaly, "Aerodynamic Inverse Blade Design of Axial Compressors in Three-Dimensional Flow Using a Commercial CFD Program," in *Proceedings of ASME Turbo Expo - GT2017-65194*, Charlotte, 2017.
- [34] *ANSYS CFX 16.1*, Canonsburg: ANSYS Inc, 2015.
- [35] A. Arbabi, "Aerodynamic Inverse Shape Design of Compressor and Turbine Stages Using ANSYS-CFX," *Master's Thesis, Concordia University, Department of Mechanical Engineering*, 2012.
- [36] K. Daneshkhah, "Aerodynamic inverse design of turbomachinery blading in two-dimensional viscous flow," *Ph.D. Thesis, Concordia University, Department of Mechanical Engineering*, 2007.
- [37] A. J. Medd, "Enhanced Inverse Design Code and Development of Design Strategies for Transonic Compressor Blading," *Ph.D Thesis, Syracuse University, Department of Mechanical and Aerospace Engineering*, 2002.
- [38] L. Gaun, D. Bestle and A. Huppertz, "Hot-To-Cold CAD Geometry Transformation of Aero Engine Parts Based on B-Spline Morphing," in *Proceedings of the ASME Turbo Expo 2014.*, 2014.
- [39] L. Piegl and W. Tiller, *The Nurbs Book*, Springer, 1997.
- [40] S. Mohammadbeigy, "Optimum representation of the blade shape and the design variables in inverse blade design," Concordia University, Montreal, 2016.
- [41] W. Mangler, "Die berechnung eines traflugelprofiles mit vorgeschriebener druckverteilung," *Jahrbuch der Deutschen Luftfahrtanschung*, 1938.

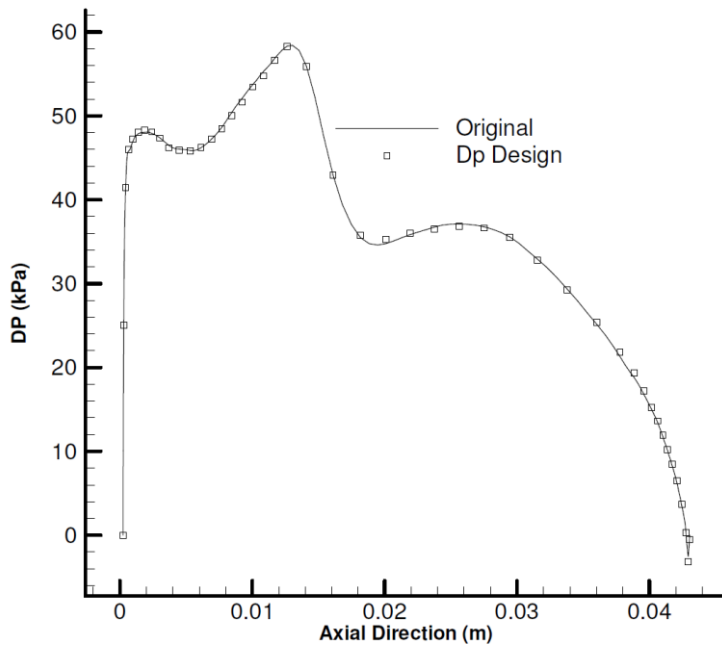
- [42] M. J. Lighthill, "A new method of two-dimensional aerodynamic design," *Aeronautical Research Council*, 1945.
- [43] G. Volpe and R. E. Melnik, "The design of transonic aerofoils by a well-posed inverse method," *International Journal for Numerical Methods in Engineering*, 22, pp. 341-361.
- [44] I. Demirdzic and M. Peric, "Space conservation law in finite volume calculations of fluid flow," *International Journal for Numerical Methods in Fluids*, vol. 8, pp. 1037-1050, 1988.
- [45] L. Reid and D. Royce, "Design and overall performance of four highly loaded, high-speed inlet stages for an advanced high-pressure-ratio core compressor," *NASA Technical Paper 1337*, 1978.
- [46] S. Walter and W. Stevens, "Design and performance of a 427-meter-per-second-tip-speed two-stage fan having a 2.40 pressure ratio," *NASA Technical Paper 1314*, 1978.
- [47] L. Fottner, "Test cases for computation of internal flows in aero engine components", 1990.

Appendix A

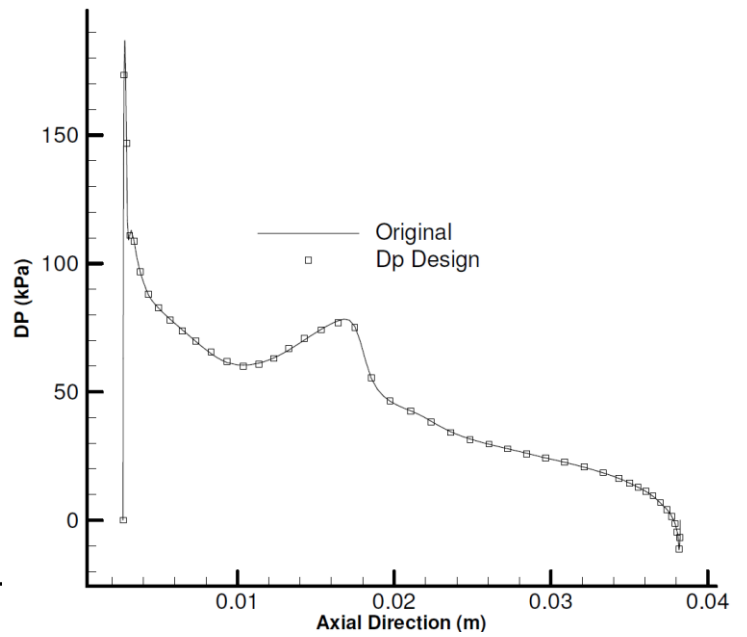
Validation of the inverse design implementation in ANSYS-CFX (Fitting Approach)

NASA Rotor 37 was used to verify the consistency of the inverse methodology and validate its implementation by Fitting [39] approach. The geometry, boundary conditions and all the design variables are the same as the validation case presented in section 4.1. The only difference is the approach used in re-constructing the 3D designed blade.

The validation was performed by inversely designing Rotor 37 for 100 design steps. Similar to the validation case where Morphing method was used, the L_2 -norm of DP remained in the order of $(10^{-3} - 10^{-2})$ while the L_2 -norm of the blade displacement remained in the order of 10^{-5} . Figure A.1 shows the original and the designed loading distribution for the airfoils located at hub, 60%, and 100% blade span, the resulting airfoil shapes are shown in Figure A.2 where the agreement between the original and the design geometry and loading distributions can be seen.



a. 0% span loading



b. 60% span loading

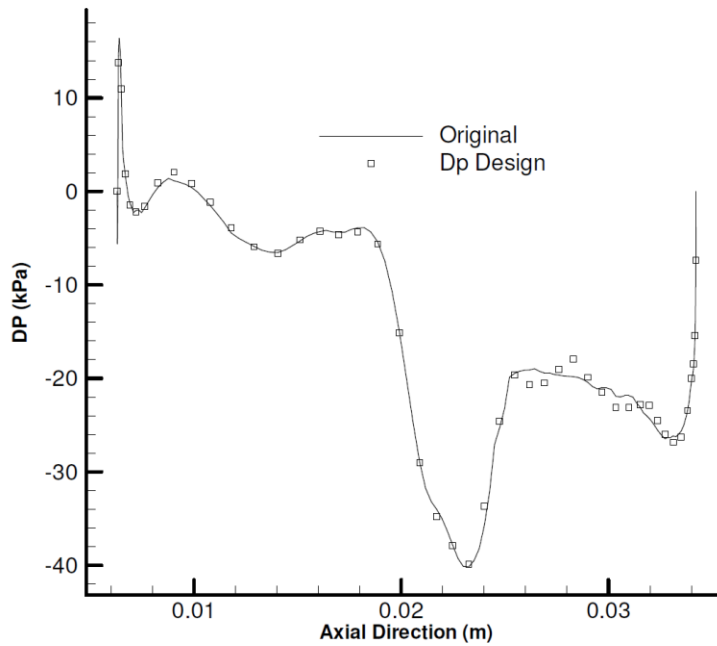
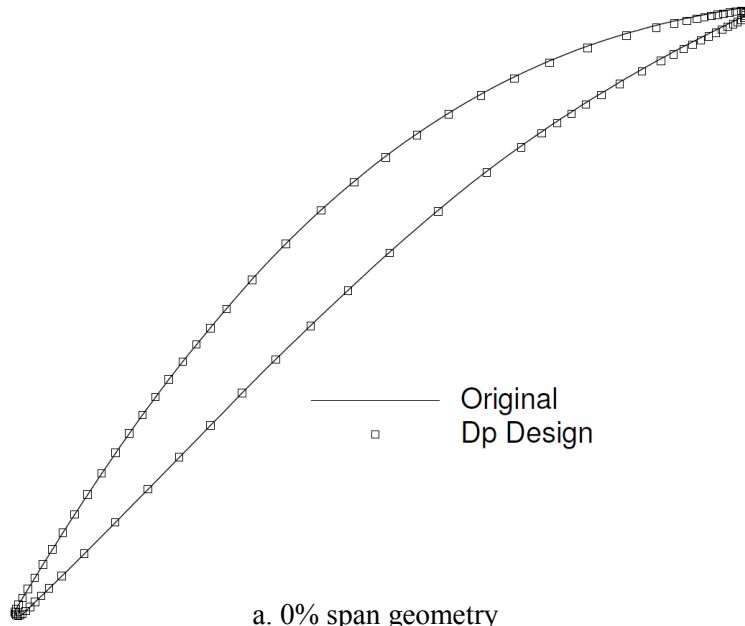
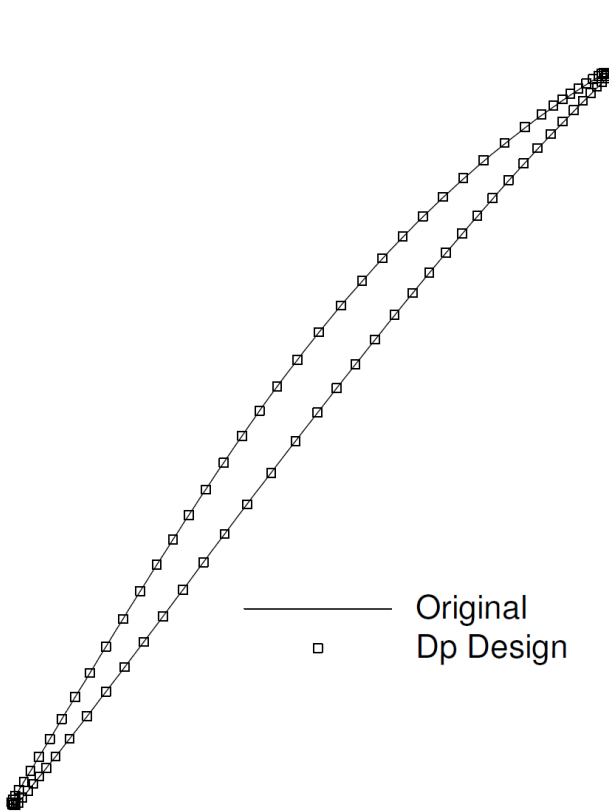


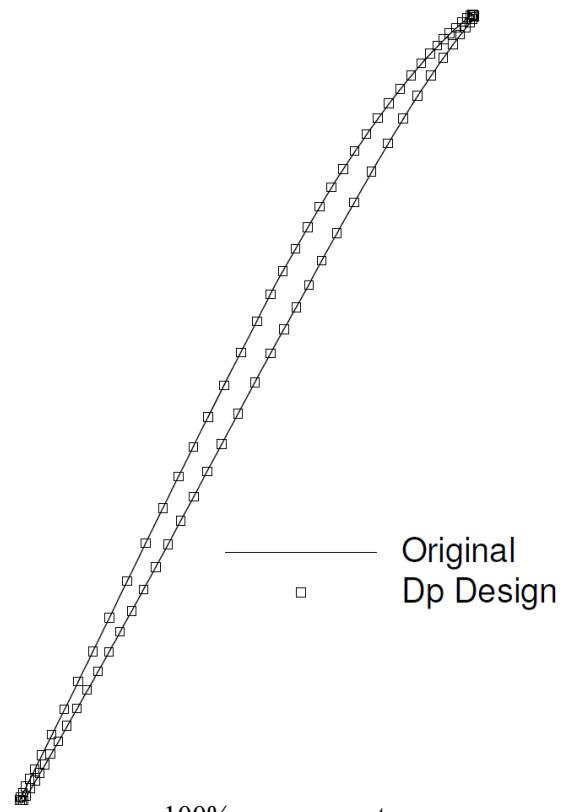
Figure A.1. Rotor 37 validation (Fitting approach): Original and design pressure loading



a. 0% span geometry



b. 60% span geometry



c. 100% span geometry

Figure A.2. Rotor 37 validation (Fitting approach):Original and design geometry

Appendix B

Computational domain

For all the test cases being investigated in this research, this appendix provides the illustration of the computational domain, meridional cut of the stage (or blade row), blade-to-blade cut of the stage at mid-span as well as the tip clearance wherever applicable.

B.1. NASA Rotor 37

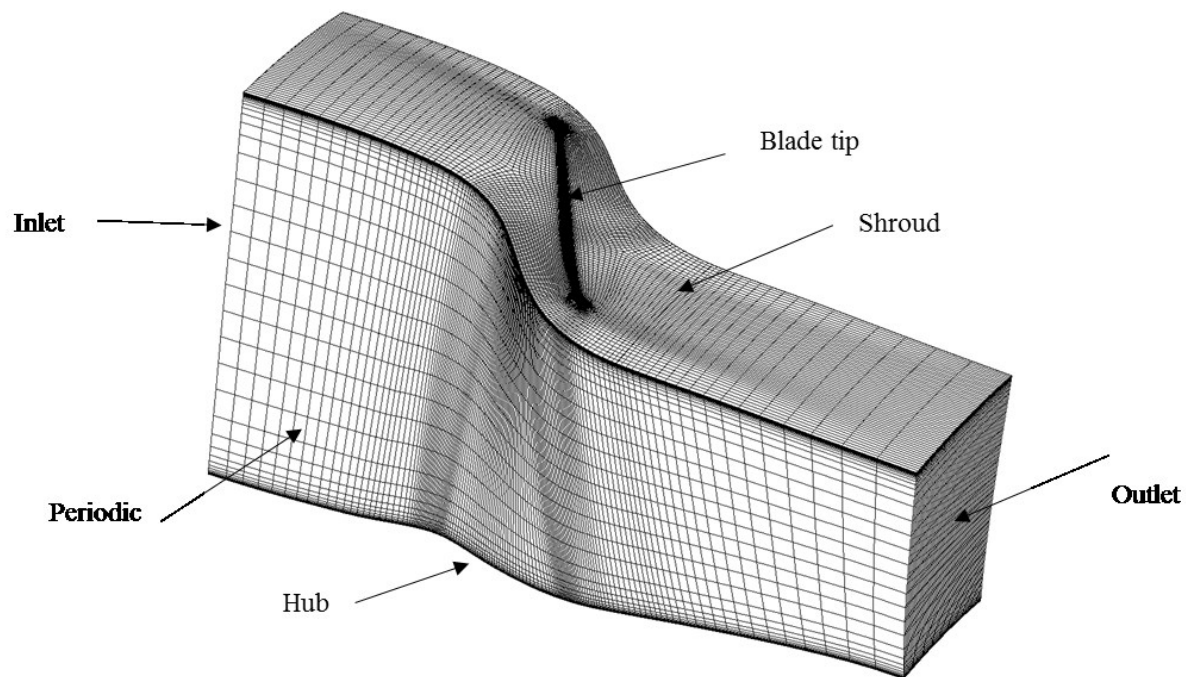


Figure B.1. NASA Rotor 37 – Computational domain

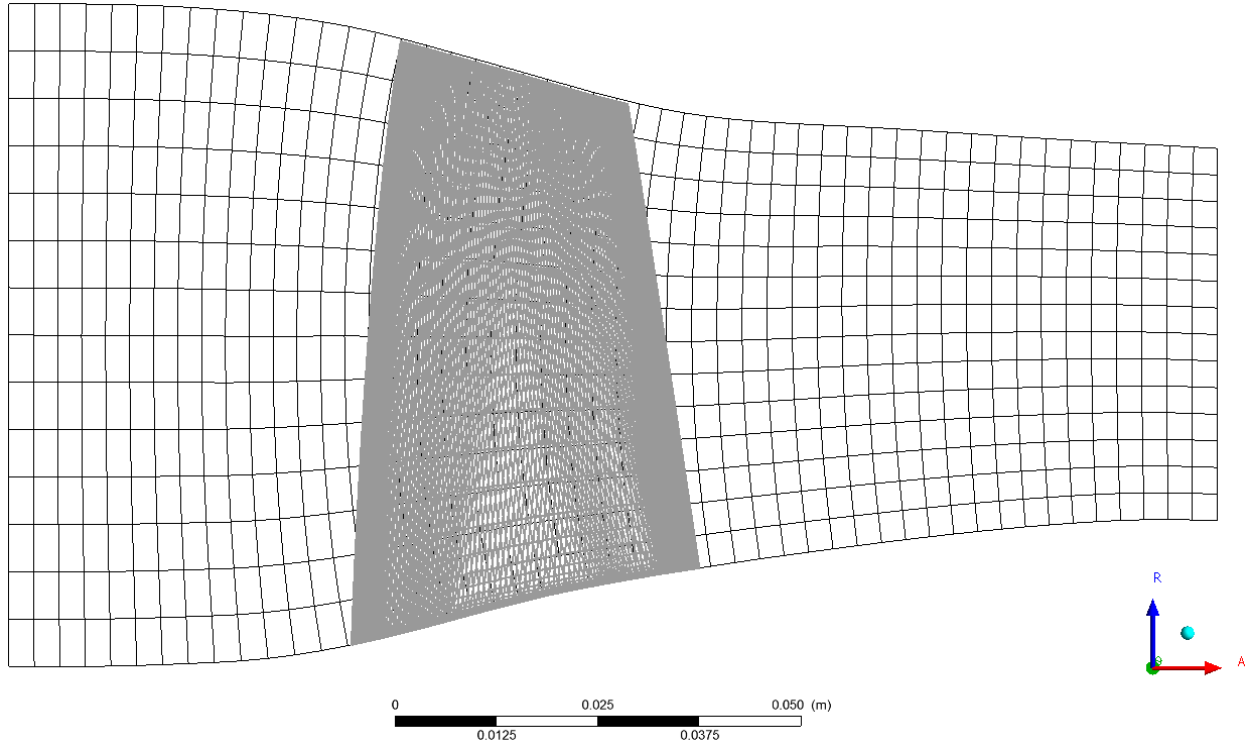


Figure B.2. NASA Rotor 37 – Meridional view

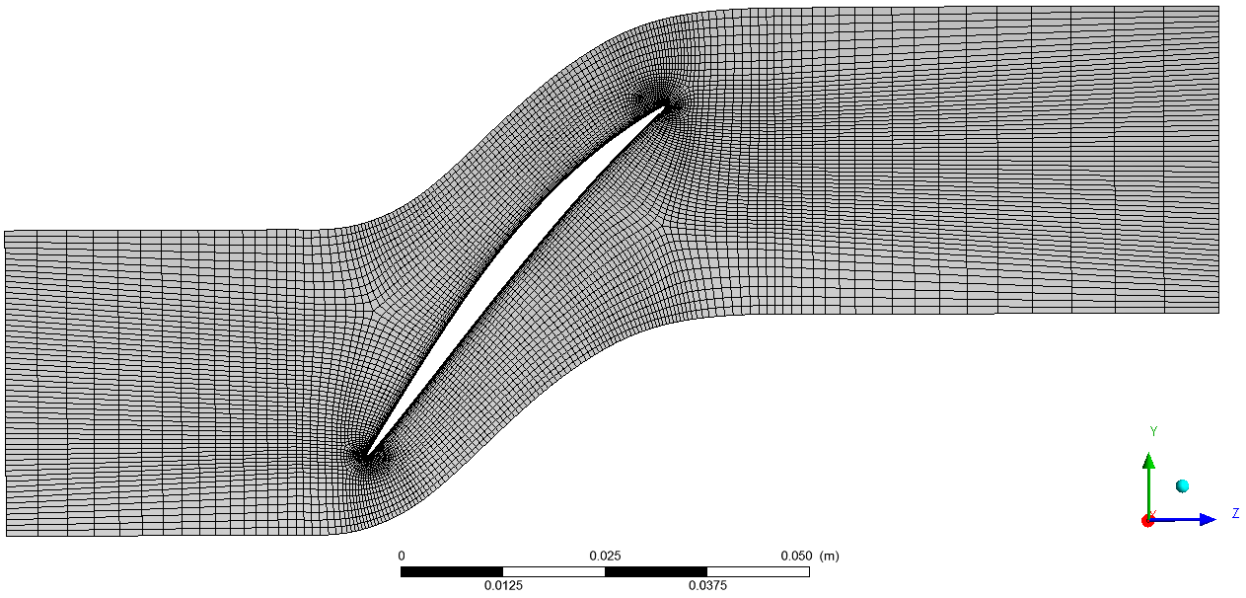


Figure B.3. NASA Rotor 37 – Blade-to-blade view at mid-span

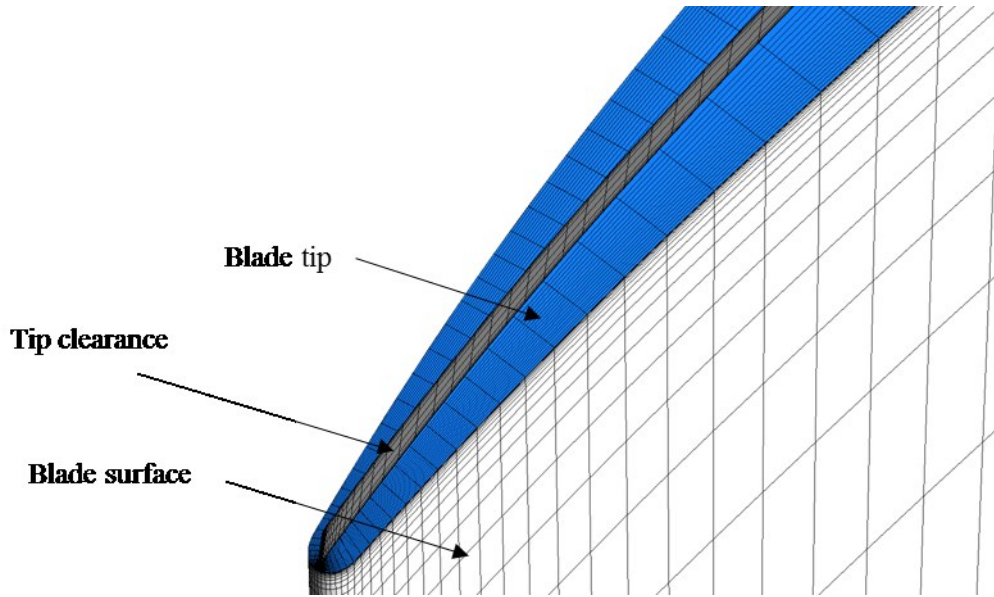


Figure B.4. NASA Rotor 37 – Blade tip and tip clearance

B.2. E/CO-3 Compressor Stage

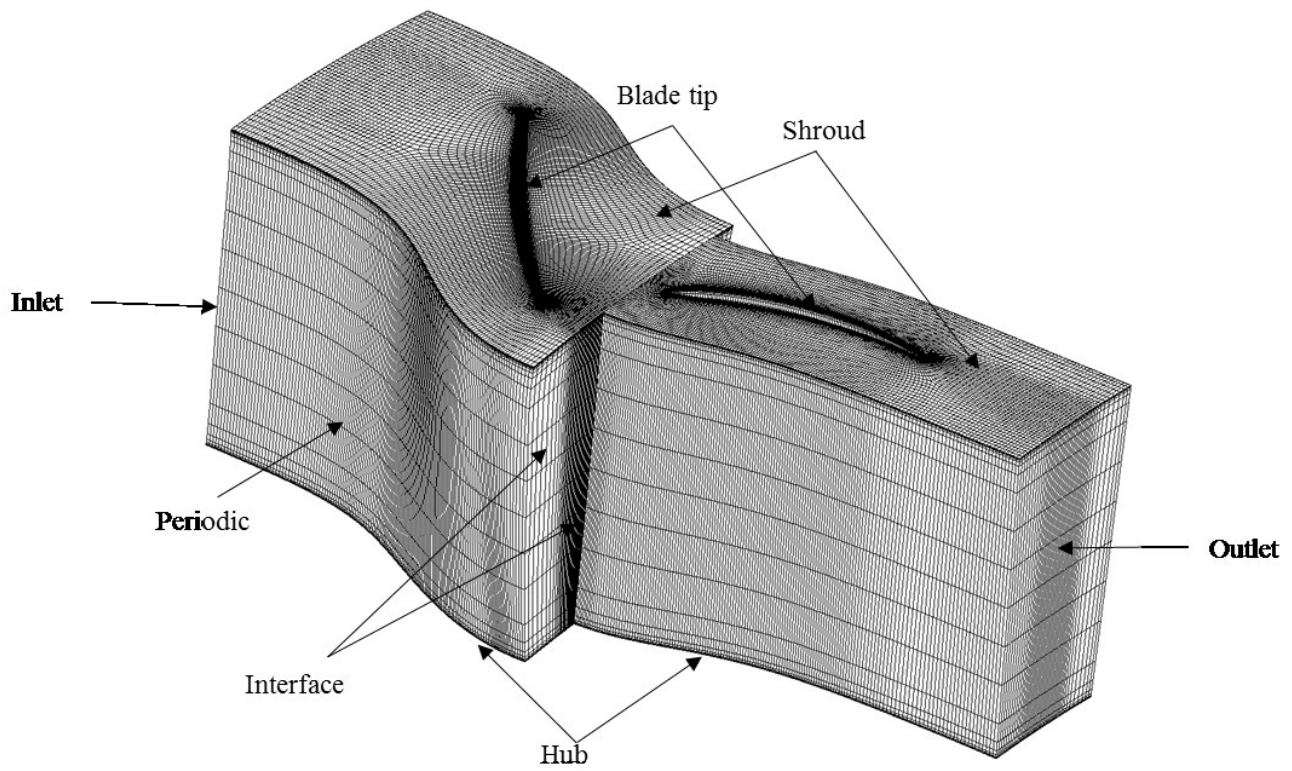


Figure B.5. E/CO-3 Compressor Stage – Computational domain: Rotor (left) & Stator (right)

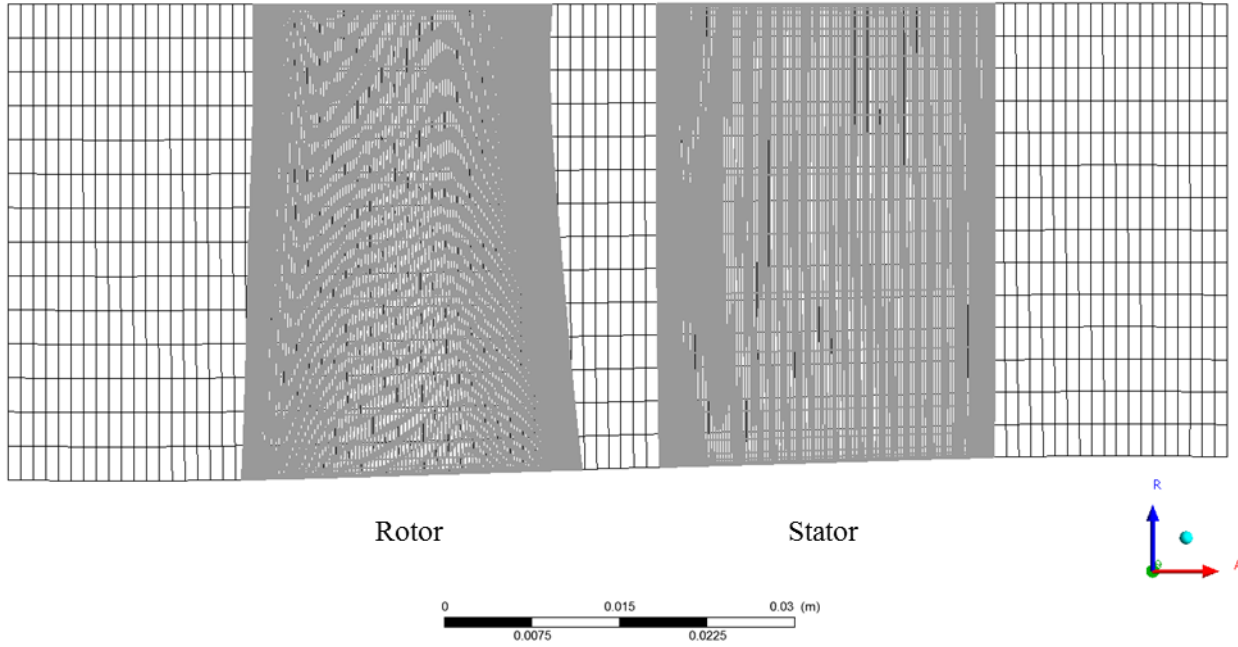


Figure B.6. E/CO-3 Compressor Stage – Meridional view

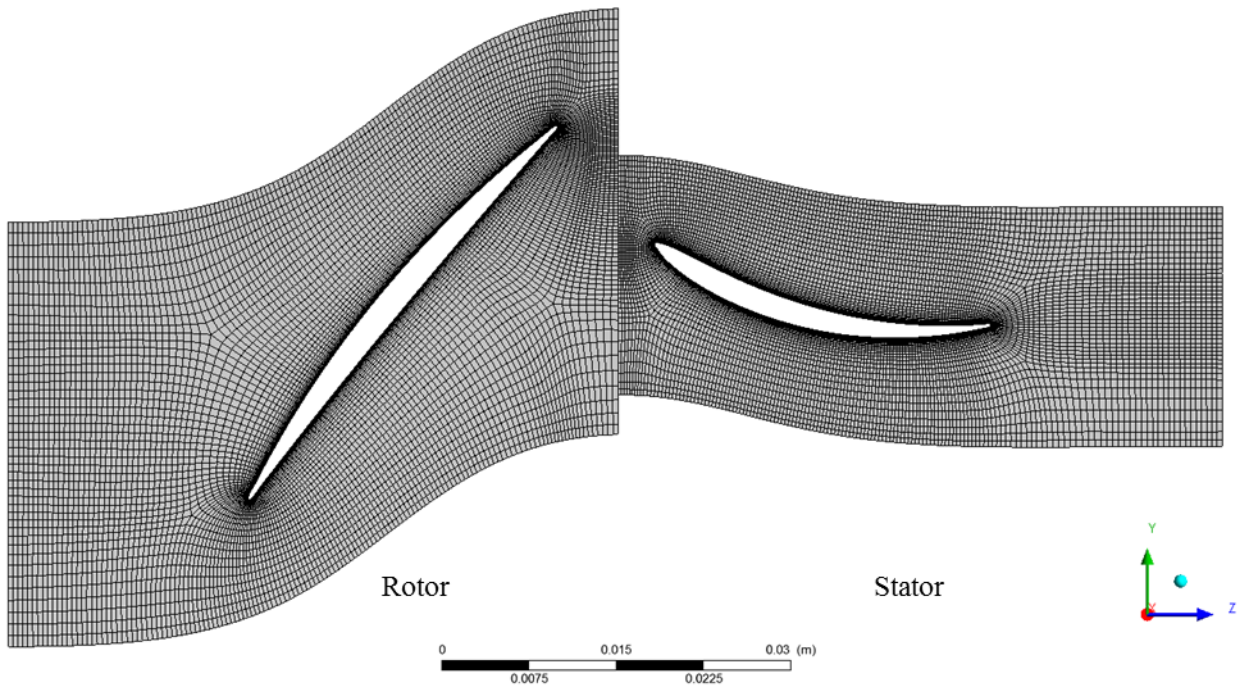


Figure B.7. E/CO-3 Compressor Stage – Blade-to-blade view at mid-span

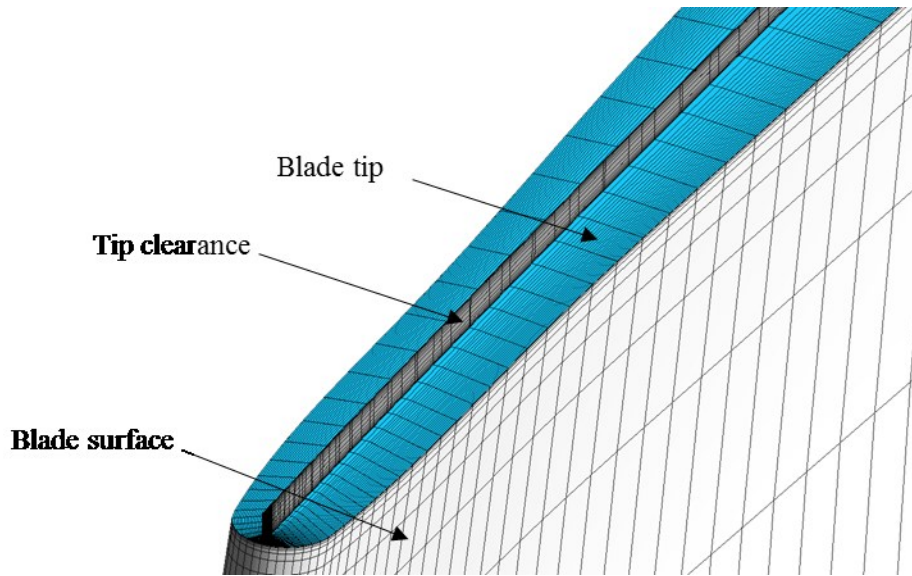


Figure B.8. E/CO-3 Compressor Rotor – Blade tip & tip clearance

B.3. Transonic Compressor 67

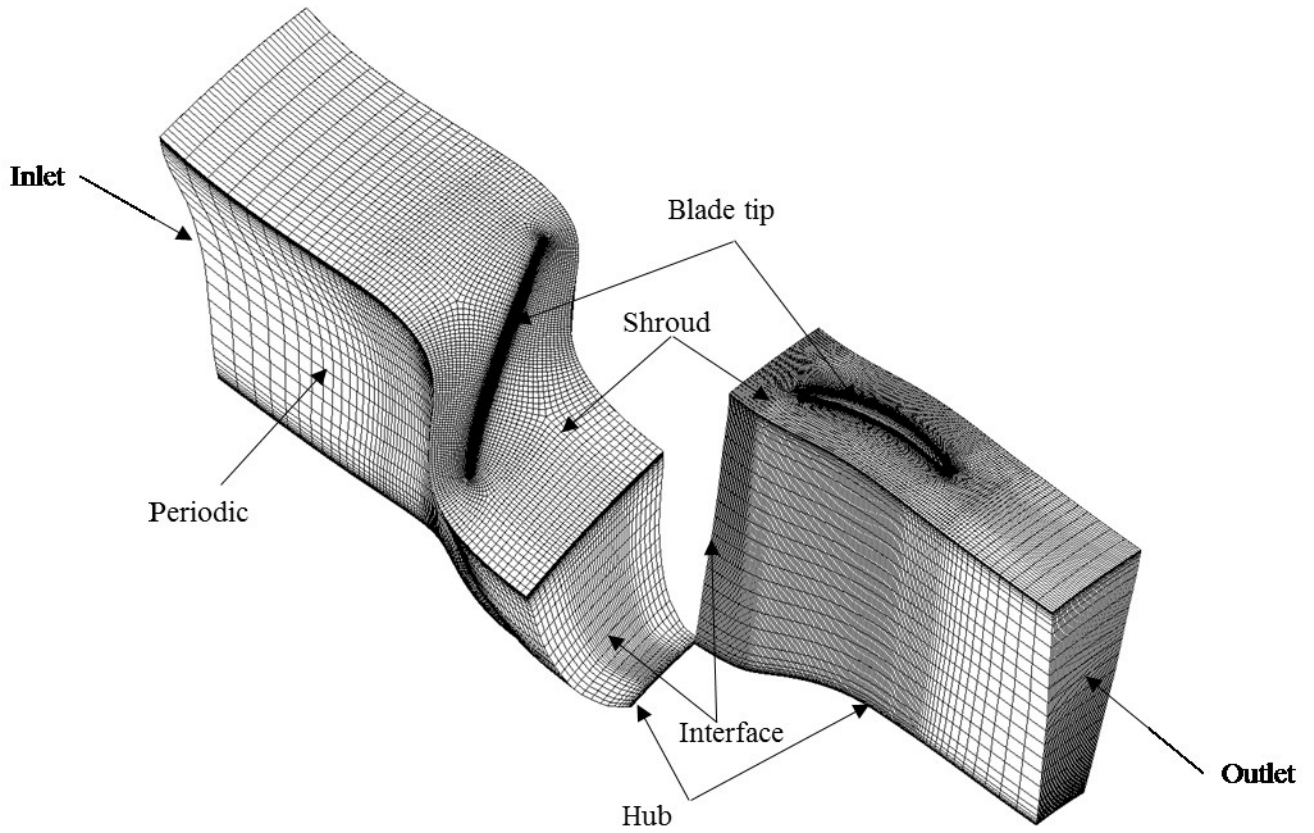


Figure B.9. Stage 67 – Computational domain: rotor (left) & stator (right)

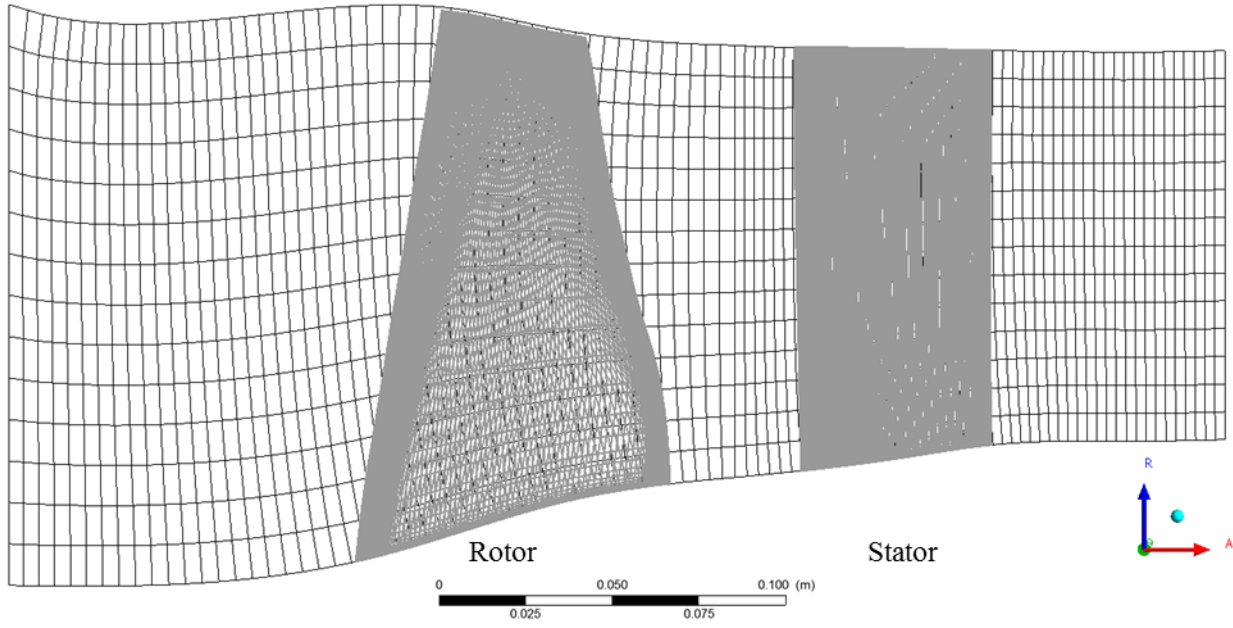


Figure B.10. Stage 67 – Meridional view

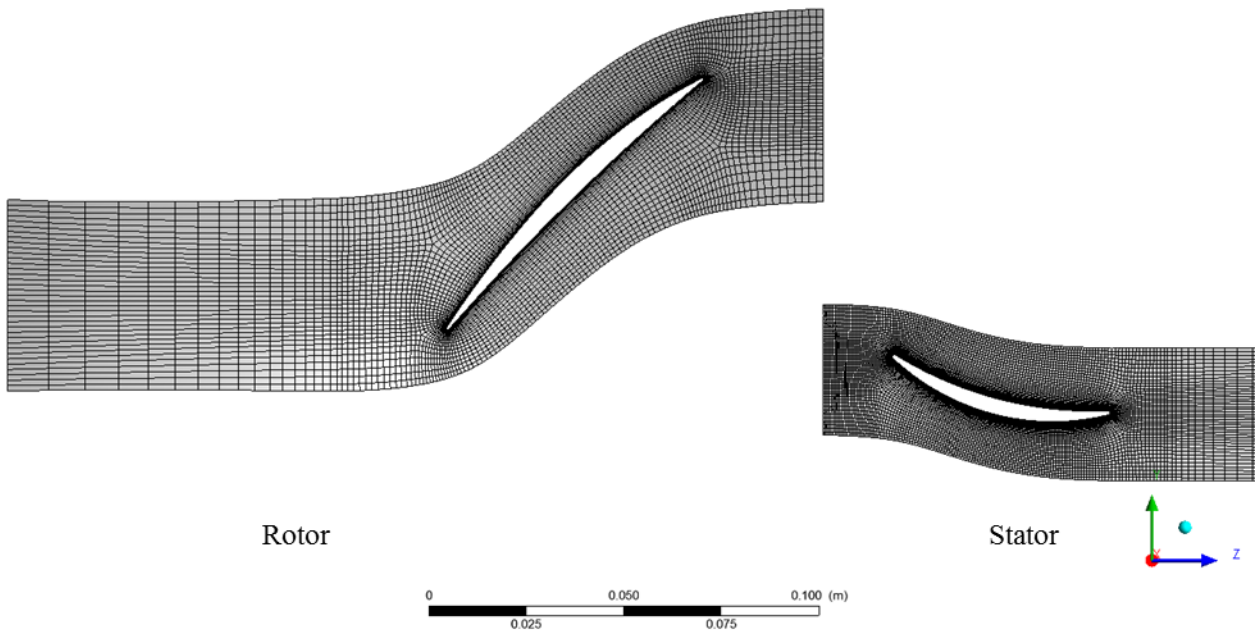


Figure B.11. Stage 67 – Blade-to-blade view at mid-span

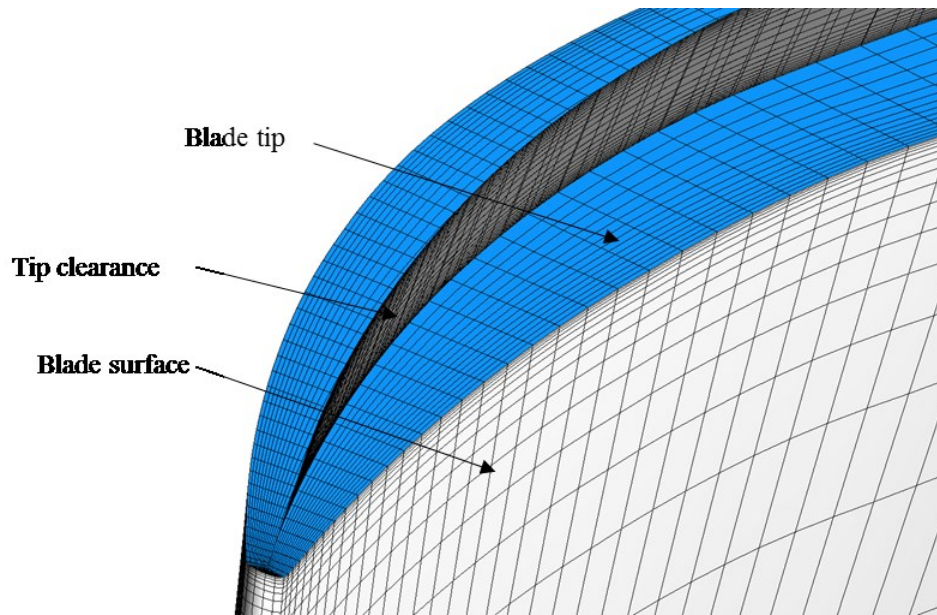


Figure B.12. Rotor 67 – Blade tip & tip clearance

B.4. E/TU-3 Turbine Stage

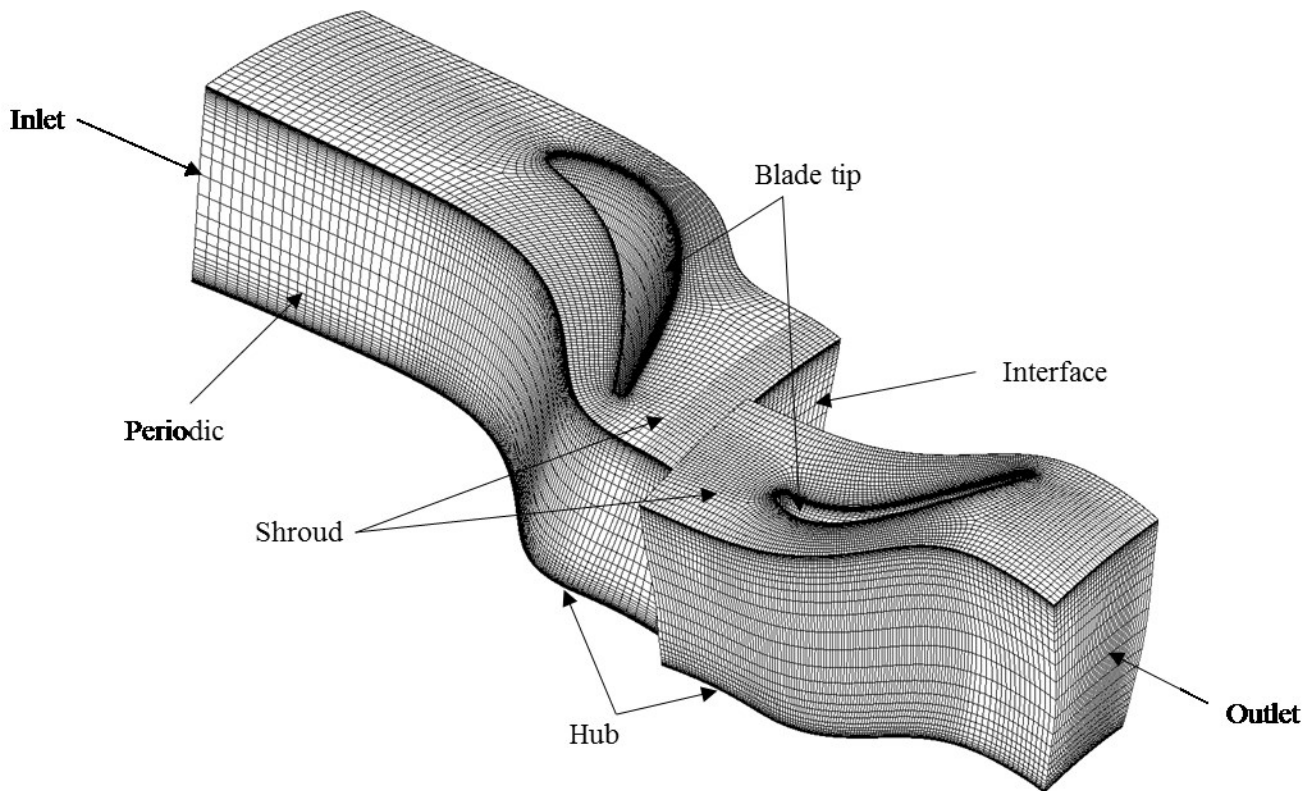


Figure B.13. E/TU-3 Turbine Stage – Computational domain: stator (left) & rotor (right)

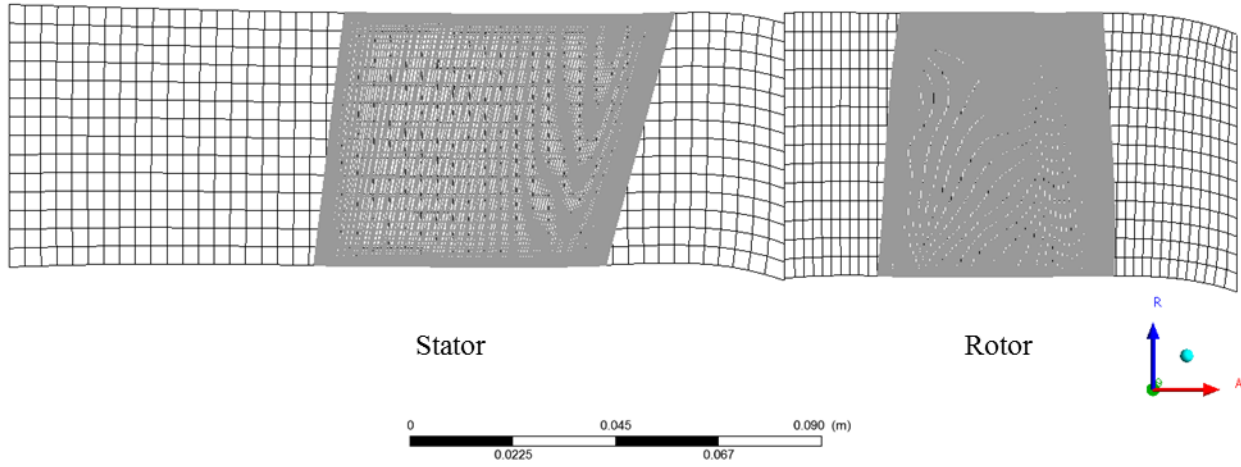


Figure B.14. E/TU-3 Turbine Stage – Meridional view

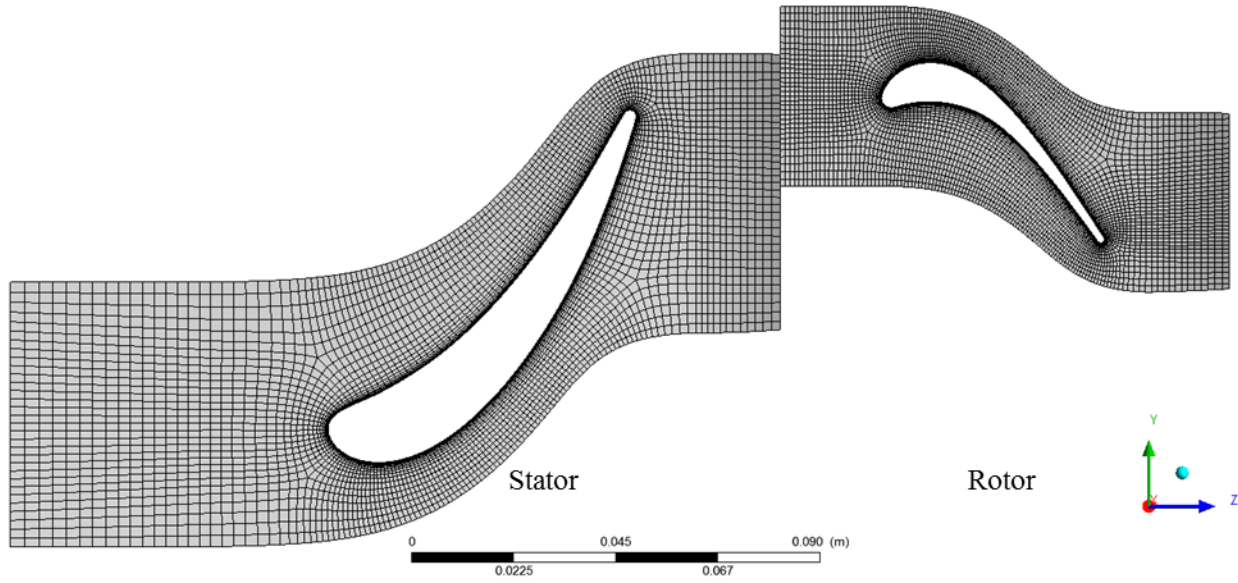


Figure B.15. E/TU/3 Turbine Stage – Blade-to-blade view at mid-span